

MECHANICAL RESPONSE OF 3D PRINTED FUNCTIONALLY GRADED FOAM

Thesis

Submitted in partial fulfillment of the requirements for the degree of

DOCTOR OF PHILOSOPHY

by

BONTHU DILEEP



**DEPARTMENT OF MECHANICAL ENGINEERING
NATIONAL INSTITUTE OF TECHNOLOGY KARNATAKA,
SURATHKAL, MANGALORE – 575025**

FEBRUARY, 2023

DECLARATION

I hereby *declare* that the Research Thesis entitled "**MECHANICAL RESPONSE OF 3D PRINTED FUNCTIONALLY GRADED FOAM**" which is being submitted to the **National Institute of Technology Karnataka, Surathkal** in partial fulfillment of the requirements for the award of the Degree of **Doctor of Philosophy** in **Department of Mechanical Engineering** is a *bonafide report of the research work carried out by me*. The material contained in this Research Thesis has not been submitted to any University or Institution for the award of any degree.

Register Number : **207075ME005**

Name of the Research Scholar : **BONTHU DILEEP**

Signature of the Research Scholar : *B Dileep*

Department of Mechanical Engineering

Place : **NITK, Surathkal**

Date : *21-02-2023*



C E R T I F I C A T E

This is to *certify* that the Research Thesis entitled “**MECHANICAL RESPONSE OF 3D PRINTED FUNCTIONALLY GRADED FOAM**” submitted by **Mr. BONTHU DILEEP** (Register Number: 207075ME005) as the record of the research work carried out by him, is *accepted as the Research Thesis submission* in partial fulfillment of the requirements for the award of degree of **Doctor of Philosophy**.

Research Guide

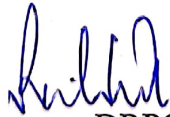


Dr. Mrityunjay Doddamani

Assistant Professor

Department of Mechanical Engineering

NITK, Surathkal.



Chairman – DRPC

Date: 22.2.2023



ACKNOWLEDGEMENT

I want to extend my sincere gratitude to Dr. Mrityunjay Doddamani, Assistant Professor, Mechanical Engineering Department, NITK Surathkal, for the invaluable constructive guidance and encouragement extended throughout my study. I want to thank Research Progress Assessment Committee members Dr. Ramesh M R and Dr. Raviraj H. M. for their valuable input.

I want to thank Prof. Ravikiran Kadoli, Head of the Mechanical Engineering Department, and all the faculty members at the Mechanical Engineering Department for their support throughout this research work.

I want to thank Dr. P Jeyaraj and Prof. Narendranath of the Mechanical Engineering Department, NITK, for their valuable suggestions and for providing the experimental resources necessary for my research.

Constant encouragement of family members, my parents B Sitaramam (mother), B V Satyanarayana (father), to pursue higher studies has made it possible for me to reach at this stage. I wish to thank all my family members for the love, help, and encouragement provided.

I express my sincere thanks to my lab mates Dr. Balu Patil, Dr. Bharath H S, Mr. Sailesh R, Mr. Sumodh Kumar, Dr. Praveen Jayachandran, and the Advanced Manufacturing Lab research team for their help and kind cooperation extended throughout this research work. A special note of thanks to all my friends and well-wishers for their constant help, encouragement, and understanding.

ABSTRACT

In additive manufacturing, fused filament fabrication (FFF) based three-dimensional printing (3DP) is one of the most popular rapid processing technologies. The key benefit of 3DP is the ability to build integrated, complex, and tailored components. Increasing the wide variety of materials that can be processed using this process helps increase the flexibility toward part generation. This made the current work focus on developing a glass micro balloon (GMB) reinforced high density polyethylene (HDPE) based syntactic foam filament. Reinforcing the hollow fillers helps in developing the filament for weight sensitive applications. Nevertheless, processing these fillers with improper process parameters and random volume fractions results in filler failure and agglomeration defects. Hence, taking the quality measuring parameters like filament ductility, roughness, ease of process-ability, and defects like agglomeration, filler percentage is maintained in the range of 20-60 volume %. Syntactic foam filaments of 20, 40, and 60 volume percentage GMB filler are extruded with proper circularity and uniform diameter.

Part quality mainly depends on the selected manufacturing method and its process parameters. Hence, after filament development, this work's primary objective was to optimize 3D printing parameters to develop a defectless part. An outcome of the number of pilot studies helps identify possible defects in 3D printing and overcome strategies. Finally, printing parameters like speed, nozzle temperature, bed temperature, infill percentage, raster angle, layer height, etc., are finalized for processing syntactic foam filaments through an FFF 3D printer. Using these optimized parameters initially plain H, H20, H40, and H60 beams that are 3D printed. Sandwich and functionally graded beams have many advantages compared to plain beams. The current work trail has developed functionally graded foams, and all configurations of foams like SH 20-60, FGF- 1, 2, 3, and FGSF- 1, 2, 3 are successfully 3D printed using the filament replacement method. Extensive scanning electron microscopic analysis was performed to study the interface bonding between the foam layers, filler sustainability, and filler matrix interface. Results showed that the layers of similar and dissimilar compositions are properly fused by forming a

seamless bonding. There is no observable filler failure, but an improper filler matrix interface was observed, which creates porosity in a sample. These voids help in enhancing the weight reduction potential. 3D printed samples are subjected to micro-CT scan to observe the porosity distribution. In this experiment, there was no observable porosity in HDPE layers, whereas some porosity was observed in the foams, and it was quite minimal in H20 and comparatively increased in H60. This porosity estimation is essential. So five samples of each composition are experimentally tested for density measurement, and theoretical density was calculated using a rule of mixtures. The theoretical and experimental density difference is represented as the void percentage. Results showed that the density of the foam increased with an increase in filler percentage and void percentage shows a similar trend for filler. Among graded foams and their respective sandwiches, the void percentage varied in the 4-7% range. The present material is aimed at weight-sensitive applications where the weight saving potential (WSP) plays a crucial role. This WSP increased with an increase in the filler, and it is higher for H60, and in graded foams and their respective sandwiches, it is higher for FGF-2 and FGFSF-2. The percentage of WSP for FGF and FGFSFs varied in the range of 8-14%.

These graded foams are developed for weight sensitive structural and naval applications, so the current work response of these 3D printed foams under various loads and loading conditions was explored. These developed foams are most prone to thrust forces, so the behavior of these foams under compressive loading was studied. It is noted that the compressive modulus increases with the filler content. The graded foams' specific properties exhibited superior response compared to neat HDPE. Among functionally graded foams (FGFs) and functionally graded sandwich foams, FGF-2 (H20-H40-H60) and FGFSF-2 (H-H20-H40-H60-H) showed the highest modulus and yield strength. FGF and FGFSFs exhibited better energy absorption compared to plain foams. FGF and FGFSFs exhibited better energy absorption than foams and are 8 to 19 % more than pure HDPE. All functionally graded foams exhibited a sacrificial failure mechanism. Due to the higher compressive forces, hollow GMB failure was observed in the tested sample.

The response of FGF and FGSFs toward transverse loading was studied by performing three-point bending experiment. The test was conducted at crosshead displacement velocities of 2.54 and 3.41 mm/min for FGF and FGSFs. Experimental results of the flexural test showed that graded sandwiches exhibited better strength than the graded core alone. Among all the functionally graded foams (FGFs), FGF-2 exhibited a better specific modulus, and the modulus of FGF-2 enhanced by 33.83% compared to pure HDPE. FEA results showed unsymmetrical stress distribution along the thickness of the sample. A comparative study of experimental and numerical results showed a slight deviation. The better specific properties of the developed graded foams help to create their preference for weight-sensitive structural applications. The behavior of the FGF and FGSFs subjected to axial compressive load and their natural frequency under zero and non-zero loading conditions was studied through buckling and free vibration analysis. The buckling load of these 3D printed beams was estimated from experimentally acquired load-deflection data using the double tangent method (DTM), modified Budiansky criteria (MBC), and vibration correlation technique (VCT). Results showed that critical buckling load increased with an increase in hollow GMB percentage. Among all FGFs, FGF-2 exhibited the highest buckling load. Compared to pure HDPE buckling strength of FGF-1, FGF-2, and FGF-3 calculated using DTM and MBC methods are increased by 39, 78.4, 47 %, 44.68, 87.23, and 53.19%, respectively. Mechanical stability of the 3D printed graded cores increased post sandwiching them with HDPE skin. All FGSFs outperformed their respective cores in terms of buckling load. FGSFs exhibited a similar trend in the core sample. There is no observable delamination between the 3D printed layers and the skin and core interface, even after increasing the load beyond the sample critical buckling load. Natural frequency is one of the crucial parameters of the beam and is evaluated by performing a free vibration test. Results showed that at mode-1, the natural frequency of all FGF and FGSF beams decreases with increasing load up to critical buckling load, and a further increase in load increases the natural frequency. The natural frequency of the beam increases with an increase in filler percentage. Corresponding to all modes, among all FGF and FGSFs, FGSF-2 exhibited higher natural frequency. The damping factor of the beam increases with an increase in load

up to the critical buckling point; further, an increase in load results in a decrease in the damping factor.

In practical applications of 3D printed beams, they are subjected to non-uniform heating conditions. This necessitates the current work to study the response of these 3D printed plain, graded, and their respective sandwiches towards non-uniform heating. This non-uniform heating was created in an experimental setup by varying the heating position of the IR heater. In case 1 sample was heated at one end. In case-2 sample was heated at the center of the sample, and in case-3, both ends of the sample are subjected to thermal load. Results showed that the thermal stability of the beams enhanced with an increase in GMB percentage. This thermal stability was further enhanced by varying the GMB volume percentage along the thickness direction and sandwiching it with HDPE skin. All 3D printed samples exhibited maximum deflection in case 2 and minimum deflection in case 1. Comparative results concluded that the beams' thermal stability could be enhanced by grading the material property along the thickness direction and sandwiching it.

Keywords: *3D printing, graded sandwich foams, high density polyethylene, glass micro balloon, fused filament fabrication.*

TABLE OF CONTENTS

DECLARATION	
CERTIFICATE	
ACKNOWLEDGEMENT	
ABSTRACT	
TABLE OF CONTENTS.....	I
LIST OF FIGURES.....	VII
LIST OF TABLES.....	XIII
ABBREVIATION.....	XV
NOMENCLATURE.....	XVII
1. INTRODUCTION.....	1
1.1 Composite Materials.....	1
1.2 Classification of composites.....	1
1.3 Syntactic Foams.....	3
1.3.1 Filler.....	4
1.3.2 Matrix.....	6
1.4 Functionally Graded Composite Structure.....	8
1.5 Sandwich.....	10
1.6 Processing of syntactic foam.....	12
1.6.1 Compression Moulding.....	14
1.6.2 Injection Moulding.....	15
1.6.3 Additive Manufacturing.....	16
1.7 Literature Survey.....	22
1.8 Motivation.....	33
1.9 Objectives.....	34
1.10 Outlines of Thesis.....	35

2. MATERIALS AND METHODS	37
2.1 Constituent Materials	37
2.1.1 Matrix	37
2.1.2 Filler.....	37
2.2 Composite Preparation	39
2.3 Melt flow Index (MFI)	41
2.4 Filament Extrusion and 3D Printing	42
2.5 Micro CT	46
2.6 Surface roughness	46
2.7 Density	46
2.8 Flexural Testing.....	47
2.8.1 Experimental Analysis.....	47
2.8.2 Finite Element Analysis.....	47
2.9 Compression Testing.....	48
2.10 Buckling and Free Vibration Behaviour	49
2.10.1 Buckling Load	49
2.10.2 Free Vibration.....	50
2.10.3 Vibration Correlation Technique.....	52
2.10.4 Numerical Analysis	52
2.11 Thermal Buckling.....	53
2.12 Microstructural Characterization.....	55
3. MATERIAL CHARACTERIZATION AND PROCESSING METHODS.....	57
3.1 Blend Characterization.....	57
3.1.1 MFI of HDPE and Composite foams	57
3.2 Filament Development	57
3.3 3D Printing of Syntactic Foam Cored Sandwich composite.....	59

3.3.1 3D Printing	59
3.3.2 Substrate selection	60
3.3.3 Adhesion	62
3.3.4 Improper flow of material.....	64
3.3.5 Prime Pillar	65
3.3.6 Warpage.....	66
3.3.7 Layer offset.....	67
3.3.8 Printing speed	68
3.3.9 Micrographic Investigation.....	69
3.4 Thermo Mechanical Analysis.....	71
3.5 3D printing of functionally graded foams and sandwiches.....	76
3.5.1 SEM analysis of 3D printed FGF and FGFSs'	77
3.6 Micro CT.....	78
3.7 Surface roughness	79
3.8 Density	81
Conclusion.....	84
4. COMPRESSION RESPONSE	87
4.1 compressive behavior of functionally graded core	87
4.1.1 Failure Mechanism	92
4.2 compressive behavior of functionally graded sandwich core	95
Conclusion.....	96
5. FLEXURAL RESPONSE	99
5.1 Flexural response of FGFs	100
5.1.1 Experimental Results.....	100
5.1.2 Finite Element Analysis of Flexural response.....	101
5.2 Flexural response of FGFS.....	103

5.2.1	Experimental Results	103
5.2.2	Finite Element Analysis of Flexural response	105
5.2.3	Failure Mechanism of FGSFs	106
5.3	Comparison of FGF and FGSFs	107
5.4	Micrographic analysis	108
5.5	Property Chart	109
	Conclusion.....	111
6.	VIBRATION BEHAVIOUR.....	113
6.1	Buckling and free vibration of functionally graded core under axial compression	113
6.1.1	Buckling behaviour of FGFs.	113
6.1.2	Free Vibration.....	118
6.1.3	Estimation of critical buckling load using VCT	121
6.1.4	Property Chart.....	121
6.2	Buckling and free vibration of functionally graded sandwich foam	122
6.2.1	Critical buckling load of FGSF	123
6.2.2	Free vibration behavior of FGSF	128
6.2.3	Property chart	130
	Conclusion.....	131
7.	THERMAL BUCKLING	133
7.1	Experimental analysis of thermal buckling	133
7.1.1.	Case1: One end heating	135
7.1.2	Case2: Centre heating	138
7.1.3	Case:3 Both end heating	142
	Conclusion.....	145
8.	SUMMARY AND CONCLUSIVE REMARKS	147

SCOPE OF FUTURE WORK	151
REFERENCES	153
LIST OF PUBLICATIONS	173
BIO-DATA	175

LIST OF FIGURES

Figure 1.1. Composite classification with respect to filler.	2
Figure 1.2. Multiple phases of syntactic foams.	4
Figure 1.3. Classification of filler.	5
Figure 1.4. SEM of hollow GMB.	6
Figure 1.5. Polymer consumption in India (ShekharB. 2012).	8
Figure 1.6. Various types of gradation.....	9
Figure 1.7. Types of sandwich.....	11
Figure 1.8. Preparation of syntactic foam.....	13
Figure 1.9. Classification of plastics.....	14
Figure 1.10. Flow chart of AM process.....	17
Figure 1.11. Representative image of FFF process.....	20
Figure 2.1. Representative picture of as received (a) HDPE and (b) Hollow GMB....	39
Figure 2.2. (a) Brabender, (b) Mechanism of blending and (c) Composite.....	40
Figure 2.3. Representative image of work flow.....	41
Figure 2.4. MFI measuring equipment.	41
Figure 2.5. Schematic diagram of single screw extruder.....	43
Figure 2.6. Experimental setup of extruder.	43
Figure 2.7. Block diagram of FFF 3D printer.....	44
Figure 2.8. Representative picture of FFF based Aha 3D printer.....	45
Figure 2.9. 3D Profilometer.....	46
Figure 2.10. Representative image of (a) meshed FGF beam, (b) meshed FGFSF beam and (c) boundary and loading conditions.....	48
Figure 2.11. Schematic representation of experimental set up for estimating buckling load and free vibration.....	50
Figure 2.12. Representative load and deflection graph for evaluating P_{cr} using (a) DTM and (b) MBC method.	50
Figure 2.13 Representative image of sample tested for free vibration.	51
Figure 2.14. Details of modal analysis display in DEWESOFT.....	51
Figure 2.15. (a) Procedure of numerical analysis and (b) Meshed image of FGF.....	53
Figure 2.16. Experimental setup for thermal buckling experiment.	54
Figure 2.17. Heating condition (a) case-1, (b) case-2 and (c) case-3.	54

Figure 3.1 (a) SEM image of filament cross section (b) filler sustainability in filament and (c) extruded H60 filament	58
Figure 3.2. Representative print images (a) at 80-120°C bed temperatures with 45-75°C chamber temperature range (b) of SH20; Micrographs of (c) delamination at skin-core interface (d) delamination within layer and (e) defect free sample.	63
Figure 3.3. Prints through (a) N1 and (b) N2.....	65
Figure 3.4. (a) Schematic representation of the prime pillar, print (a) without and (c) with prime pillar.....	66
Figure 3.5. Warp in representative (a) H60 (core) and (b) SH60.....	67
Figure 3.6. Representative sandwich prints for effect of (a) layer offset and (b) print speed.	68
Figure 3.7. Freeze fractured micrographs of representative 3DP sandwich (a) using lower and (b) suitable printing parameters from Table 3.1 (c) micrograph of the sandwich along thickness.....	70
Figure 3.8. Sandwich (a) model and (b) mesh and (c) boundary conditions used in FE analysis.....	71
Figure 3.9. Temperature distribution in (a) sandwich (b) thickness direction (c) top skin (d) core and (e) bottom skin.	73
Figure 3.10. Stress (MPa) distribution in (a) SH60 (b) along the thickness.....	73
Figure 3.11 (a) Temperature and (b) stress distribution along the sandwich thickness post printing.	75
Figure 3.12 3D Printing strategy for FGF and FGFSF	77
Figure 3.13 Representative SEM images of (a) FGF interfaces and (b) GMB Sustainability.....	78
Figure 3.14. Micro CT of (a) FGF-1, (b) FGF-2 and (c) FGFSF-2.	79
Figure 3.15. Surface roughness of (a) HDPE and (b) H60.	80
Figure 3.16. Surface roughness profile curve of 3D printed sample in different directions of printing.....	81
Figure 4.1. (a) Experimental Setup for flatwise compression (b) test in progress and (c) representative sample deformation post compression.....	88
Figure 4.2. Representative Stress-Strain Plots of 3D printed (a) H, (b) Plain (H20, H40 and H60) and (c) functionally graded (FGF-1, FGF-2 and FGF-3) samples.....	89

Figure 4.3. (a) Compressed representative FGF print (b) post tested FGFs.	93
Figure 4.4. Representative freeze fractured 3D printed sample showing (a) material flow around GMBs and (b) void elongation and collapse during compression.	93
Figure 4.5. Representative of filler sustainability in (a) pre-tested and (b) post tested samples and (c) at the interface.	94
Figure 4.6 Representative (a) SEM of post-tested sample and (b) filler failure mechanism.	95
Figure 4.7. 3D printed FGSF-2 mounted in UTM.	95
Figure 4.8. Compressive response (a) FGSFs and (b) Collapse of interface and filler.	96
Figure 5.1. Three Point bending test of FGF-3 (a) Initial mounting on fixtures (b) post yield zone (c) Sever deformation (d) FGSF-3 sever deformation.	100
Figure 5.2. Stress-Strain response of 3D printed FGFs.	100
Figure 5.3. FEA results of FGFs (a) stress distribution in X-axis (b) Von-misses stress and (c) deformation.	102
Figure 5.4. Stress-Strain response of 3D printed FGSFs'	104
Figure 5.5. FEA results of FGSFs (a) stress distribution in X-axis (b) Von-misses stress and (c) deformation.	105
Figure 5.6. Fractured FGSF-2.	107
Figure 5.7. Comparison of FGF and FGSF (a) Specific modulus and (b) specific strength.	108
Figure 5.8. SEM of graded foams (a) GMB sustainability (b) HDPE and core interface (c) interface among (d) layer diffusion at fractured cross section and (e) de-bonding.	109
Figure 5.9. Property chart (a) flexural modulus and (b) flexural strength.	111
Figure 6.1. (a) seamless deposition between two adjacent layers (b) interface between H and H20 in 3D printed FGF – 1 and (c) GMB sustainability.	113
Figure 6.2. Representative FGF in (a) pre and (b) post buckling regimes.	114
Figure 6.3. load and deflection graph of HDPE and FGFs'	114
Figure 6.4. Representative load and deflection graph for evaluating P_{cr} using (a) DTM and (b) MBC method.	115
Figure 6.5. Load-deflection comparison of (a) FGF-1 (b) FGF-2 and (c) FGF-3.	116

Figure 6.6. FGFs Vs variation of Bardella-Genna modulus along the thickness of (a)FGF-1 (b)FGF-2 and (c)FGF-3.	117
Figure 6.7. (a) FRF plot of FGF-2 and plots for comparing effect of uniaxial compressive force on natural frequencies at (b) Mode 1 (c) Mode 2 and (d) Mode 3.	118
Figure 6.8. Representative plot for damping factor among different (a) Modes for FGF-1 and (b) FGFs.....	120
Figure 6.9. (a) Representative plot for evaluating P_{cr} using VCT and (b) comparison of DTM, MBC and VCT.....	121
Figure 6.10. Buckling Load of different closed cell foams.	122
Figure 6.11. 3D printed FGSF-2.	123
Figure 6.12. SEM images of (a) As casted layers (b) Filler sustainability of H60 (c) H-H20 interface and (d) H60-H interface of freeze fractured 3DP samples.....	123
Figure 6.13. Representative image of (a) Pre and (b) post buckling state of FGSF-2.	124
Figure 6.14. Representative (a-c) BGM variation, (d) load and deflection graphs of H and FGSFs.....	125
Figure 6.15. Evaluation of P_{cr} of FGSF-1 using (a) DTM and (b) MBC (c) Comparison of P_{cr} between FGSF and FGF.	126
Figure 6.16. Comparison of Load-deflection graphs of (a) FGSF-1 (b) FGSF-2 and (c) FGSF-3.	127
Figure 6.17 Representative FRF curve of FGSF-3.	129
Figure 6.18. Representative plot of load-damping factor among (a) different modes of FGSF-1 and (b) FGSFs.	130
Figure 6.19. Comparison of Critical buckling load and densities among different foam based sandwich beams.	131
Figure 7.1. Interface of H40-H60-H.	133
Figure 7.2. Representative picture of (a) sensor arrangement to measure temperature across cross-section (b) SEM of syntactic foam, and (c) Heat flow with respect to GMB percentage.	134
Figure 7.3. Represents images of case-1 (a) Heating position and (b) temperature distribution.	135

Figure 7.4. Temperature versus deformation graphs of case-1 for (a) Plain (b) Plain-Sandwich (c) FGF's and (d) FGFS's.	136
Figure 7.5. Local softening.	137
Figure 7.6. Representative images of case-2 (a) Heating position and (b) temperature distribution.	138
Figure 7.7. Temperature versus deformation graphs of case-2 for (a) Snap through buckling (b) Plain (c) Plain-Sandwich (d) FGF's and (e) FGFS's.....	139
Figure 7.8. Buckling of (a)SH20 (b) FGF-1 (c) mode-1 buckling shape of FGF-1 and (d) sample with no delamination.....	141
Figure 7.9. (a) Heating condition and (b) Temperature distribution.....	142
Figure 7.10. 3DP HDPE sample (a) Before testing (b) while testing and (c) post buckling.....	142
Figure 7.11. Dimensional buckling of H40.	143
Figure 7.12. Temperature versus deformation graphs of case-3 for (a) Plain (b) Plain-Sandwich (c) FGF's and (d) FGFS's.	144

LIST OF TABLES

Table 1.1. Classification of AM (ASTMF2792-10).	18
Table 1.2. Previous work inputs on 3D printing and functionally graded materials. ..	22
Table 2.1. Represents as received properties of HDPE HD50MA180 grade.	37
Table 2.2. Represents properties of hollow GMB (iM30K grade)*	38
Table 2.3. Specifications of single screw extruder.	44
Table 2.4. Specifications of FFF based aha 3D printer.....	45
Table 3.1. Optimized printing parameters of FFF.	60
Table 3.2 Evaluation of substrates used for 3DP.....	61
Table 3.3. Material properties used for FE simulation.	74
Table 3.4. Temperature and stress distribution along the sandwich thickness computed from FEA.	74
Table 3.5. Surface roughness values of HDPE and H60.	80
Table 3.6. Average surface roughness of foams.	81
Table 3.7. Amplitude parameters along thickness direction & along width direction.	81
Table 3.8. Density and weight saving potential of FGFs'.	82
Table 3.9. Density and weight saving potential of FGSF.	82
Table 4.1. Compressive properties of 3D printed FGFs.	89
Table 4.2. Specific properties of plain and FGFs.	91
Table 4.3 Compressive properties of FGSFs	96
Table 5.1. Density and Flexural Properties of FGFs.	100
Table 5.2. Specific Properties of FGFs.....	101
Table 5.3. Position of neutral axis.	103
Table 5.4. Experimental and FEA comparison of graded foams.....	103
Table 5.5. Experimental flexural properties of FGSFs'	104
Table 5.6. Specific properties of FGSFs'	104
Table 5.7. Neutral axis position in FGSFs'	106
Table 5.8. Experimental and FEA comparison of FGSFs'.	106
Table 6.1. Experimental and numerical P_{cr} of FGFs'.	115
Table 6.2. Influence of uniaxial compressive load on natural frequencies of FGFs.	119
Table 6.3. Influence of uniaxial compressive load on damping factor of FGFs.....	119

Table 6.4. Comparison of natural frequency under no load condition.	120
Table 6.5. Experimental critical buckling load of FGSFs.	126
Table 6.6. Experimental and theoretical critical buckling load of FGSFs.	128
Table 6.7. Natural Frequencies of FGSFs.	128
Table 6.8. Experimental and numerical comparison of FGSFs under no load condition.	129
Table 6.9. Damping Factor corresponding to first three modes of FGSFs.	130
Table 7.1. Case-1 buckling temperature of 3D Printed Samples.	136
Table 7.2. Buckling temperatures of case-2.	141
Table 7.3. Buckling temperature of case-3.	145

ABBREVIATION

ASTM	: American Society for Testing and Materials
AM	: Additive Manufacturing
CTE	: Coefficient of Thermal Expansion
CM	: Compression Molding
DAQ	: Data Acquisition System
DSC	: Differential Scanning Calorimetry
DTM	: Double Tangent Method
FFF	: Fused Filament Fabrication
FFT	: Fast Fourier Transform
FDM	: Fused Deposition Modeling
GMB	: Glass Microballoon
HDPE	: High Density Polyethylene
MBC	: Modified Budiansky Criteria
MFI	: Melt Flow Index
PMC	: Polymer Matrix Composite
SEM	: Scanning Electron Microscope
SF	: Syntactic Foam
UTS	: Ultimate Tensile Strength
VCT	: Vibration Correlation Technique
3DP	: 3 Dimensional Printing

NOMENCLATURE

ω_j	Angular natural frequency	rad/s
α	Angle formed between ω 's	°
T_{cr}	Critical buckling temperature	°
P_{cr}	Critical buckling load	N
ρ_m	Density of the matrix	kg/m ³
ρ_c	Density of the composite	kg/m ³
ρ_f	Density of the filler	kg/m ³
ε	Damping factor	
ρ_{exp}	Experimental density	kg/m ³
E_f	Flexural modulus	MPa
σ_{fm}	Flexural stress	MPa
p	Load	N
L	Span length	mm
m	Slope of the tangent	----
ρ_{th}	Theoretical density	kg/m ³
t	Thickness	mm
ϑ_m	Volume fraction of matrix	%
ϑ_f	Volume fraction of filler	%
\emptyset_v	Void percentage	%
w	Width	mm

1. INTRODUCTION

1.1 Composite Materials

The present world formulation concept is vast as it concerns many industries which manufacture products by mixing various materials at different proportions. To be more precise, a formulation can be stated as combining or mixing various ingredients of natural or synthetic origin, which are primarily non-reactive with each other, such that the final product satisfies the desired specification. As the ingredients are non-reactive, the final product consists of multiple immiscible phases. This basic concept of formulation is applied in developing composite materials. Composite materials, as defined by the ASM Handbook (ASTM D3878-18), are the mixture of two or more distinct materials with a visual interface. Generally, the composite material has two constituents: the primary is a matrix, and the secondary is reinforcement. Here matrix is the continuous phase, and reinforcement is a discontinued phase. This matrix and filler can be any metal, polymer, or ceramic material. The properties of the composite depend on the percentage and type of matrix and filler material, shape and size of the filler, and interphase of the filler and matrix. The capability of exhibiting better specific properties and weight reduction potential made these composite materials significant in various applications, namely light structures, sports, aerospace, automotive, packaging, acoustic, and medical applications (Hsissou Rachid et al. 2021). Boeing 787 and Airbus A350, which contain almost 50 and 53% share of composite materials, were the best examples to show the potential of composite material for Aviation applications (Tang XC et al. 2018). As the properties of the composite can be tailored in many ways, many researchers are developing hybrid composites by changing the orientation of fibers, volume fraction, etc., to achieve enhanced properties (Gangil Brijesh et al. 2019, Hemath Mohit et al. 2020, Laishram Rokesh et al.).

1.2 Classification of composites

These composites are classified into a ceramic, polymer, and metal composite based on matrix material. They are classified into micro and Nano composite based on reinforcement size and further classified as filler, short and continuous fibre

reinforced composites based on the type of filler. The broad classification of composite based on the filler is mentioned in Figure 1.1. Every type of composite has its advantages. For example, reinforcing fillers with good tensile strength and higher modulus helps the polymer matrix enhance mechanical and thermal properties (Das Pallab and Pankaj. 2019, Datsyuk V et al. 2020). Moreover, compared to metal composites, polymer composites offer flexibility to the manufacturing process. Thus, complex shapes can be developed. The other advantages include their lower density, which results in minimum fuel consumption (for aviation and automobiles), high speed in competitive sport, or for longer range missiles and places where there is a need for higher payload (Tarhini AA and AR. 2019, Vaggar Gurushanth B and SC. 2020). The two most common types of polymers are thermoset and thermoplastic ones. The chains of thermosetting polymers are rigidly connected by strong covalent bonds, making them insoluble and infusible. Phenolic, melamine, vinyl esters, vulcanized rubber, epoxy resin, and silicones are examples of thermosetting plastic materials that are frequently encountered daily. The bonds in thermoplastics are weak, which causes them to melt under intense pressure and heat. Polyvinyl chloride, polybenzimidazole, polyethylene, acrylic, polypropylene, Teflon, and nylon are a few typical examples of thermoplastics. A thermoplastic or thermosetting resin that has been reinforced with fillers like fibres, particles, etc. makes up polymer matrix composites (PMCs).

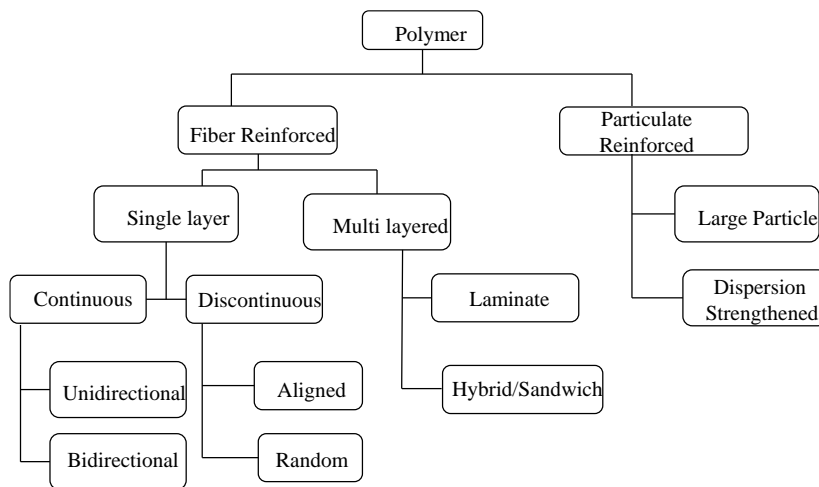


Figure 1.1. Composite classification with respect to filler.

1.3 Syntactic Foams

These foams are initially developed in 1960 for marine and structural applications. Syntactic foams are the type of composite material where the hollow particles are reinforced as the filler in the matrix. These foams possess a wide range of mechanical properties, which helps in exhibiting multifunctional advantages (Breunig PETER et al. 2020). As these are developed by reinforcing hollow particles, these foams have better weight saving potential, making these syntactic foams one of the preferable core materials in sandwich structures (Bharath H. S et al. 2021). These advantages made researchers develop various thermoplastic and thermosetting based syntactic foams (Doddamani MR and SM. 2011). Syntactic foam properties can be varied by altering the properties of the filler. This turns the researcher's focus towards observing the behavior of the syntactic foam when metal, ceramic, and silicon based hollow particles are used as reinforcement. (Gupta Nikhil et al. 2013). (Gupta Nikhil et al. 2005) observed that these foams offered high specific strength and low thermal conductivity. Due to their lightweight, these foams have great potential for buoyance and damping applications (Sadanand et al. 2021). The properties and weight reduction potential of these syntactic foams also depend on the sustainability of the filler in the matrix (Jayavardhan ML et al. 2017, Kumar BR Bharath et al. 2016).

In general, these syntactic foams have two phases' matrix and reinforcement. This syntactic foam is of two types primary is open cell foam, and secondary is closed cell foam. Open cell foam has comparatively less mechanical properties among these two due to the presence of interconnected pores. This made a researcher develop closed cell foam. However, during the manufacturing of these closed cell foams, air entrapment may result in the formation of voids. These voids help in enhancing the weight reduction potential. Here these voids act as the third phase of the composite. Similarly, when these foams are reinforced with the short fibre it acts as multiphase material (Figure 1.2).

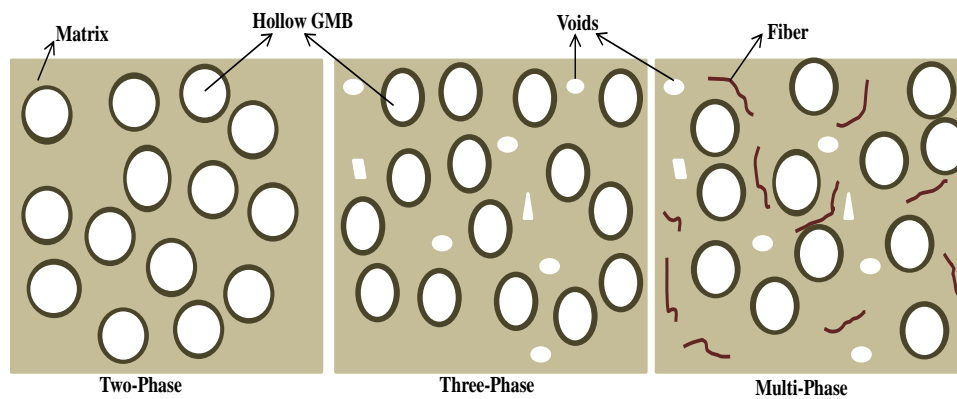


Figure 1.2. Multiple phases of syntactic foams.

1.3.1 Filler

The choice of filler is determined by the properties needed and the intended applications. The thermoplastic industries have made considerable use of both inorganic and organic solid fillers (Chen H. C et al. 2006, Liu H et al. 2008). Surface, electrical, mechanical, and thermal properties can also be altered by varying the percentage of filler in a matrix (Jayavardhan M. L and Mrityunjay. 2018, Jayavardhan ML et al. 2017). Besides improving the mechanical and thermal properties, reinforcing the filler in the matrix also helps control the resin cost (Annigeri Ulhas K and B. 2018). Various options, including industrial waste, metal, ceramics; bio waste, etc., can be used as reinforcement. These fillers are classified based on size, shape, and chemical composition. Based on the size, they are divided into three types (1) macro, (2) micro, and (3) nanofillers. The macro fillers are those which have their size in a macro range, such as natural fibres like sisal, banana, jute, etc., synthetic ones like glass, carbon, etc., the micro fillers are those fillers that have their size in a micro range such as glass micro ballons (GMB) (H S Bharath et al. 2020), bio-active glasses (BAG) (Jeyachandran Praveen et al. 2021), fly-ash cenospheres (Patil Balu et al. 2019), etc . while the nanofillers are those which have their size in nano range such as carbon nanotubes (CNT), graphene, etc. (Kumar Sumodh et al. 2022). Based on chemical composition, they are classified as (1) Inorganic and (2) organic fillers. Here fillers like zinc (Zn), silver (Ag), cobalt (Co), iron (Fe), and metal oxides like TiO_2 , Fe_2O_3 , Al_2O_3 , ZnO , etc. are examples of inorganic fillers. The metal oxides are specifically developed to increase the fillers' efficiency, tailorability, and reactivity. $\text{TiO}_2 / \text{ZnO}$ (Pan Lun et al. 2015), Fe_2O_3 (Masood SH and WQ. 2004), Al_2O_3 (Singh

Rupinder et al. 2016), etc., are the most frequently used metal oxides fillers (Chris. 2011). Fillers like Carbon fibre, Carbon black, CNT, graphene, graphite, fullerenes, etc., are a few examples of organic fillers. The broad classification of fillers is shown in Figure 1.3. Among the various fillers mentioned above, the hollow glass micro balloon was considered as reinforcement in the current work.

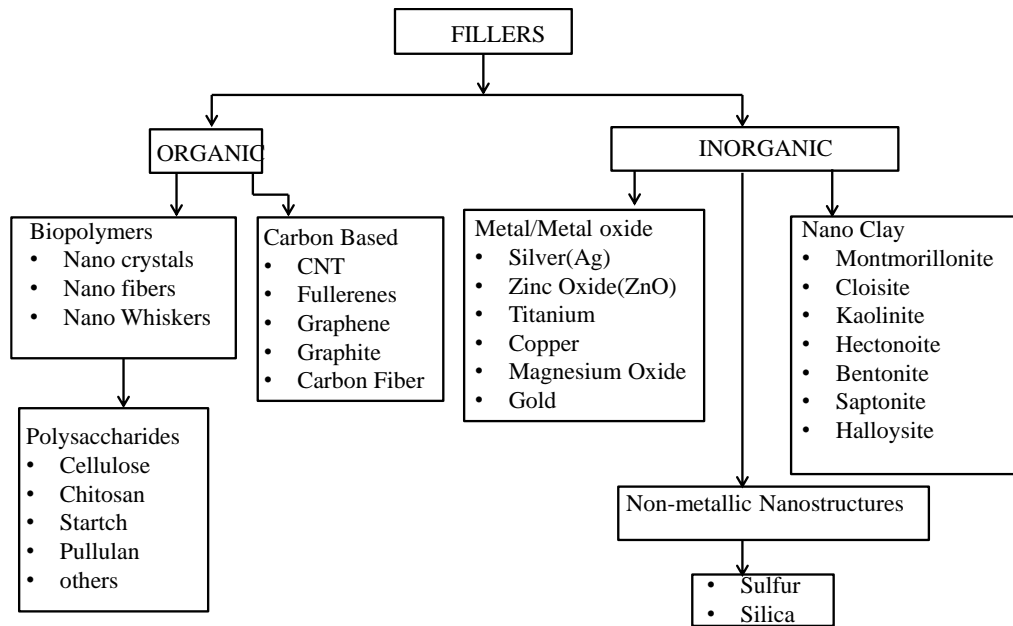


Figure 1.3. Classification of filler.

GMBs are a free-flowing powder developed in 1960 from the manufacturing of solid glass beads. There are various commercial methods through which GMBs can be developed. Due to the availability of raw materials and the advancement of manufacturing technologies, GMBs are less expensive than polymeric ones (Kumar Sumodh et al. 2022). These GMBs are developed in an upward tube heater. Here the tube is heated using gas that contains propane-butane. At the lower part of the tube, a glass and a porofore containing powder are splashed. Porofore is a synthetic blowing specialist that produces gas at the glass softening point and swells, to some extent, intertwined solid particles. The microspheres are then brought to the highest point of the cylinder by the hot gas, cooled, and washed with water to dispose of faulty microspheres. Further, these microspheres are subjected to acidic reactions to enhance the softening temperature and chemical resistance. Sodium silicate microballoons are produced using sodium silicate with ammonium pentaborate and further subjected to a

spray-drying process to form hollow microballoons (Lee SM and Peter. 1992). The scanning electron microscopic image of Hollow glass micro balloons used in the current works is shown in Figure 1.4.

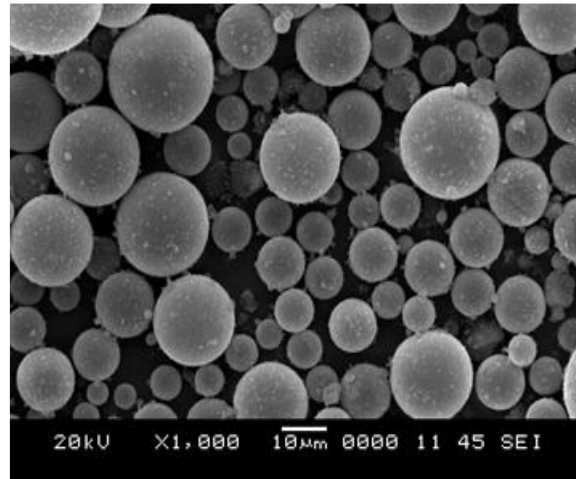


Figure 1.4. SEM of hollow GMB.

These hollow glass micro balloons come in different grades, where their physical properties like density, wall thickness, and crushing strength may vary from one another. Based on these properties, a specific grade GMB is selected for a specific application. Weight and strength are crucial parameters to consider for weight-sensitive applications. Developing the components for such applications using GMB reinforced composites is advantageous. It will be challenging and interesting to create novel and useful systems employing glass micro balloons with near isotropy.

1.3.2 Matrix

The matrix in the composite can be any metal, polymer, or ceramic material. In the current work, the matrix is selected as a polymeric material. Polymers are long chain repeated units of monomers formed by polymerization. These polymers offer advantages like good ductility, formability, and corrosion resistance. A wide variety of such polymers offers a manufacturer to improve product quality. Basically, these polymers are classified into two types named as thermo and thermosetting polymers. The major difference between these two is thermo polymer offers flexibility for recycling. Strong covalent bonds in thermosetting polymers hinder this recycling phenomenon. These thermosetting polymers exhibit rigid behavior even after

subjecting to the heating process, whereas when it comes to thermo polymers on heating, they get softened and can be moulded into the desired shape

(Arzamasov. 1989). This reusability is the major advantage for thermo polymers because it helps in the effective usage of material and resources; this is one of the main reasons for using thermo polymers for many structural and engineering applications. Polymers like polyethylene, polypropylene, polylactic acid, etc., are a few examples of thermoplastics, epoxy, Bakelite, and phenolic thermosetting. So far, there is a lot of work done on these thermo polymers like polylactide (Spoerk Martin et al. 2017), polyetherimide (Arivazhagan Adhiyamaan et al. 2014), polymethyl methacrylate (Espalin David et al. 2010), polycarbonate (Domingo-Espin Miquel et al. 2015), etc. The capability of some polymers to replace metals in small devices and structural applications brings the name engineering plastic to the classification of plastics. Among the available multiple polymers, few plastics are most suitable for developing composite, which can offer better specific strength and modulus and atmospheric and chemical inertness (B John and Nair. 2014). Polymer matrices are frequently employed in composites. This is because of the inherent characteristics of polymers. The price of PMCs can be minimized by reinforcing the plastic with inexpensive fillers like hollow GMBs. The increasing usage of plastic daily has boosted the demand for plastics in India. Polymers are mostly observed in every aspect of daily routines, like water bottles, food packages, cloth fabrics, toys, vehicle bodies, etc. From the analysis done on predicting plastic usage, it is observed that India had one of Asia's lowest per capita plastic usage rates in 1997, estimated at 0.800 kg. The anticipated demand in the year 2000 AD was 2.16 kg/capita. Due to economic liberalization, India has seen a rise in plastic consumption since 1991. India's plastic use doubled from 0.85 million tonnes in 1990–1991 to 1.79 million tonnes in 1995–1996. Demand for commodity plastics is rising at a 15% annual rate. The All India Plastic manufacturers association estimates that in 1995, there was a total production capacity of 1.39 million mega tonnes (MMT) for PVC, PS, PP, and PE, with 1.8–1.9 million mega tonnes of demand in 1996–1997. According to data from Plast India, this is split into three main sectors: infrastructure (30% of the total), which includes bridges, buildings, energy, roads, and telecommunications; packaging

(25%); and water and agriculture (24%). India's polymer usage is shown in Figure 1.5. About half of this consumption is made up of polymers used in packaging.

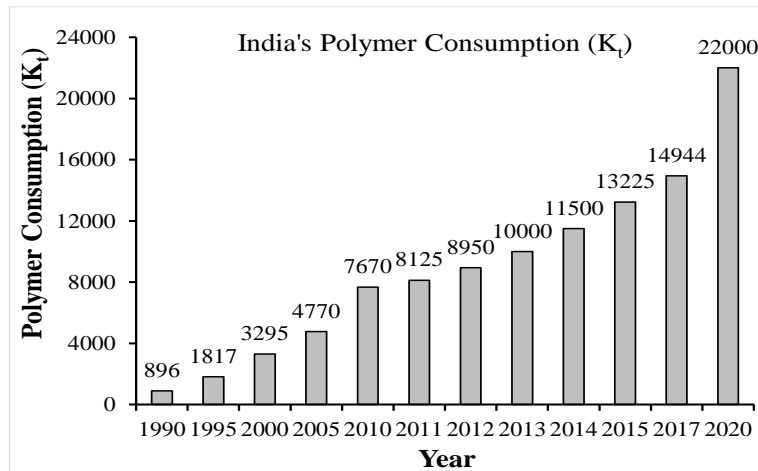


Figure 1.5. Polymer consumption in India (ShekharB. 2012).

With such a growth rate in plastic consumption, adopting composites like thermoplastic syntactic foam composite developed by reinforcing the Hollow GMB helps solve the issues regarding plastic management and environmental issues. Apart from these, whenever some filler is reinforced in a matrix, the filler matrix interface and their compatibility need some attention.

1.4 Functionally Graded Composite Structure

Functionally graded structures are the beams in which the property of the material changes with any one or more dimensions of the beam, i.e., beams property can be defined by material function $f(x)$. Inhomogeneous beams, $f(x)$ remains constant. The determination of compositional gradient and the process of making a functionally graded beam depend on its intended use. Japanese researchers in the 1980s initiated functionally graded materials (FGMs) as an application in constructing thermal barriers to withstand high temperatures for space aircraft projects. (Zhong Zheng and Tao. 2007). As per previous studies, there are four different ways to incorporate material variation along the thickness direction (a) Orientation gradient type, (b) Size (of material) gradient type, (c) Fraction gradient type, and (d) Shape gradient type (Figure 1.6).

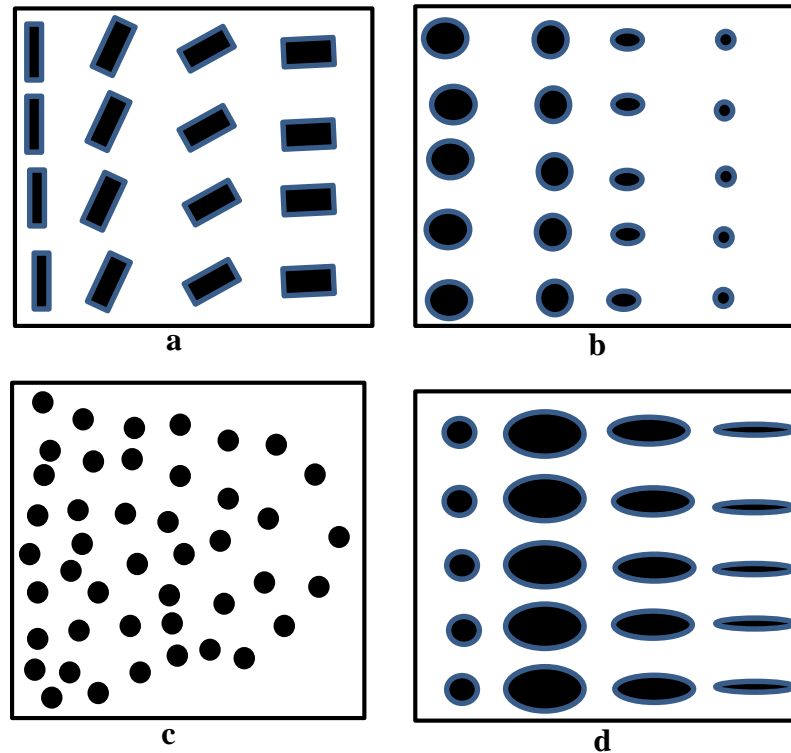


Figure 1.6. Various types of gradation.

FGMs gradually transition between the various material components, which can significantly lower the failure of the delamination and cracking frequently seen in laminated composite materials. Furthermore, it is possible to develop and optimize the volume percentage of various materials to fulfill certain specifications (Liu Zhihui and Junchuan. 2018). Due to their numerous benefits, FGMs are now being used in various industries, including the aerospace sector, turbine blades, and weapon armor, in addition to thermal barrier systems (Bhavar Valmik et al. 2017, Toudehdehghan Abdolreza et al. 2017). With the advancement of FGMs and their tremendous potential, it is conceivable that they will spread their wings in various industries. Many analytical and numerical works were done on these FGMs to predict their behavior under different loading and boundary conditions. In order to study the thermal elastic behavior of FGM beams, (Chakraborty A et al. 2003) developed a novel beam element based on the first-order shear deformation theory. The unified approach for analyzing FG Timoshenko and Euler-Bernoulli beams' static and dynamic and static behavior was thoroughly addressed (X-F. 2008). (Neves AMA et al. 2012) worked on analyzing the buckling behavior of FG sandwich plates and observed that critical buckling load exhibited an inverse relation to the exponent of

the power law. (Ebrahimi Farzad and Ali. 2016) developed a Navier solution approach that is used to examine the thermo mechanical vibration properties of FG beams formed by porous material and subjected to various heat loadings. Beams developed by varying the volume percentage of the hollow particles along the thickness direction are called functionally graded syntactic foam (FGSF) (Nikhil. 2007). Adopting graded foams instead of plain foams helps enhance energy absorption capacity (Nikhil. 2007). (Doddamani Mrityunjay et al. 2015) developed FGSFs using a layered curing technique, and these developed FGSFs are subjected to flexural and compressive testing. Results showed that the graded foams outperformed the plain foams by enhancing the specific properties. Though there are advantages of replacing the graded foams with plain beams, manufacturing methods to develop or manufacture these beams are limited. Therefore in the current work 3D (three dimensional) printing of functionally graded foams (FGFs) was explored. The main advantages of this method were it can eliminate the material wastage and gives the flexibility to print critical parts with less human effort. The possible defects in graded beams like delamination can be avoided by choosing the proper printing parameters.

1.5 Sandwich

The core structures in which the top and bottom faces are stacked with stiff skin are named the sandwich structures (Figure 1.7). When this material property of core material is constant throughout the thickness, it is named a plain sandwich structure (Figure 1.7a). When this material property varied along the core's thickness, it is named functionally graded sandwich structure (Figure 1.7b). The material selection for these sandwich structures depends on the quality, cost, and required application. A wide variety of materials available for the face sheet and core increase the possibility of a sandwich showing its significance in multifunctional benefits. Generally, lightweight material is selected as the core material for the sandwich. The separation of the facings by a lightweight core greatly enhances the second moment of area of the material cross-section and the bending stiffness with only a little increased weight. This is called to be as “sandwich effect”. The development of sandwiches for structural applications helps enhance strength, specific properties, fatigue life, and functional benefits (Birman Victor and George. 2018, Elamin Mohammed Eltayeb

Salih et al. 2018). All these attractive properties made the sandwich structures find their application in aerospace, marine, and civil industries (Jiang Li-li et al. 2014).

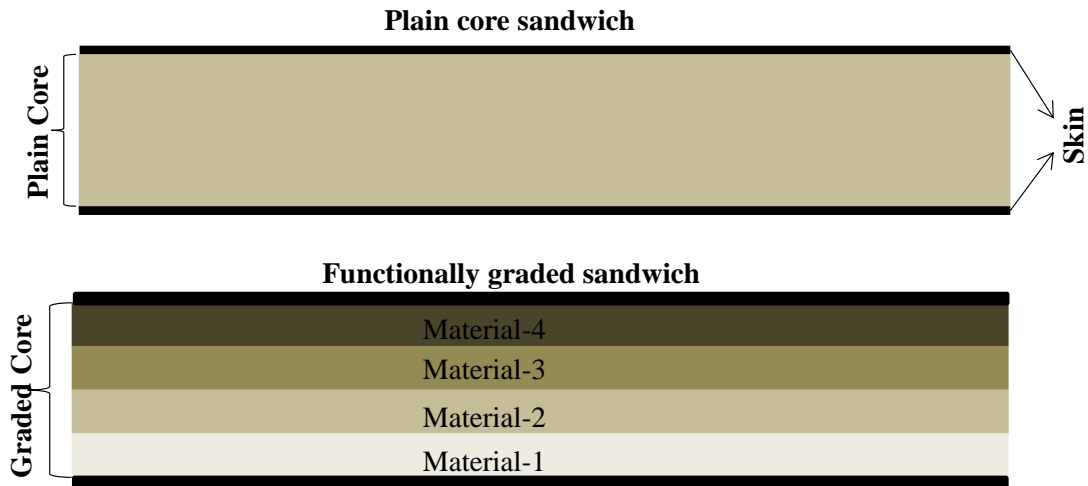


Figure 1.7. Types of sandwich.

Initially, these sandwich structure theories were introduced in 1849 CE (A. K. Noor et al. 1996). But the potential of the sandwich design was improved while world war-2. Due to advancements in aircraft, there is a desire for lightweight, highly robust, and damage-resistant structures. Composites with these characteristics are the best option for many situations where weight is an issue. The sandwich structures property depends on the material of the core, skin, and their respective thickness. The necessary qualities and application determine the thickness of the core and skin. The loading conditions influence the choice of material for sandwich composites, price, quality, availability of constituent materials, and functional needs. For example, Aerospace structures frequently use multi-layered graphite and carbon epoxy facings, while civil and marine systems' frames use glass epoxy or vinyl esters (Birman Victor and A. 2018). The damping and load-bearing capability of the sandwich structures are greatly influenced by the core and skin's design, thickness, and material (Yuan Chongxin et al. 2012). The properties of the sandwich can be altered by varying the selection of suitable matrix and filler materials, as well as volume fractions of constituents. Depending on the application and performance requirements, various materials can be employed as the core (R. 2018). The most commonly used core materials in sandwich structures are closed and open cell foam, honeycomb structures and corrugated high-density material in the shape of a truss, etc. The strength of the sandwich structure mainly depends on the core material, hence using closed cell foam

instead of open cell foam helps in improving the impact strength, modulus and also controls the moisture absorption (Doddamani MR and SM. 2012, Zhang Jianxun et al. 2014, Zhang Jianxun et al. 2016). The sandwich structures property can also be enhanced by effectively controlling the porous size, varying the wall thickness and size of the hollow particle, and laminating the core with much stiffer skin (Omar Mohammed Yaseer et al. 2015, Qin Qing-Hua et al. 2014). The control over the property enhancement depends on how effectively the reinforcement has been introduced into the matrix, so the optimization of the maximum volume percentage of the filler is essential. So far, multiple core structures such as tetrahedral lattice(Kooistra Gregory W et al. 2008), honeycomb(Park S et al. 2012), pyramidal lattice(Wadley Haydn NG et al. 2003), body-centered cubic lattice (Mines RAW et al. 2013). These sandwich structures are primarily used in applications where the object is subjected to impact loading. Hence the interface strength of the skin and core is essential as it plays a crucial role in load transfer. Therefore if a sandwich structure is developed concurrently, possible defects like delamination can be eliminated. This single-stretch development of the sandwich structure is possible through 3D printing, considered the manufacturing method in the current work.

1.6 Processing of syntactic foam

Each system of materials has unique physical, mechanical, and processing characteristics. It is necessary to use an appropriate manufacturing method to shape the material into its final form. In the twentieth century, the processes used to create items using composite materials transitioned to sophisticated microprocessor systems from skilled labor operations, which can automate the system. Whereas earlier people used hand layup and spray-up methods to develop molds using mixed raw materials and curing them at room temperature. Due to the advantages of PMCs, these synthetic materials are now used in almost every other sector of the global economy, from consumer goods to automotive and marine to the main structural applications of aeroplanes and bridges. Increasing these PMCs in various product applications necessitates expanding design methodologies, material technology, and production procedures. To fabricate syntactic foams (SFs) effectively, the production process must be properly organized to reinforce hollow particles into the resin. The inevitable

result of increasing matrix porosity and particle breakage can be avoided by stabilizing gas bubbles in the polymer matrix. The manufacturing processes (Figure 1.8) must minimize clusters without affecting the reinforcement, wet homogenous reinforcement dispersion in the resin material, and prevent the fracture of hollow particles.

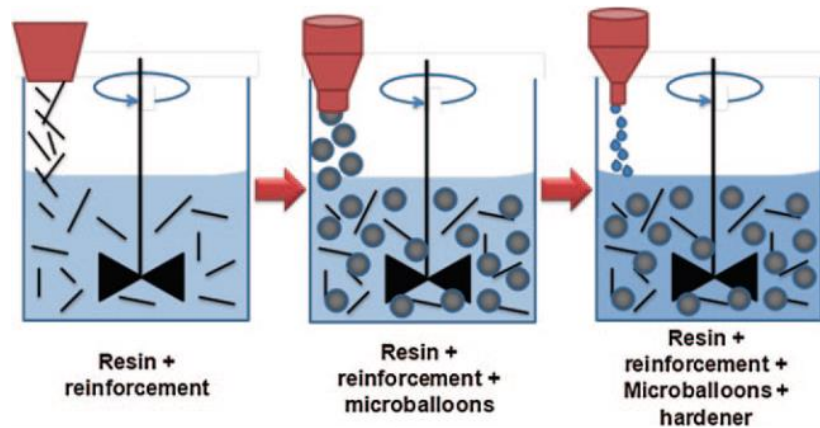


Figure 1.8. Preparation of syntactic foam.

The manufacturing of this multiphase syntactic foam includes three stages. In the first stage, fibre is dispersed in the resin, and in the second stage, hollow particles are dispersed and stirred well so that the fillers' uniform dispersion occurs. Once the uniform dispersion and viscosity is reached, in the third step hardener was added to the resin, and to distribute it, the solution was stirred at low speed. Then this resin solution is poured into the mold and cured at room temperature. Basically, these mold methods are divided into two types: primary is the open mold process, and secondary is the closed mold process. The open mold process is further classified into oven cured, autoclave, and hand layup. The closed molding process is divided between compression mold, injection molding thermo stamping, and transfer molding. A brief classification of this thermo and thermosetting plastic is shown in Figure 1.9.

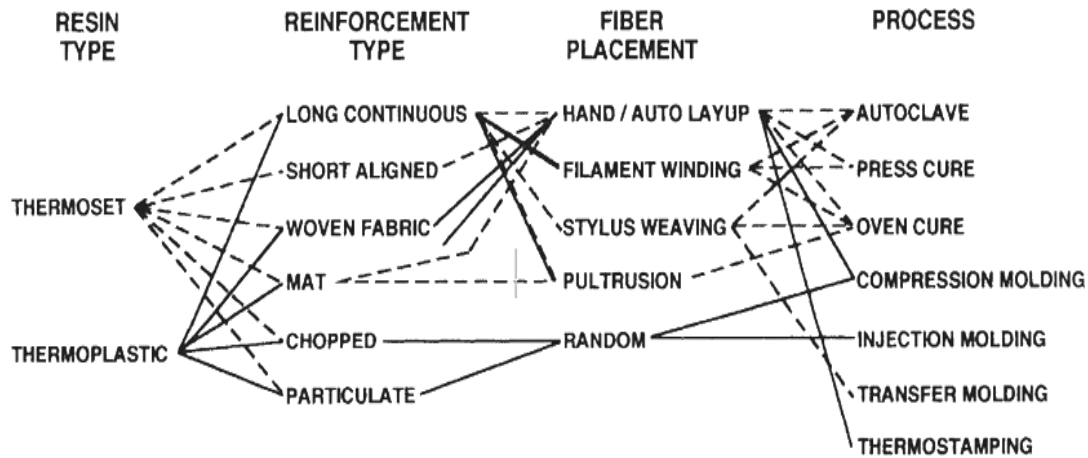


Figure 1.9. Classification of plastics.

Previously Injection and compression molding methods are mostly used for processing thermoplastic products. But in the current scenario, 3D printing has taken a gain, offering much flexibility with less material wastage and human effort to prepare the same component.

1.6.1 Compression Moulding

Compression molding is a traditional manufacturing method. In this method, we generally use two match plates, one fixed and the other movable. Initially, the thermoplastic composite layup is placed in the mold and subjected to preheating at a specific temperature per the material's constituents. It is further subjected to pressure by applying the hydraulic load so the material molds into the desired shape. At constant pressure, this is subjected to a curing process in an oven. Combined loads of thermal and mechanical helps in controlling the void formation and improving the surface finish. Advanced composite thermoplastics with unidirectional tapes, woven textiles, a sheet of randomly oriented fibres, or chopped strands can also be compressed and molded. Compression molding is a more affordable alternative to injection molding and stamping. When thermosets are subjected to compression molding, the mold remains hot for the whole process. A new charge of moulding powder should be supplied as soon as a molded component is evacuated. Contrary to thermosets, thermoplastics need to cool in order to solidify. Singh and his associate (Singh Manoj Kumar and Sunny. 2021) worked on evaluating the wettability and degradation behavior of compression molded kenaf reinforced high density

polyethylene (HDPE). They observed that these composite exhibited more tendency towards the absorption of water and less towards vegetable oil. As of now, so much research has been done on studying these compression molded parts. But comparatively, compression molding is less efficient than injection molding in terms of cycle time, part complexity, and yield volume.

1.6.2 Injection Moulding

The most popular production method for creating plastic parts is injection molding. Additionally, a wide variety of different sizes, designs, levels of complexity, and applications are produced using it. The injection molding machine contains a hopper through which material in the shape of pellets or granules is fed into the barrel, a lengthy screw inside the barrel, and a thermal heater to melt the pellets inside the barrel. In this process, the material placed in the hopper gets melted into a semisolid state and injected into the mold with the help of a rotating screw. Once the entire die was fed completely, it was allowed to cool and solidify to get the end product. Once it is completely cool part will be separated from the die. This process was mostly used in the thermoplastics industry due to its effective utilization of material, capability to create critical parts, higher and fast production rate, and a wide variety of material choices. Injection molding helps give precision parts at a low cost and reinforces hollow spheres in resins. Developing a part using this injection molding process helps develop the high strength part with good weight-saving potential (Bunn P and JT. 1993, Nikhil. and Eyassu. 2004). (Kumar BR Bharath et al. 2016) Studied the physical and mechanical characteristics of samples developed using injection molding. Though lots of work was done on processing syntactic foam through injection molded samples, the weight reduction potential was not so appreciable. This is due to the failure of hollow particles caused to pressure and extra shear forces. This problem of failure of hollow spherical can be overcome by replacing the injection molding method with 3D printing, considered the manufacturing method for current research work.

1.6.3 Additive Manufacturing

The driving forces behind advanced manufacturing are rapid expansion and advancements in the manufacturing sector for increased global competitiveness. Creating cutting-edge manufacturing technology and materials is essential for any nation's economic prosperity. Compared to traditional processing technologies, AM technology has developed quickly in recent years, slowly shifting the focus away from traditional methods to increase competitiveness in the manufacturing industry (Ahmed et al. 2016, Rezayat Hassan et al. 2015). A greater range of customization options increased productivity, flexibility, and lower production costs are all benefits of AM. AM also eliminates conventional part geometry limits by developing highly complex components with less material consumption and resources. It reduces the time from concept to commercialization by doing away with the need for expensive tooling and intricate drawings, enhances the renewable energy economy by lowering energy intensity, and brings about a paradigm shift in the design-to-manufacture process. Traditional subtractive methods of making parts, such as milling or lathing, remove material, whereas additive manufacturing (AM) develops a part by gradually adding material. Rapid prototyping is possible with additive manufacturing, and in a few cases, it can be applied directly to manufacturing for small-scale production. Moreover, with fewer facilities for small-scale critical part production, the part can be developed at a low cost. Designers might find this to be quite helpful since it can reveal elements that are challenging to discern from 3D models on a computer screen. Due to the quick evolution of AM methods, AM's applicability is no longer restricted to rapid prototyping. The medical, aerospace, and automotive sectors have benefited from the quick advancements in additive manufacturing processes that have moved them beyond prototypes to actual product development (Vijayavenkataraman Sanjairaj et al. 2017). The complete process chain of AM is represented in Figure 1.10. AM process is initiated with the part design. Here, the part to be developed is designed using CAD software or a 3D laser scanning technique. This designed model is saved in stereo lithographic (STL) format. This STL file can be opened using any slicing software that helps connect the 3D printer to the computer. Once the STL file

was imported into the slicing software, the part orientation was adjusted to how we wanted it to be developed. Further, all the printing parameters are given as input, and the path to be followed by the 3D printer nozzle is generated in the form of the G-Code. This G-Code is given as the user input to the 3D printer. Once the Machine starts, the part will be developed by adding the material layer by layer, following the generated path, until the entire part is completed successfully.

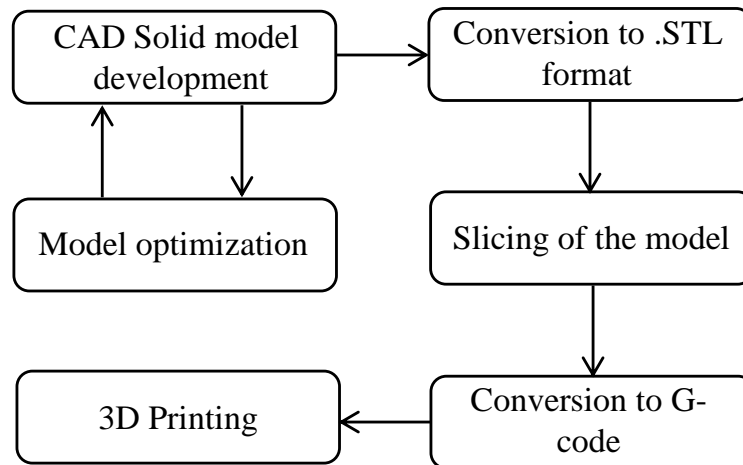


Figure 1.10. Flow chart of AM process.

Currently, in the market there are many AM processes. According to ASTM F42, these processes are broadly classified into seven types which are mentioned in Table 1.1, Among which four processes, namely fused filament fabrication (FFF), Multi-jet/Polyjet modeling (MJM), selective laser sintering (SLS) and stereolithography (SLA) can be employed for processing polymeric materials (David. 2017). The cost, required floor space, required material thickness, and layer heights of these systems vary from one another.

Table 1.1. Classification of AM (ASTMF2792-10).

Process Type	Brief Description	Related Technology	Companies	Materials
Binder Jetting	Liquid bonding agent is selectively deposited to join powder material	Powder Bed and Inkjet Head (PBIH), Plaster Based 3D Printing	3D system (USA), ExOne (USA)	Polymer, Foundry sand, Metals
Direct Energy Deposition	Focused thermal energy to fuse material by melting as the material is being deposited	Laser Metal Deposition (LMD)	Optomec (USA), POM (USA)	Metals
Material Extrusion	Material is selectively dispensed through a nozzle or orifice	Fused Filament Fabrication (FFF)/ Fused Deposition Modeling (FDM)	Stratasys (Israel), Bits from bytes	Polymers
Material Jetting	Droplets of build material are selectively deposited	Multi-Jet Modeling (MJM)	Objet (Israel), 3D system (USA)	Polymer, Waxes
Powder Bed Fusion	Thermal energy selectively fuses regions of powder bed	Electron Beam Melting (EBM), Selective Laser Sintering (SLS), Selective Heat Sintering (SHS) and Direct Metal Laser Sintering (DMLS)	EOS (Germany), 3Dsystem (US), Arcam (Sweden)	Metals, Polymers
Sheet Lamination	Sheets of material are bonded to form an object	Laminated Object Manufacturing, Ultrasonic Consolidation (UC)	Fabrisonic (USA), Mcor (Ireland)	Paper, Metals
Vat Photo Polymerization	Liquid photopolymer in a vat is selectively cured by light	Stereolithography (SLA), Digital Light Processing (DLP)	3D system (USA), Envisiontec (Germany)	Photopolymers

The FFF method is a developing AM technology that can produce objects without geometric limitations and offers numerous advantages like cheaper cost, wide material use, minimal environmental damage, and simple post-processing (Griffiths Chrisian A et al. 2016, Rinaldi Marianna et al. 2018, Wu Peng et al. 2016). S.Scott Crump invented this FFF process in the late 1980s and further, it was co-founded and commercialized in 1990 by Stratasys in 1990 (Tucker Katherine et al. 2014). Studies

on FFF product characteristics have recently been conducted to meet the specified design requirements, including surface roughness (Boschetto Alberto and Luana. 2016, Chen Han and Fiona. 2016), build quality (Caminero MA et al. 2018, Gordeev Evgeniy G et al. 2018, Narahara Hiroyuki et al. 2016), mechanical properties (Hwang Seyeon et al. 2015, Tsouknidas A et al. 2016) and dimensional quality (Chen Han and Fiona. 2016). The most popular method for employing 3DP procedures to reduce lead times is the FFF process. The FFF approach is depicted schematically in Figure 1.11.

In the current work, thermoplastic based plain, functionally graded core and their respective sandwiches are 3D printed using the FFF process. This FFF is a layer-by-layer addition process. In this process, the material is fed in filament form, and the heat required for melting the filament is supplied through thermo electric heaters. Initially, the model to be manufactured is designed in CAD software. The STL format is exported to any slicing software like simplify3D, quora, etc.; the path generated in this is supplied as input to the nozzle motion. To be considered appropriately, there are various parameters like layer height, infill percentage, number of skirt lines, extrusion multiplier, nozzle temperature, printing speed, number of outline perimeter shells, raster angle, bed temperature, etc., according to the material properties. FFF process adhesion bond between the sample and bed and safe removal of the sample without any warpage is the major thing to be taken care of while selecting the material to be 3D printed.

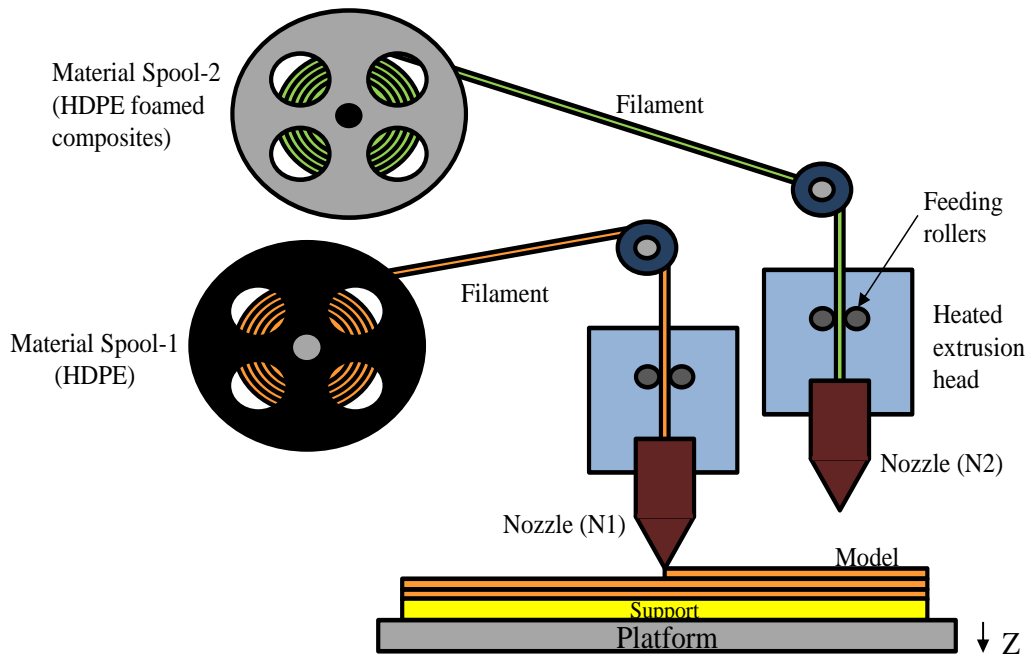


Figure 1.11. Representative image of FFF process.

Lots of work was done on the 3D printing of plain beams using various polymer based composite materials. (Ivanov Evgeni et al. 2019) 3D printed graphene/MWCNT/PLA composite characterized its mechanical and thermal properties. Results showed that 3D-printed composite samples outperformed the 3D-printed pure PLA. (Vu Minh Canh et al. 2021) 3D printed copper particle reinforced poly methyl methacrylate (PMMA). Though there are numerous works done on FDM-based 3D printing, developing functionally graded samples with material gradation along thickness direction is not yet explored. This might be due to challenges in getting proper interface bonding the layers occurred due to non-uniform volumetric shrinkage, adhesion, solidification. So with the aim of filling this research gap, the current work focussed on 3D printing of functionally graded foam and their respective sandwiches.

As the input material for the FFF process is supplied in filament form, three major things must be considered. The Primary is the extrusion of uniform diameter filament with respect to the nozzle diameter. Secondary maintaining required ductility to avoid filament breakage while spooling, feeding into the nozzle. Tertiary is maintaining the proper strength and modulus to sustain the force subjected by rollers while feeding.

Considering all these parameters, researchers have explored many materials; rather, filament development of syntactic foam is not completely done.

The current work explains the extrusion of three-phase syntactic foam and 3D printing of functionally graded foams for light weight structural applications. Subsequently, physical, mechanical, and thermal characteristic of the 3-phase foams was studied.

1.7 Literature Survey

Table 1.2. Previous work inputs on 3D printing and functionally graded materials.

Author	Process	Parameters	Materials Used	Property Studied	Remarks
(Tay Yi Wei Daniel et al. 2022)	3D Printing	Effect of gradation	Fibre reinforced Concrete.	Compression	<ul style="list-style-type: none"> • Strength to weight ratio increased upto 50% in graded concrete structures compared to plain structures. • Structure developed after topological optimization study will perform better than structure developed without topological optimization.
(Montgomery S. Macrae et al. 2021)	VAT Polymerization technique	Impact behaviour	Polymer	Drop Test	<ul style="list-style-type: none"> • FGM samples are 3D printed by varying the modulus property along thickness direction. • The effective energy absorption capacity of foams as well as rotational or shear damage mitigation both will be improved by tailoring the properties along thickness direction.

(Haldar AK et al. 2021)	3D Printing	Trapezoidal and triangular core designs.	Carbon fiber reinforced PLA	Compression	<ul style="list-style-type: none"> • The energy-absorbing capacity and compressive strength of sandwich panels both rise sharply with increase in thickness of core. • By increasing the area of contact between skin and core mechanical qualities enhanced
(Kanakannavar Sateeshkumar and Jeyaraj. 2021)	Hand layup	Thermal buckling behaviour	PLA/Natural Fibre	Thermal Buckling load	<ul style="list-style-type: none"> • When natural fiber reinforced PLA beams was subjected to thermal load, it exhibited snap through buckling phenomenon.
(Gao Fan and Yuanzhi. 2020)	3D printing	3D printing of FGM	Sic, SiO ₂ , Polydimethylsiloxane (PDMS).	Tensile testing	<ul style="list-style-type: none"> • FGM help in offering high flexibility at one end and good stiffens and thermal conductivity at other end.
(Mrityunjay. 2020)	3D Printing	Crystallinity	HDPE, Flyash	XRD, DMA	<ul style="list-style-type: none"> • 3D printed sample exhibited higher crystalline phase compare to their respective filaments. • Storage modulus of the sample exhibited direct relation with filler %.

(Dontsov Yury V et al. 2020)	3D Printing (FDM)	Twin screw speed, Extrusion temperature, Amount of Extrusion material	Ultra high molecular weight polyethylene	Taguchi optimization method,	<ul style="list-style-type: none"> • Extruder speed have more effect on yield strength. • Extruder temperature have more effect on fracture point • Extrusion multiplier have more effect on Tensile strength
(Anthony Xavior M et al. 2020)	Hand layup	Density	ABS	Tensile testing, Density	<ul style="list-style-type: none"> • FGMs are developed by varying density along the width direction. • Tensile properties of FGM are degraded but weight saving potential was increased.
(Waddar Sunil et al. 2020)	Hand layup	Thermal buckling behaviour	Epoxy/Flyash	Thermal Buckling Load, Density	<ul style="list-style-type: none"> • Increase in filler percentage helps in decreasing the density of the composite. • Thermal buckling load will increase with increase in filler percentage.
(Labans E et al. 2019)	Laminated composite	Variable angle tow composite	Carbon Fiber Reinforced Plastic (CFRP)	Mechanical Buckling and Free vibration	<ul style="list-style-type: none"> • Application of vibration correlation technique to experimental data helps

					in predicting perfect buckling load results.
(Amirpour Maedeh et al. 2019)	3DP	Material stiffness ratio	VeroWhite, RGD8530-DM, RGD8515-DM, FLX9895-DM.	3-Point bending, Digital image correlation.	<ul style="list-style-type: none"> • For nonlinear FG plates, the difference between experimental and FEA out of plane deflection greater than for linear FG plates. This difference could be explained by the high gradient distribution of the material additions. • Difference in out plane deflection value obtained through FEM and experimental analysis is higher in Nonlinear FG plate compared to linear FG plates.
(Geng Peng et al. 2019)	Extrusion, FDM	Temperature and printing speed	Polyether-ether-ketone (PEEK)	Influence of printing speed and extrusion temperature.	<ul style="list-style-type: none"> • Surface defects can be controlled by increasing the melt pressure. • The stability of the extrusion process is effected by a variable extrusion force.

(Waddar Sunil et al. 2018)	Hand layup method	Thermal and mechanical buckling load	Epoxy/Flyash	Thermal and mechanical Buckling load	<ul style="list-style-type: none"> When flyash reinforced syntactic foam beam is subjected to mechanical load it exhibited dimensional buckling load where when it subjected to thermal load it exhibited non dimensional buckling load i.e, it exhibited snap through buckling phenomenon.
(Waddar Sunil et al. 2018)	Hand layup	Filler percentage	Epoxy and Cenosphere	Mechanical Buckling and Free vibration	<ul style="list-style-type: none"> Increase in axial compressive load decreases the natural frequency. If load increased beyond the buckling load natural frequency started increasing.
(Caminero MA et al. 2018)	FDM (3D Printing)	Effect of continuous fiber	PLA, ABS, NYLON	Short beam shear stress test	<ul style="list-style-type: none"> Continuous fibre reinforced composite exhibits higher mechanical properties compared to plain samples. Inter laminar Shear strength decreased with increase in fibre percentage.
(Wang Rong et al. 2018)	FDM	Viscoelastic material as core	Hybrid composite based Sandwich	Vibration	<ul style="list-style-type: none"> According to the results of the dynamic study, the VMF technique is

			panels,		<p>effective in lowering amplitude without significantly increasing natural frequency.</p> <ul style="list-style-type: none"> • In a fixed modal test, the acceleration amplitude of the VMF Kagome lattice plate natural frequency was reduced by 18.19 dB in comparison to a solid plate and it was decreased by 6.03 dB when compared with standard Kagome lattice plate.
(Byberg Kate Iren et al. 2018)	FDM	Layer Orientation (90°, 0°, 45°)	ULTEM 9085	Tensile, Flexural and Compression	<ul style="list-style-type: none"> • It is reported that a flat build direction and 90° layer orientation result in the highest compressive stress. • The largest flexural stress was produced with flat built direction and a 0° layer orientation was combined.
(Reza. 2018)	FEM	Buckling phenomenon under thermal	Silicon-nitride, stainless steel	Timoshenko Beams theory	<ul style="list-style-type: none"> • Modulus of elasticity , thermal conductivity and CTE have significant effect on buckling

		and mechanical load			temperature. <ul style="list-style-type: none"> The critical buckling temperature drops permanently as the power law index rises.
(Waddar Sunil et al. 2018)	Hand layup method	Thermal and mechanical buckling load	Epoxy/Flyash	Thermal and mechanical Buckling load	<ul style="list-style-type: none"> When flyash reinforced syntactic foam beam is subjected to mechanical load it exhibited dimensional buckling load where when it subjected to thermal load it exhibited non dimensional buckling load i.e, it exhibited snap through buckling phenomenon.
(Tao Yubo et al. 2017)	3D Printing	Effect of Wood flour	Wood Flour/PLA	Mechanical characterization, Melting point	<ul style="list-style-type: none"> By adding wood flour to PLA, deformation resistance increases. No much variation in the melting point.
(Porter Daniel A et al. 2017)	FFF	nozzle temperature , Raster angle,	Polyvinylidene fluoride	Tensile Strength, FTIR	<ul style="list-style-type: none"> The Young's modulus is greatest at 0° (484 MPa) and lowest at 90° (419 MPa), raster angle respectively.

		outline perimeter shell,.			Maintaining the infill pattern parallel to the loading direction enhances the yield strength and it diminishes as the infill angle increases.
(Rajesh M and Jeyaraj. 2017)	Compression moulding	Woven fabric orientation	Jute	Buckling and free vibration	<ul style="list-style-type: none"> • Critical buckling load increases with increase in number of fabric layers. • Woven pattern have a significant influence on property of the composite.
(Domingo-Espin Miquel et al. 2015)	FDM	Build Orientation	Polycarbonate		<ul style="list-style-type: none"> • The X and Y orientations have the highest (1.43) and lowest (1.33) flexural stiffness coefficients, respectively. • Samples printed in the Z +45 orientation (36.0 MPa) exhibited the lowest tensile strength, whereas those printed in the X (45.9 MPa) and Z (45.6 MPa) orientations had equal tensile strengths. The samples with

					the highest tensile strength were printed in the Y (54.6 MPa) direction.
(<i>Doddamani Mrityunjay et al. 2015</i>)	Casting and Curing	Filler Percentage	High Density Polyethylene(HDPE) + fly ash cenosphere	Compression test and Flexural Test	<ul style="list-style-type: none"> • FGSF exhibited better weight reduction potential and energy absorption
(Wu Helong et al. 2015)	Timoshenko beam theory	Effect of gradation	Carbon nanotube	Free Vibration and elastic buckling	<ul style="list-style-type: none"> • CNT volume fraction and slenderness ratio exhibited significant influence on natural frequency and buckling load. • Core to skin thickness ratio have comparatively less effect on natural frequency. • Natural frequency of sandwich beam exhibited inverse relation with compressive load and direct relation with respect to tensile load.
(Nikzad Mostafa et al. 2011)	FDM (3000)	Composition, percentage of filler	ABS (P400), Iron Filler and Copper filler	Tensile, DMA, Heat capacity and	<ul style="list-style-type: none"> • Conductivity of ABS polymer increased with addition of copper as reinforcement.

				Thermal conductivity.	<ul style="list-style-type: none"> • An iron particle decreases the heat capacity of ABS composites. Fe-ABS composite with a 30 vol.% Fe (45m) content saw a significant increase in conductivity. • After 10 vol.% Cu, the storage modulus of ABS composite significantly decreased . • Iron-ABS (10 vol.% Fe) composites' tensile strength decreased considerably in comparison to plain ABS.
<i>(Anandrao Khalane Sanjay et al. 2012)</i>	Finite Element method	Volume fraction of metal and ceramics	Ceramics and metal	Free Vibration	<ul style="list-style-type: none"> • Natural frequency and mode shape of FGM beams with low aspect ratio are significantly influenced by transverse shear forces.
<i>(Caeti Ryan et al. 2009)</i>	Co-Curing method	Failure mechanism of FGMs	Epoxy/GMB	Compression	<ul style="list-style-type: none"> • Graded foams failed in sacrificial mechanism.

(Aydogdu Metin and Vedat. 2007)	higher order shear deformation theories, (HSDT), classical beam theories (CBT)				<ul style="list-style-type: none"> • Classical beam theory gave higher frequencies. • With increasing in mode number the deviation in the evaluated frequency values using CBT and HSDT also increases.
(Nikhil. 2007)	Casting	Effect of gradation, Particle size, Wall thickness	Syntactic foam	Compression	<ul style="list-style-type: none"> • Energy absorption capacity enhanced with material gradation. • Control over density, strength and modulus can be acquired by adopting graded beams

The literature shows that much work has been done on the numerical and analytical methods to characterize FGMs. But significantly less work is done to study the behavior of FGMs using experimental techniques. This is due to the minimum manufacturing methods to develop FGMs. As per previous works, FGMs are developed using casting, co-curing, and powder metallurgy techniques. Most polymer-based FGMs are developed using thermosetting based epoxy resins that cannot be recycled. But recyclable thermoplastic based FGMs are yet to be explored. Moreover, from the literature, it is also observed that cutting-edge technologies like fused filament fabrication (FFF) are yet to be explored for developing syntactic foam FGMs. Hence, current research focuses on developing thermoplastic foam based functionally graded foams (FGFs) and their sandwich using FFF based 3D printing process.

1.8 Motivation

Glass micro balloon (GMB) is one of the novel inorganic materials widely used as filler in a matrix to reduce the weight of a composite system. It is a free flowing powder that consists of thin walled spherical glass particles of outer diameter 10-200 μ m. Low density, high compression strength, low moisture absorption, and good acoustic insulating capability are unique properties of glass micro balloons. Glass micro balloons are used as inorganic reinforcement in developing polymer composites. Researchers showed that polymer based glass micro balloon reinforced syntactic foam exhibits multifunctional properties such as high specific compressive strength, low density, (Gupta Nikhil and Ruslan. 2006, Kim Ho Sung and Azhar. 2001), low moisture absorption (Calahorra A et al. 1987, Wouterson Erwin M et al. 2005). All these properties made syntactic foams suitable for the structural application of aerospace, marine structures, automobile body parts, etc. FGMs have certain advantages, like eliminating the sharp transition of property and increasing the energy absorption rate. These advantages help in enhancing the part quality. So introducing different manufacturing methods to develop FGMs and studying their behavior with respect to manufacturing methods is essential. Considering the unique properties of GMB and advantages of FGMs, made present research work to focus on developing

thermoplastic based functionally graded foams (FGFs) and sandwiches of functionally graded foams using FFF based 3D printing process.

The reasons I chose to research this subject are outlined below:

- Developing lightweight thermoplastic feedstock materials.
- Offering wide material choices for available commercial 3D printers.
- Complex prototypes and functional parts can be developed without limitation to the designer.
- Introducing a new method to develop FGMs with zero tooling cost.
- Eliminating the sharp transition of property

1.9 Objectives

Research activities on 3D printing of polymers and metals are mostly observed in the literature survey, but the 3D printing of functionally graded foams using FFF process is not mentioned. Though these foams offer many advantages like lightweight and better damping, processing methods are limited to compression molding, casting, and injection molding due to processing difficulties with proper filler sustainability. Overcoming these challenges in processing these foams is quite interesting and fancy. The development of a 3D printed syntactic foam composite using FFF is proposed in the present study. This study aims to synthesize 3D printed functionally graded syntactic foam by developing syntactic foam feedstock filament and to predict its micro structural, physical, mechanical, and thermal characteristics. The objectives of the proposed study are:

1. Develop lightweight feedstock filament of GMB/HDPE suitable for feeding in commercially available FFF based 3D printers.
2. Optimize 3D printing parameters for printing neat HDPE, plain foams, FGFs, and their sandwiches.
3. Study the influence of filler volume fraction on composite and investigation of physical (Density and Void content) and mechanical properties of FGF core (Three-point bending, Compression, Damping investigation, Thermal buckling) and their sandwich composite (Three point bending, Compression and Damping).
4. Perform microstructural characterization on 3D printed pre and post tested samples for structure-property correlations and demonstrate the representative

industrial scale components for showing the feasibility of 3DP of FGF sandwiches.

Thermoplastic foams applied in lightweight structures are mostly processed through compression and injection molding techniques. These foams are processed less through 3D printing technique. This might be due to the challenge of extruding the syntactic foam filament with suitable stiffness and diameter without any failure of hollow particle breakage. So the scope of the current work focused on the extrusion of syntactic foam filament of 20, 40, and 60 volume % of hollow GMB. And this work continued with optimizing the 3D printing parameters of these filaments using pilot studies. Using these optimized parameters, plain, functionally graded, and their respective sandwich samples are 3D printed. Further response of these various types' of 3D printed samples under different loading conditions was studied.

1.10 Outlines of Thesis

The current thesis presents a systematic study of the selected objectives. A brief skeletal structure of the thesis is presented below,

Chapter 1. Presented a brief literature survey on the FGM beams and FFF 3D printing process and further continued with motivation, objectives, and scope of the work.

Chapter 2. Discussion on the material used in the current work and various test methods followed for characterization.

Chapter 3. Discussion on the 3D printing parameters and strategies are discussed in this chapter.

Chapter 4. Compression behavior of the 3D printed FGF and FGSEs is mentioned.

Chapter 5. Flexural behavior of concurrently 3D printed FGF and FGSEs are reported.

Chapter 6. Mechanical buckling and free vibration details of FGF and FGSEs are explained.

Chapter 7. Thermal buckling response of 3D printed beams under non-uniform heating conditions is explored.

Chapter 8. Summary and conclusion of the entire work was mentioned.

Finally, the key findings of the significant inferences from the current research work are provided.

2. MATERIALS AND METHODS

2.1 Constituent Materials

In the current work for developing composite, thermoplastic based high density polyethylene (HDPE) is chosen as the matrix material, and hollow glass micro balloon (GMB) is selected as filler. Individual properties of the HDPE and GMB are mentioned in further sections.

2.1.1 Matrix

Matrix material HDPE of HD50MA180 grade was imported in ~3 mm granule form Figure 2.1a from Indian Oil Corporation Limited, Mumbai, India. The received properties of this HDPE material are mentioned in Table 2.1.

Table 2.1. Represents as received properties of HDPE HD50MA180 grade.

Property	Test Method	Typical Value	Unit
Melt Flow Index (190 ⁰ C/2.16 kg)	ASTM D 1238	20.0	gm/10 min
Density @ 23°C	ASTM D 1505	950	kg/m ³
Tensile Strength at Yield	ASTM D 638	22	MPa
Elongation at Yield	ASTM D 638	12	%
Flexural Modulus	ASTM D 790	750	MPa
Hardness	ASTM D 2240	55	Shore D
Vicat Softening Point	ASTM D 1525	124	°C

2.1.2 Filler

Hollow glass micro balloons of iM30K grade imported from 3M Corporation, Singapore, are used as reinforcement. As received properties of this untreated GMB, Figure 2.1b are mentioned in Table 2.2.

Table 2.2. Represents properties of hollow GMB (iM30K grade)*.

Particulars	Typical Value	Unit	Test Method
True Density	600	(kg/m ³)	3M QCM 14.24.1
Isostatic Crush Strength	27,000	(psi)	3M QCM 14.1.8
Packing Factor (bulk density to true particle density)	63	%	-----
Oil Absorption	33.5	g oil/100 cc	ASTM D282 - 84
Softening Point	600	°C	-----
Flotation (density < 1.0 g/cc)	90	% (in volume)	3M QCM 37.2
Volatile Content (by weight)	Max. 0.5	%	3M QCM 1.5.7
Alkalinity	< 0.5	Milliequivalents/gram	3M QCM
pH (5% loading in water)	9.5	-----	ASTM D3100 - 1982
Diameter (average)	18	microns	3M QCM 193.0
Softening temperature	600	°C	-----
Thermal conductivity	0.05 - 0.20	Wm ⁻¹ K ⁻¹	@20°C
Dielectric constant	1.2 - 1.9	-----	@100 MHz
Minimum fractional survival	90	%	-----

*As per supplier



Figure 2.1. Representative picture of as received (a) HDPE and (b) Hollow GMB.

2.2 Composite Preparation

HDPE and GMB composite is prepared using Brabender of 16CME SPL imported from western company Keltron CMEI, Germany. During this process blending parameters like blending temperature and speed are selected through pilot studies and finalized at 160°C and 10 rpm, respectively (Jayavardhan ML et al. 2017, Jayavardhan ML and Mrityunjay. 2018). These parameters are selected such that it avoids GMB fracture. A pictorial representation of the developed composite blend is shown in Figure 2.2a. Initially, HDPE and GMB are placed in the confined chamber of the blending machine, and this mixer gets melted in the heating unit. This mixer is supplied through a twin screw shown in Figure 2.2b. A pictorial representation of extracted blend is shown in Figure 2.2c.

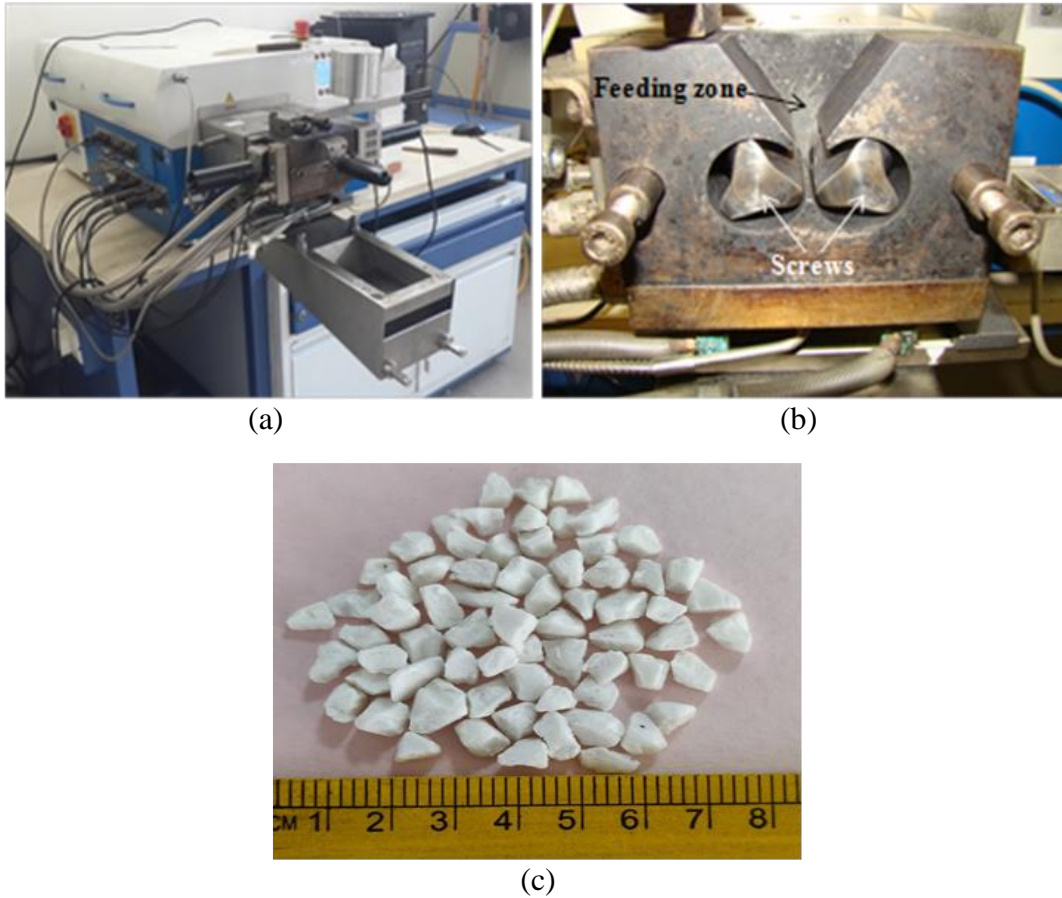


Figure 2.2. (a) Brabender, (b) Mechanism of blending and (c) Composite.

The blend compositions are denoted by the letters H20, H40, and H60, where H stands for the HDPE matrix and 20, 40, and 60, respectively, reflect the volume percent of GMB that is contained in the HDPE matrix. Since no observable change in mechanical properties is observed below 20%, the GMB volume% is chosen to be in the range of 20 to 60. Particle-particle interactions cause much more viscous blend development at 60% volume fraction, which results in significantly increased particle breakage. A flowchart of the anticipated work for this project is shown in Figure 2.3.

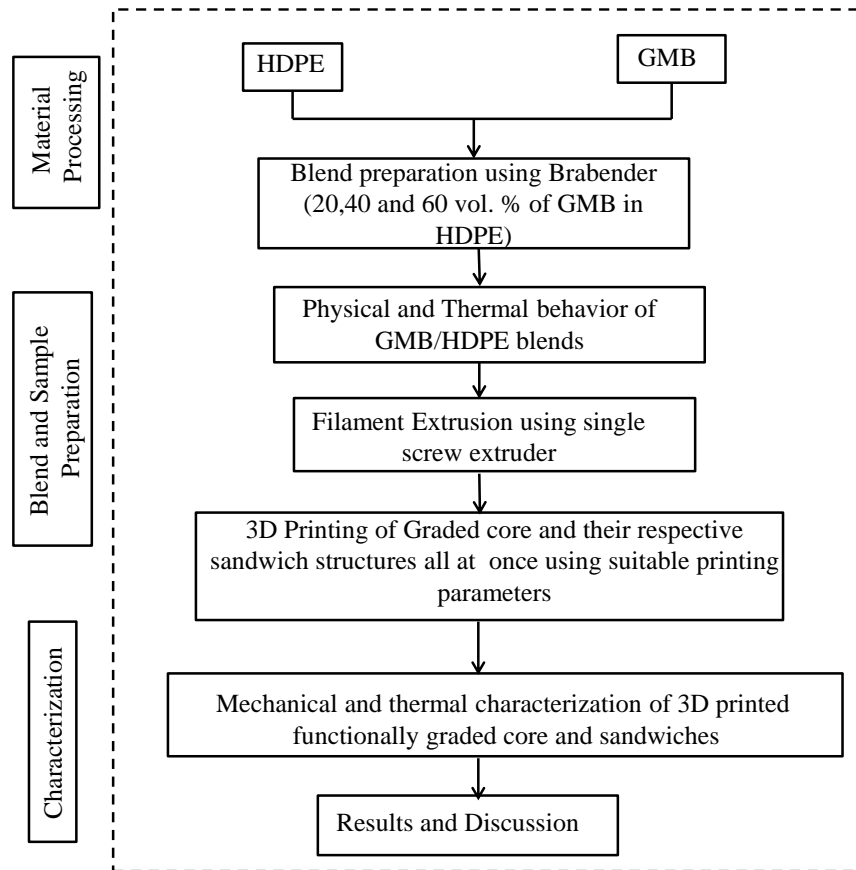


Figure 2.3. Representative image of work flow.

2.3 Melt flow Index (MFI)

The flow rate of the material through a small aperture under a certain temperature and load is known as the melt flow index. In the current work, as per ASTM D1238 MFI, all composites are measured using Dynisco LMI5000. As per the MFI of the material, the extrusion multiplier value is selected during 3D printing. The MFI equipment used in the current work is represented in Figure 2.4.



Figure 2.4. MFI measuring equipment.

2.4 Filament Extrusion and 3D Printing

Extrusion is one of the preferable methods for manufacturing filaments, films, tubes, etc. It is a continuous process. It contains a material feeding zone, heating zone, die, water bath, and take-off roller unit. In this process, the material is initially placed in the hopper, which is connected to the barrel containing a single screw. This barrel is also connected to electric heaters and thermocouples. When the material is placed in a hopper, a single screw guides the material inside the heating zone, where the temperatures are adjusted according to the melting point of the material, and thermocouples measure the current temperature of the barrel. Once the material reaches the heating zone, it gets melted, and due to the motion of a single screw, this melted material is pushed out from the die hole. This material comes out of die stretched by the taking-off unit pulling the filament by passing it through a water bath where the extruded filament gets solidified. The required constant diameter of the extruded filament is maintained by adjusting the extruder screw speed and take-off speed. Three major things should be considered while extruding the syntactic foam filament. Primary is avoiding extra shear forces to prevent filler failure, secondary is control over the void formation, and tertiary is filler agglomeration and non-uniform diameter. For better clarity over the process, both the schematic and extrusion setup are shown in Figure 2.5 and Figure 2.6. Table 2.3 represents the specifications of a single screw extruder used for filament extrusion. In the current work manufacturing method selected for the fabrication of the sample is 3D printing based Fused Filament Fabrication (FFF). For better clarity over the process, both schematic and live 3D printer pictures was shown in Figure 2.7 and Figure 2.8. This FFF based 3D Printer is imported from AHA. It contains two brass nozzles, and these two nozzles are connected to the heating block and gear and encoder unit. This gear and encoder unit controls the rate of extrusion of the material from the nozzles. When there is a need to print critical structures, one nozzle will build the main part, and the second nozzle will print support. The chamber has a fixed glass bed with embedded heating elements. The loading spools of part and support material are made easier using hangers. The machine control unit keeps track of the printing head's movement in the X, Y, and Z directions using independent stepper motors. Technical specifications of the FFF 3D printer used in the current work are mentioned in Table 2.4.

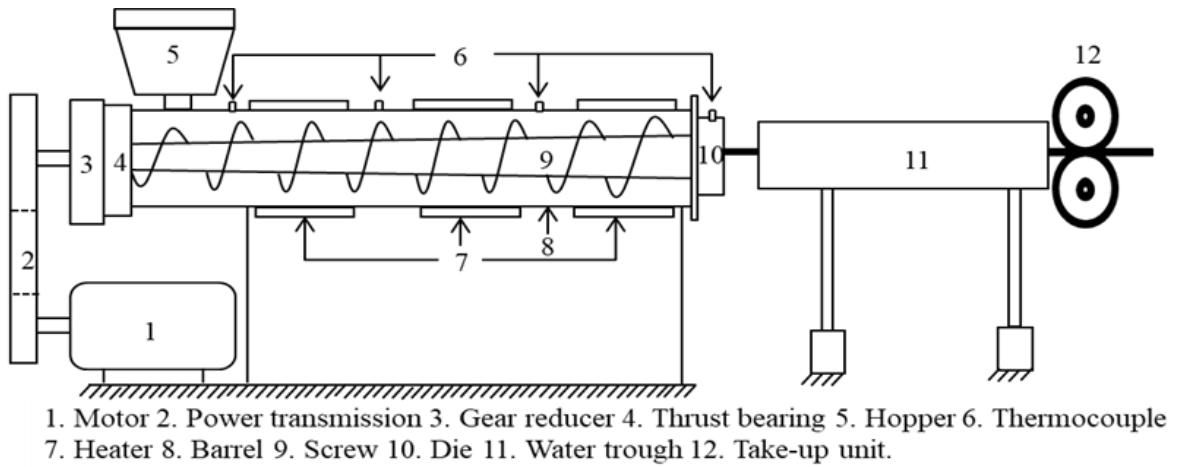


Figure 2.5. Schematic diagram of single screw extruder.



Figure 2.6. Experimental setup of extruder.

Table 2.3. Specifications of single screw extruder.

Specification	Details
Cooling	Water cooling
Die sizes	1.75, 2.5 and 3 mm.
Drive	3 HP ACVF Drive, Max. RPM 60.
Heaters	Ceramic in SS cover, 4 nos. with load up to 5 Kw.
Heating control panel	PID controllers with 5 zones, Accuracy $\pm 1^{\circ}\text{C}$, Max. Temp. 450°C .
Hopper	Min. 3 Kg, SS sheet with discharge chute.
Make and Model	Aasabi Machinery (P) Ltd. Dombivli, Mumbai, India. (25SS/MF/26, L/D ratio of 25:1)
Pelletizer	Helical type, minimum 4" dia. \times 4" L with 0.5HP ACVF drive.
Screw	High tensile nitride hardened alloy steel to sustainable up to 450°C , Dia. 25 mm with length 26D having uniform discharge.
Spooling arrangement	Take up rollers with 0.5 HP ACVF drive with height adjustments and castor wheels

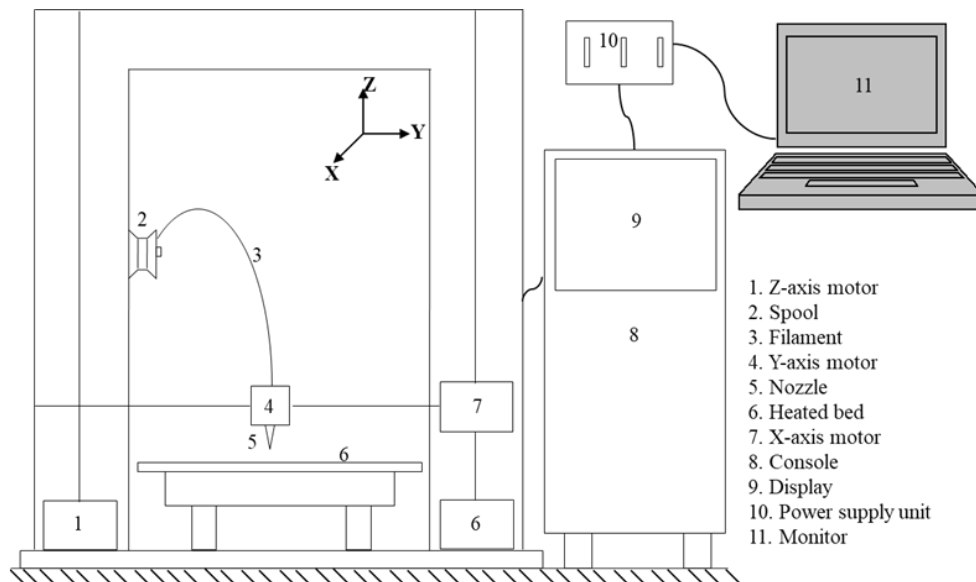


Figure 2.7. Block diagram of FFF 3D printer.

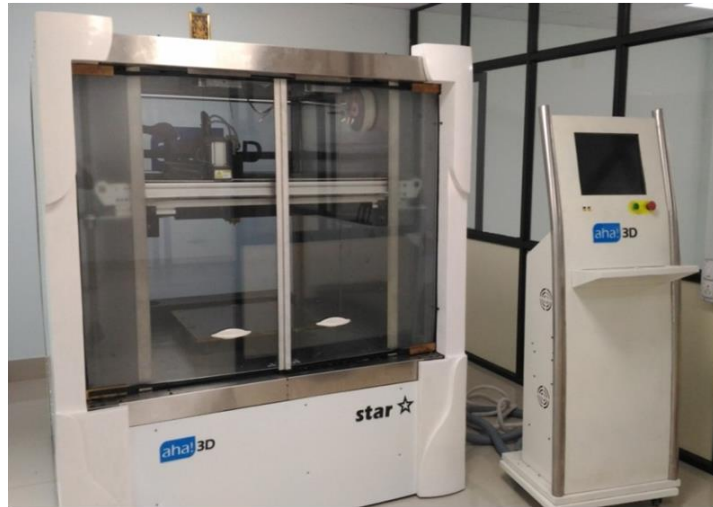


Figure 2.8. Representative picture of FFF based Aha 3D printer.

Table 2.4. Specifications of FFF based aha 3D printer.

Specification	Details
Build chamber	Up to 100°C
Build platform	Up to 150°C
Build volume	500 × 500 × 500 mm ³
Data import format	STL, AMF, OBJ
Filament diameter	3 mm (Standard)
Layer height	100 to 500 microns
Make and model	Aha 3D Innovations Pvt. Ltd., Jaipur, Model: Star
Max. extrusion temp.	Basic tool head: 300 °C, Standard tool head: 500 °C
Number of extruders	2
Positional accuracy	50 micron (stepper), 20 microns (servo), 4 microns (dual servo)
Power requirement	220V AC, three phases
Printing materials	All engineering thermoplastic and Plastic Composites, ABS, HIPS, PC, Nylon, TPU, TPE, Carbon fiber composite, etc.
Rate of production	Basic tool head: up to 15 cm ³ /hr., Standard tool head: Up to 150 cm ³ /hr.
Screw	High tensile nitride hardened alloy steel to sustainable up to 450°C. Suitable compression ratio (at least Dia. 25 mm with length 26D) having a uniform discharge at metering zone.
Technology	Fused Filament Fabrication (FFF)
Tool head cooling	liquid cooled.
Workstation compatibility	Windows XP, Windows 7, Linux

2.5 Micro CT

X-ray scanning is used in micro-CT (micro tomography) to generate a 3D model without harming the original object. Micro-CT scanning's unique properties enable researchers to examine a sample's shape and investigate features such as porosity and structure. In the current work, Micro CT instrument of phoenix v | tome | x s model manufactured by General Electric Measurement and Control Solutions is used to find the porosity distribution in 3D printed FGF and FGSFs’.

2.6 Surface roughness

In the current work, surface roughness and density of 3D printed Pure HDPE furrows and composite with the highest filler volume fraction are measured using Non-contact profilometer Analysis with a step size of 5 μ m. A representative image of non-contact profilometer is shown in Figure 2.9.

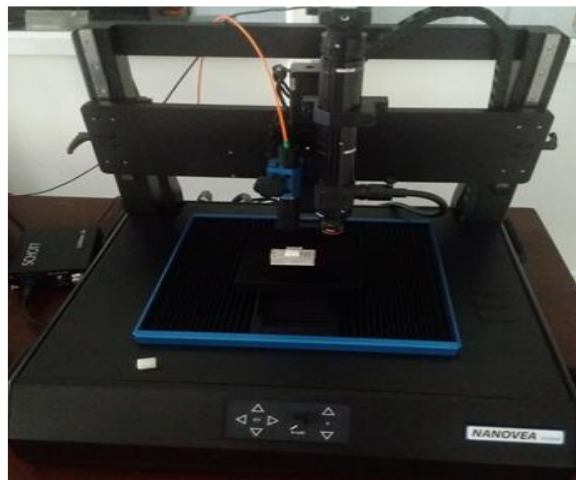


Figure 2.9. 3D Profilometer

2.7 Density

Density is one of the crucial physical properties of the material. This property has a direct relationship with the weight of the material. Experimental densities of 3D Printed plain, functionally graded, and their respective sandwiches are calculated as per ASTM D792-13. For comparing the accuracy of the experimental densities and void percentage, theoretical densities of the 3D printed samples are calculated using a rule of mixtures.

$$\rho_c = \vartheta_m \rho_m + \vartheta_f \rho_f \quad (2.1)$$

$$\rho_{th} = \varepsilon \left(\rho_c \times \left(\frac{\text{composite thickness}}{\text{FGSF thickness}} \right) \right) \quad (2.2)$$

$$\varnothing_v = \frac{\rho_{th} - \rho_{exp}}{\rho_{th}} \times 100 \quad (2.3)$$

Here ρ_c is density of composite, ϑ_m is volume fraction of matrix, ϑ_f is volume fraction of filler, ρ_f is density of filler, ρ_m is density of matrix, \varnothing_v is void percentage, ρ_{th} theoretical density, ρ_{exp} experimental density.

2.8 Flexural Testing

2.8.1 Experimental Analysis

As per ASTM-D790, 3D printed FGF and FGSFs with dimensions of 180×18×6 (in mm) and 180×18×8 (in mm) are tested for their flexural response at a strain rate of 0.01s⁻¹ with cross-head displacement velocity of 2.54 mm/min for FGFs and 3.41mm/min for FGSFs. Zwick-Roell Z020 universal testing machine (UTM) with 0.1 MPa pre-load is used for experimental investigation of flexural response. UTM used Equation 2.4 and Equation 2.5 to evaluate the modulus and strength of the beam during experimentation. Five samples of each composition are tested, and average values of the obtained results with standard deviation are mentioned in the current work.

$$E_f = \frac{L^3 m}{4 w t^3} \quad (2.4)$$

$$\sigma_{fs} = \frac{3 P L}{2 w t^2} \quad (2.5)$$

Where L is span length (mm), w is beam width (mm), t is beam thickness(mm), and m is the slope of the tangent line drawn to the initial linear portion of the load-deflection curve. The flexural stress (σ_{fs}) is calculated by m as the slope of the tangent line to the load-deflection curve's initial straight-line segment.

2.8.2 Finite Element Analysis

The graded foam finite element analysis is performed to analyze the stress distribution and deflection occurrence in FGF and FGSFs along their length and thickness

direction under transverse loading conditions. FEA analysis is done using a commercially available Ansys package. In this FGF and FGSFs, beams are modeled in layer-wise fashion with 96 and 128 mm span lengths, respectively, and subsequently activated ADD FROZEN command for restricting the relative motion between the layers. These beams are meshed using SOLID 186 elements leading to 19238 nodes, 2418 elements, and 21844 nodes, 2854 elements respectively for FGF have and FGSF Figure 2.10a and Figure 2.10b. Boundary conditions applied while performing numerical analysis are shown in Figure 2.10c. Experimental material properties (Bharath H. S et al. 2021, Bharath HS et al. 2020) and loading values are considered while performing finite element analysis.

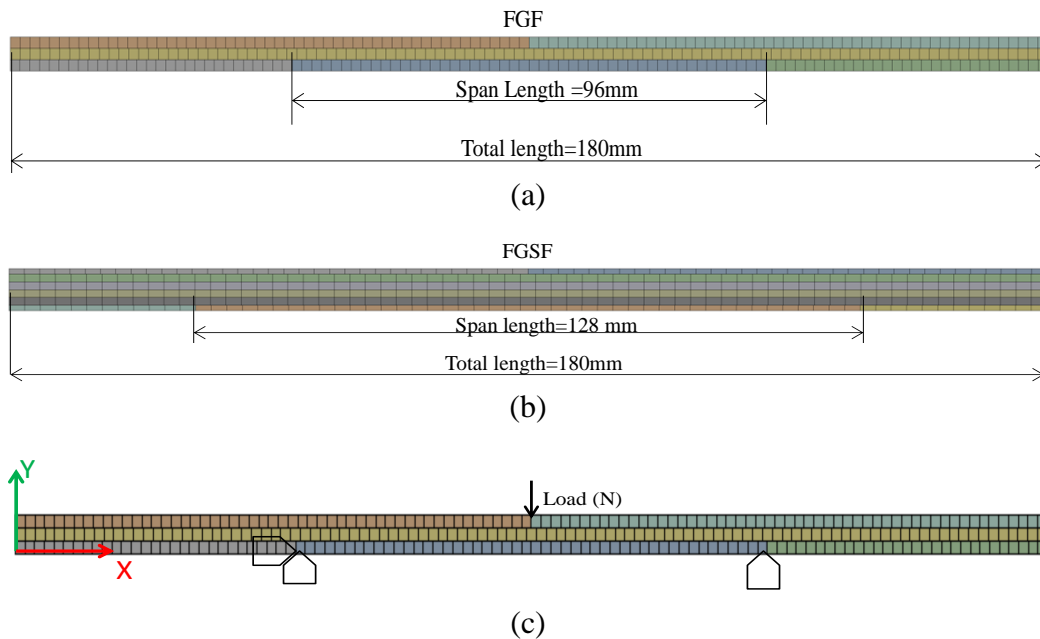


Figure 2.10. Representative image of (a) meshed FGF beam, (b) meshed FGSF beam and (c) boundary and loading conditions

2.9 Compression Testing

ASTM C365/C365M-16 is followed to investigate the compression response of plain and FGFs. According to ASTM standards, specimen cross-sectional area should be 625 mm² (maximum) for foams with sample dimensions 25×25×15 mm. Five composition samples are tested at a constant cross-head 0.5 mm/min displacement rate using Zwick-Roell Z020 USA (20 kN load cell). The data is analyzed using MATLAB code that was created in-house. The peak stress determines the

compressive strength at the end of the elastic zone. At least five samples of each volume fraction are analysed to assure accuracy.

2.10 Buckling and Free Vibration Behaviour

2.10.1 Buckling Load

Mechanical buckling of 3D printed GMB/HDPE based FGF and FGFSs under clamped-clamped condition is carried out using H75KS (Tinius Olsen make, UK) UTM of 50 kN load cell capacity. The experimental setup of the buckling test is presented in Figure 2.11.

The possibility of behavior change in post-buckled FGF and FGFS prints is carefully considered by keeping the end shortening 0.7 mm. Based on experimentally obtained load and deflection data from UTM, critical buckling load (P_{cr}) is evaluated graphically using DTM and MBC methods (M. 2007, Tuttle M et al. 1999). In the DTM approach, tangents are drawn at both pre and post-buckling curves wherein Y-Coordinate corresponding to the intersection point of tangents deduces P_{cr} Figure 2.12a. In MBC technique, bisector of the angle formed between the tangents drawn at pre and post-buckling regions is extrapolated to intersect the load and deflection graph Figure 2.12b. The Y-Coordinate of the intersection point yields P_{cr} . P_{cr} evaluated using these two graphical approaches are considered as the upper and lower boundary limits respectively for the critical load.

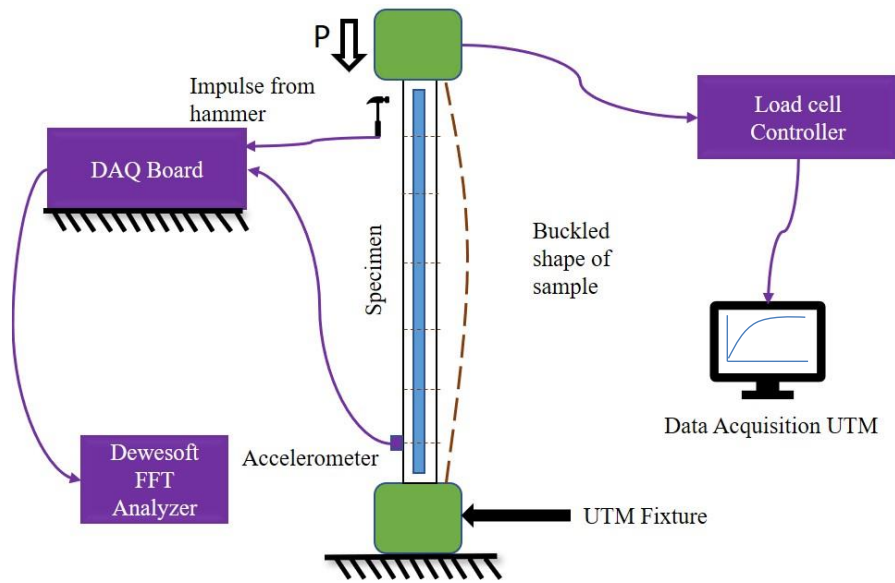


Figure 2.11. Schematic representation of experimental set up for estimating buckling load and free vibration

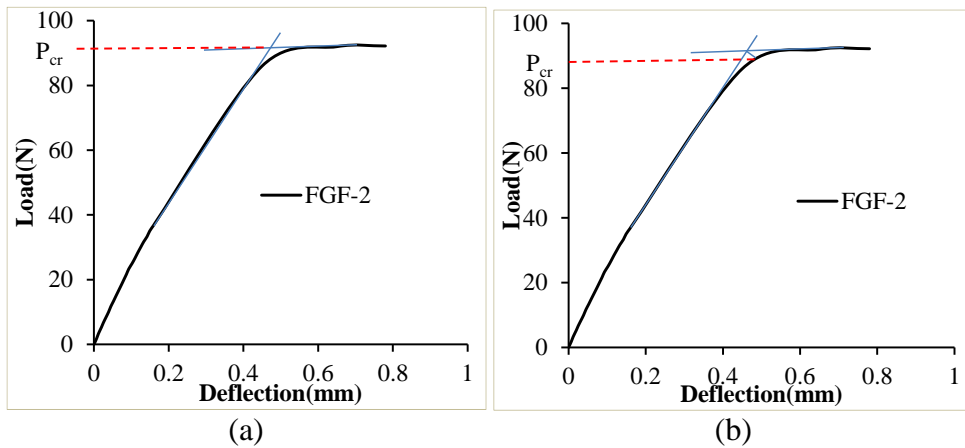


Figure 2.12. Representative load and deflection graph for evaluating P_{cr} using (a) DTM and (b) MBC method.

2.10.2 Free Vibration

The modal analysis (experimental) is performed to predict natural frequencies and damping factors corresponding to the first 3 bending modes of FGF and FGSFs under clamped-clamped conditions Figure 2.13. The experiment is performed from zero (no load) to critical load with 25 kN load increments. Meanwhile, the test is paused for 2 min after every 25 kN load increment to conduct the modal analysis. Machine parameters are adjusted so that the sample's applied load remains constant while performing modal analysis in pause mode. The free vibration test is performed using the impulse hammer method where the sample is excited using impact hammer (sensitivity of 10 mV/N, 9722A2000) of Kistler make that generate vibration signals

measured using uniaxial accelerometer (sensitivity of 10 mV/g, 8778A500) mounted on the sample using bee's wax. Eight channel-based DAQ, time-dependent applied load, and vibration results are fed as the input to DEWESoft. Using the Fast Fourier transformation technique, DEWESoft converts the time to frequency domain signals (Tian Chun Guang et al. 2013). This frequency data acquired for corresponding impulse excitation at the different marked positions in Figure 2.13 captures FRF. The software renders damping factor, frequency, and mode shape. FRF, mode circle, and mode shape utilized in the experimental modal analysis are shown in Figure 2.14. Based on the circle fit method, the modal damping factor is evaluated using Equation 2.6.

$$\epsilon = \frac{\omega_2^2 - \omega_1^2}{2\omega_0[\omega_2 \tan\frac{\alpha_2}{2} + \omega_1 \tan\frac{\alpha_1}{2}]} \quad (2.6)$$

Here ω is the angular frequency (rad/sec) and α is the angle formed between ω 's ($^\circ$).

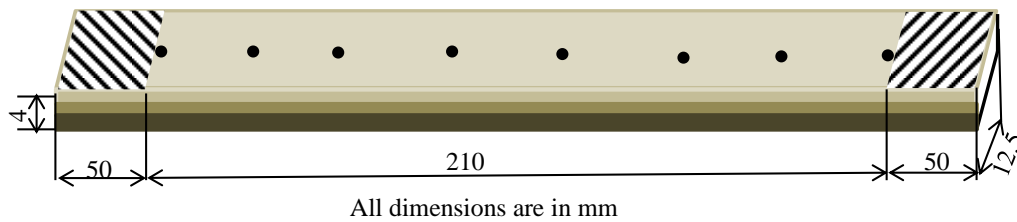


Figure 2.13 Representative image of sample tested for free vibration.

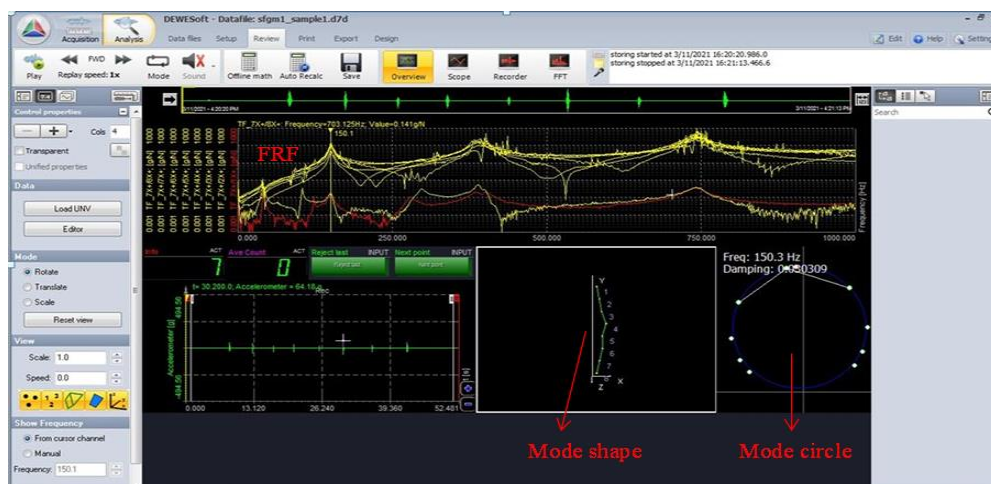


Figure 2.14. Details of modal analysis display in DEWESoft.

2.10.3 Vibration Correlation Technique

The vibration correlation approach, a non-destructive methodology, is used to estimate the P_{cr} from the pre-buckling stage for composite beams. There are two different vibration correlation technique (VCT) methods: the direct approach and the indirect one (Singer J. A et al. 2003). The direct technique is based on the extrapolation of an experimental functional connection between the natural frequency and applied compressive load, whereas the indirect method assesses the real boundary conditions permitting the estimation of P_{cr} . The buckling load of the 3D prints is extrapolated in this experiment using a direct approach.

2.10.4 Numerical Analysis

The non-linear static structural analysis with geometric non-linearity is performed using ANSYS to obtain the load-deflection plot which is compared with the experimental plot. In numerical analysis, the material properties of SFs are assumed to be quasi-isotropic. Theoretical material properties like young's modulus of H - H60 are evaluated using the Bradelle- Genna model (BGM) (Kumar K Senthil et al. 2014). The BGM considers radius ratio and volume fraction as input to estimate modulus values (Kumar K Senthil et al. 2014). Poisson's ratio of GMB and HDPE is considered as 0.25 and 0.425. Poisson's GMB/HDPE composite ratio is calculated using the mixture rule (Anandrao Khalane Sanjay et al. 2012, HS Bharath et al. 2020). Numerically estimated P_{cr} based on finite element method is compared with experimental results. FGFs dimensions of $210 \times 12.5 \times 4$ mm is modelled as a layered entity using commercial ANSYS space claim having isotropic domain for each composition across the thickness. FGFs and FGSFs are meshed using four noded SHELL 181 element Figure 2.15. Displacement boundary condition and compressive load is applied on the FGFs. Initially, linear Eigenvalue buckling analysis is performed to estimate the primary buckling mode shape. Further, the mode shape along with geometric imperfection factor (GIF) is given as input to perform non-linear static structural analysis for graphing the load-deflection behaviour. GIF is varied in the range of 0.0001 to 0.001.

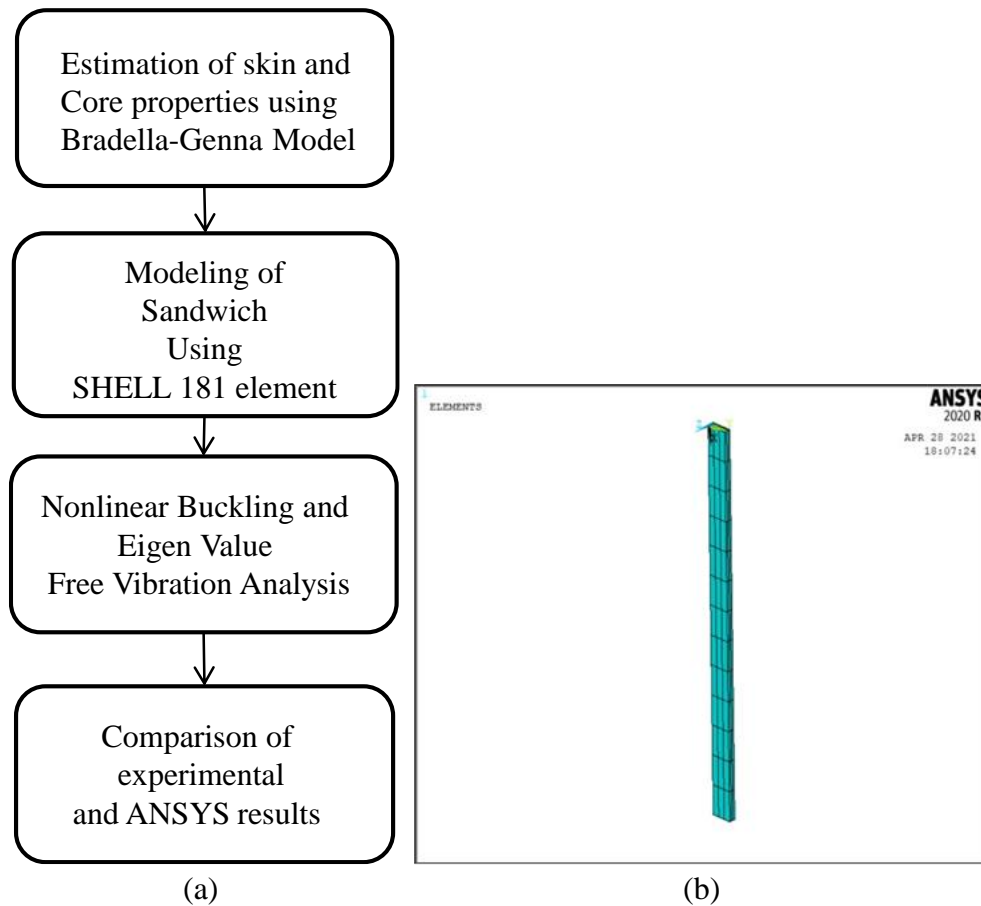


Figure 2.15. (a) Procedure of numerical analysis and (b) Meshed image of FGF.

2.11 Thermal Buckling

In the current work to predict the thermal buckling load and deflection patterns of plain, graded beams and their respective sandwiches, a thermal buckling setup was developed, as shown in Figure 2.16. In this experimental setup, the beam is subjected to clamped boundary conditions by fixing it in a steel frame and tightening it with Allen bolts, so that motion at the ends of the beam is restricted. Thermal load is applied using a 230 V/1000 W single-tube short-wave infrared (IR) heater. With the intention of subjecting the beam under non-uniform thermal loading conditions, the position of IR- heater is placed at the one end of the beam in case-1 (one-end-heating) Figure 2.17a, the center of the beam in case-2 (center-heating) Figure 2.17b and at both ends of the beam in case-3 (both-end-heating) Figure 2.17c. To measure the lateral deflection of the beams MVL7 model of linear variable differential transducer (LVDT) with ± 25.4 mm stroke length is used. This LVDT can operate at -50°C to 125°C temperature range. Thermal sensors are fixed to the sample to measure the

temperature at different positions as per the desired temperature profile study. Code was developed using Lab-view to employ the relay unit to control the on and off condition of the IR heater as per set point and current temperature reading. The temperature versus deflection data was taken as output using NI9481 DAQ.

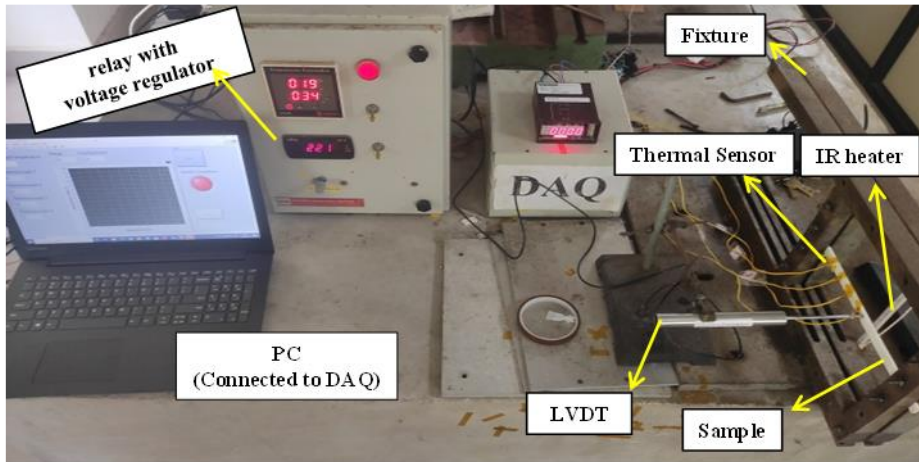


Figure 2.16. Experimental setup for thermal buckling experiment.

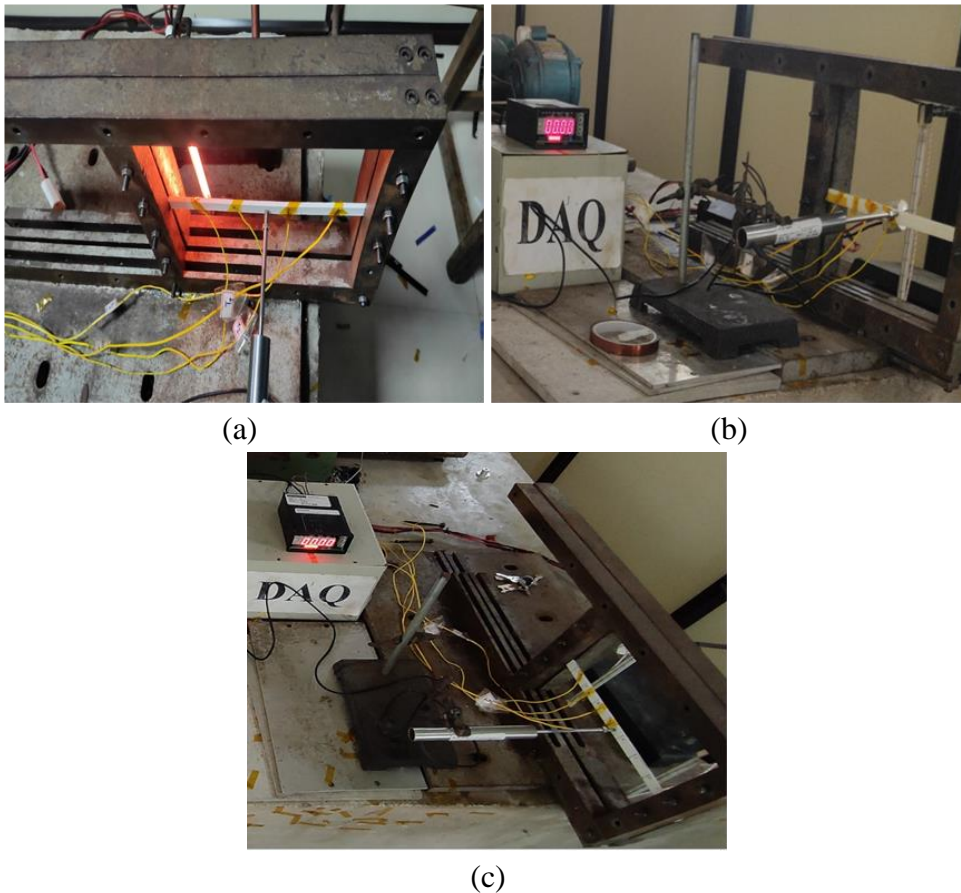


Figure 2.17. Heating condition (a) case-1, (b) case-2 and (c) case-3.

2.12 Microstructural Characterization

Using a scanning electron microscope (SEM) JSM 6380LA JEOL, Japan, an extensive micrograph is done on extruded filaments, as printed plain, graded foams and their respective sandwiches, and post-tested filaments and prints. As the current samples are polymer based, to make them conductive before performing SEM, all samples are subjected to gold sputter using JFC-1600 auto fine coater.

3. MATERIAL CHARACTERIZATION AND PROCESSING METHODS

3.1 Blend Characterization

The flow characteristics of the material are very important in 3D printing. This behavior is studied by performing the melt flow index (MFI).

3.1.1 MFI of HDPE and Composite foams

A melt flow index test is performed to check the amount of material flow through the aperture of a nozzle at a particular temperature and load. The flowability of the polymer decreases with an increase in the filler percentage. This is due to the filler restriction forces acting on the matrix material (Escócio Viviane Alves et al. 2015). Experimental results showed that neat HDPE granules exhibited their MFI value as 17.94 gm/10 min and MFI values of H20, H40, and H60 composite as 13.76, 8.11, and 4.85 gm/10 min. This decrease in the flow rate of composite material can be counterbalanced in the 3D printing process by increasing the extrusion multiplier and printing temperature.

3.2 Filament Development

In the current work, HDPE and foam filaments extrusion is performed using a single screw extruder with a 25:1 L/D ratio (flight length of screw to its outside diameter) of 25SS/MF/26 models, supplied by Aasabi Machinery Pvt. Ltd., Bombay, India. The initial process of filament extrusion was pre-heating of composite in an oven at 80°C for 24 hours. This preheating is done to evaporate any moisture content in the composite because the moisture in the composite may lead to the rough surface of the filament, and continuous filament extrusion is also disturbed. The uniform diameter and properties of filament-like modules, strength, and density depend on three major extrusion parameters: primary is a barrel and die temperature, secondary is screw speed, and tertiary is take-off speed. Maintaining proper barrel and die temperature is very important to melt the solid composite pellets and to perform the entire extrusion process without any blockage at the die portion. The material from the die hole was pulled by the take-off unit, passing filament through the water bath. The material in semi-solid state gets solidified while it passes through a water bath. The desired diameter of the filament was adjusted by varying the screw and take-off speed. In the

current work, HDPE and foam pellets are fed to an extruder with a temperature profile of 145-150-155-145°C from the feed to the die section, screw, and take-off unit speed of 25 and 11.5 rpm, respectively, to produce the filament of 2.85 ± 0.05 mm diameter. All these parameters have been chosen by considering HDPE melting temperature, uniform and homogeneous mixing of GMB in HDPE without breakage, rheological behavior of blends, and presence of porosity, if any, during extrusion (Bharath HS et al. 2020). Sometimes the filament can be in an oval cross-section. This can be avoided by adjusting the distance between two rollers in the take-off unit. Figure 3.1a represents the circular cross-section of extruded H60 filament. H20 filament at higher magnification show uniform dispersion of GMBs in the matrix without any particle breakage Figure 3.1b confirms the suitability of chosen extrusion parameters. The extruded H60 filament is photographed and presented in Figure 3.1c.

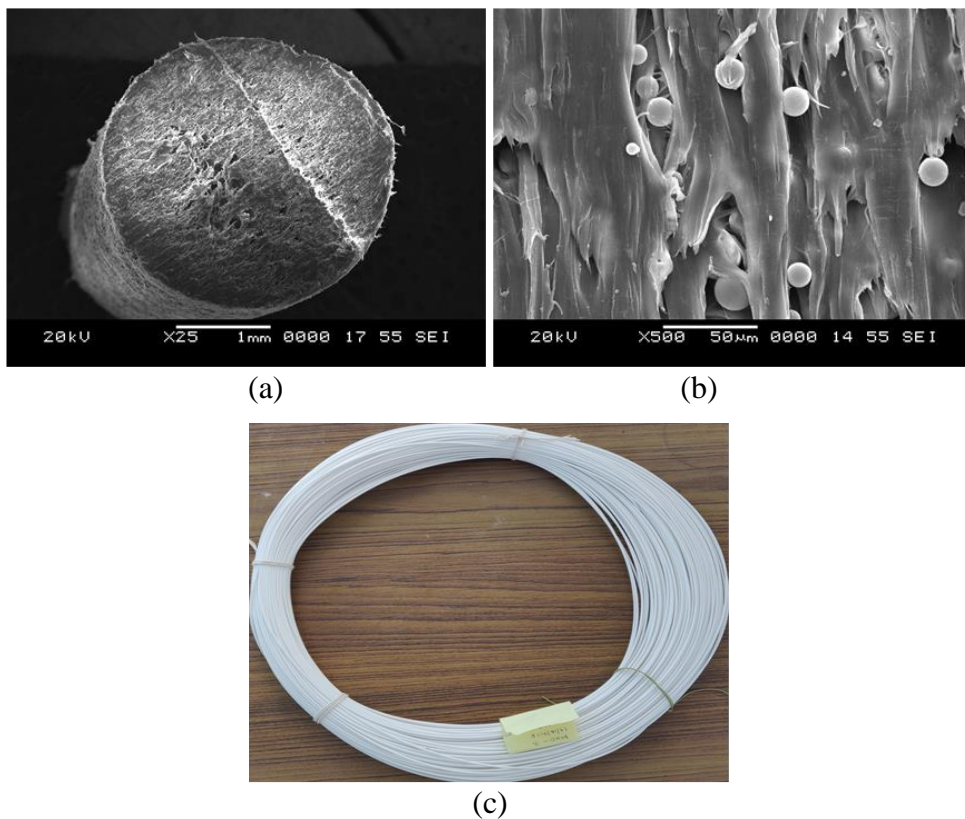


Figure 3.1 (a) SEM image of filament cross section (b) filler sustainability in filament and (c) extruded H60 filament

The developed filament should possess enough spooling stiffness and pass through the gear and encoder mechanism while 3D printing. Hence evaluating filament properties like density, tensile strength, and modulus is crucial. Initially, the density of all four types of composites, HDPE, H20, H40, and H60, are measured experimentally. Results showed the experimental density of HDPE, H20, H40, and H60 as 942 ± 8 , 858 ± 15 , 780 ± 11 and 683 ± 12 kg/m³. To measure the accuracy of experimental density, theoretical density was calculated, and results showed the theoretical density of HDPE, H20, H40, and H60 as 950, 880, 810, and 740 kg/m³. The deviation of this experimental density concerning theoretical density is due to the voids incorporated during extrusion. These voids help in enhancing the weight-saving potential. The void percentage of HDPE, H20, H40, and H60 are 0.84, 2.50, 3.70, and 7.70 %. The weight-saving potential of H20, H40, and H60 foams with respect to HDPE filament is 8.92, 17.20 and 27.49 %. Further tensile testing was performed to study the modulus and strength of the extruded filaments. Modulus of H, H20, H40, and H60 filaments are 722 ± 16.73 , 781 ± 17.95 , 826 ± 14.27 , and 1060 ± 18.53 MPa, whereas strength is evaluated as 16.4 ± 0.22 , 10.45 ± 0.42 , 9.25 ± 0.39 and 7.16 ± 0.17 MPa. The results show that modulus increases and strength decrease with an increase in filler.

3.3 3D Printing of Syntactic Foam Cored Sandwich composite

3.3.1 3D Printing

Pilot investigations are carried out to propose suitable printing parameters for printing core (H20-H60) and sandwiches (SH20-SH60) by exploiting N1 and N2 nozzles available on commercial FFF based printers. Cores and sandwiches of dimensions $180\times 18\times 6$ mm³ and $180\times 18\times 8$ mm³, respectively, are printed using the parameters listed in Table 3.1. GMBs presence in the HDPE matrix reduces the coefficient of thermal expansion leading to lower warpage and samples with dimensionally closer tolerance (Bharath HS et al. 2020). Several initial trials in the pilot investigations did not yield high-quality prints. The reasons for such observations and the possible solutions that resulted in sound quality core and sandwiches are discussed hereafter. The suitable parameters (in brackets) are also listed in Table 3.1 based on the following discussions.

Table 3.1. Optimized printing parameters of FFF.

Parameters	H	H20	H40	H60	SH20	SH40	SH60
N1 (°C) - HDPE filament	200-				200-	200-	200-
	230	-----	-----	-----	230	230	230
	*[225]				[225]	[225]	[225]
N2 (°C) - Foam filaments		200-	230-	230-	200-	230-	230-
	-----	230	250	250	230	250	250
		[225]	[245]	[245]	[225]	[245]	[245]
Extrusion Multiplier	1	1	1	1.2	1	1	1.2
Bed temperature (°C)	80-120 [120]						
Chamber temperature (°C)	45-75 [75]						
Printing speed (mm/s)	30-40 [35]						
Layer thickness (mm)	0.5						
Infill percentage (%)	100						
Raster pattern	Rectilinear						
Raster angle	±45°						

*All the values presented in the square brackets are suitable printing parameters.

3.3.2 Substrate selection

Selecting a suitable substrate for printing core and sandwich is crucial from the perspective of adhesion of the raft to the bed and post-print removal without damaging the print. The commercially available printers are fitted with a glass bed that necessitates exploring suitable substrates for layered deposition based on the polymer/polymer composite being considered in this study. The substrate serves two functions: a) Establish good bonding between the raft and the substrate itself so that the complete part gets built without any defects b) Permits easy removal post-printing without damaging the bottom-most layer of the print. Table 3.2 presents the evaluation of three substrates (HDPE tape, Kapton tape, and SEBS KratonTM) used in the present work. Initially, samples are printed on HDPE tape without bed heating. The samples showed good adhesion to the substrate but posed difficulty in print peeling from the tape, necessitating subsequent polishing operations. Such post-processing sample polishing routes might add cost, time, and lead time and, most

importantly, might pose difficulties for geometrically complex integrated prints. The warpage creeps in when the bed is heated in the presence of HDPE tape as the adhesive effect slowly diminishes with increasing bed temperature. Kapton tape did not exhibit any bonding of the print with it. Nevertheless, when it is applied with adhesive and the bed is heated, good interface bonding and easier removal post-printing are noted. Nonetheless, the ends of the prints are warped for the samples having a thickness of more than 6 mm. This might be due to the higher time lag between the subsequent depositions of layers. With increasing print dimensions (length in the present case), such a time lag increases faster cooling of the earlier layer by the time the next layers deposition initiates. Such observation requires a suitable thermoplastic elastomer that exhibits rubber-like behavior without undergoing vulcanization. Styrene-ethylene-butylene-styrene, also known as SEBS, is one such linear triblock copolymer polymer that is strong and flexible. Kraton™ SEBS FG1901, supplied by RishiChem Distributors Pvt. Ltd., Chennai, is used as the substrate. The printed samples exhibited moderate to excellent adhesion with a substrate based on bed heating conditions and easy detachment post-printing without any warpage. The samples are allowed to cool in the chamber until they reach room temperature to minimize the warpage and residual stresses. The Kraton™ SEBS FG1901 substrates are checked for the printing of all the samples (H, H20-H60, SH20-SH60) and performed satisfactorily.

Table 3.2 Evaluation of substrates used for 3DP.

Substrates	Observations
HDPE tape without bed heating (BH)	Good adhesion, Removal difficulty post printing
HDPE tape with BH	Good adhesion, Warped print
Kapton tape without adhesive without BH	Poor adhesion of samples with substrate
Kapton tape with adhesive and BH	Good adhesion, Easily detachable, Warped prints > 6 mm thickness
Kraton™ SEBS FG1901 without BH	Moderate adhesion of samples with substrate.
Kraton™ SEBS FG1901 with BH	Excellent adhesion, Easily detachable without any warpage

3.3.3 Adhesion

The adhesive bonding between the first layer of the print and the substrate depends on the bed and chamber temperature Table 3.2. Figure 3.2a presents representative print images after peeling the samples from the substrate at different bed and chamber temperatures. The improper adhesion results in non-uniform surface texture in case of 80°C bed temperature and for chamber temperatures of 45-75°C Figure 3.2a. Increasing bed temperature to 100°C, improper raster diffusion at the base layer forms rough surface and void formations. The perfect bonding, uniform texture, and good quality sample without any defects are observed when the bed and chamber temperatures are maintained at 120 and 75°C, respectively Figure 3.2a. The uniform and same texture on the bottom and uppermost layers of the printed samples are crucial to render similar stress states under applied loads. The chamber temperature is vital in controlling delamination at the skin-core interface and within the layers Figure 3.2b. The delamination is significant in the HDPE and their foam prints with larger dimensions due to the higher time lag of printing, resulting in differential cooling rates of the individual layers and higher temperature gradient existing between the layer to be deposited and the earlier laid layer. The appropriate chamber temperature can reduce the temperature gradient between the nozzle, layer, and bed temperatures. Figure 3.2b, below 75°C chamber temperature, delamination is observed at the skin-core interface and within the layers. The visual observation Figure 3.2b and the micrographs presented in Figure 3.2c and Figure 3.2d depict an effect of differential cooling in the form of wavy layers, delamination at the skin-core interface region, and voids within the layers at lower chamber temperatures. The defect-free sandwich is also presented in Figure 3.2b, with its micrograph in Figure 3.2e. The parallel layers with a seamless interface are clearly visible, signifying the effect of chamber temperature (75°C) on the printing of multi-material systems, a syntactic foam cored sandwich in the present investigation.

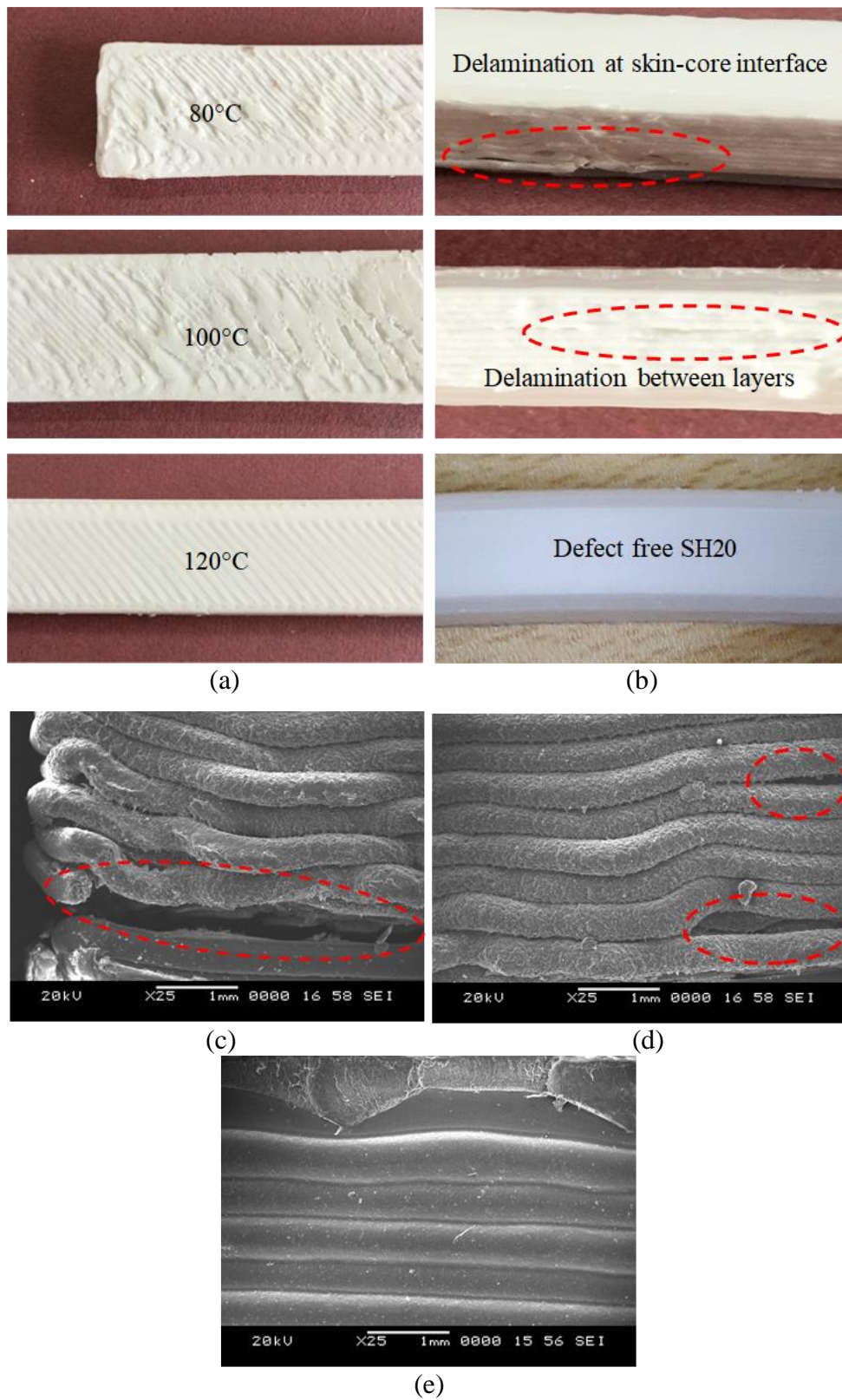
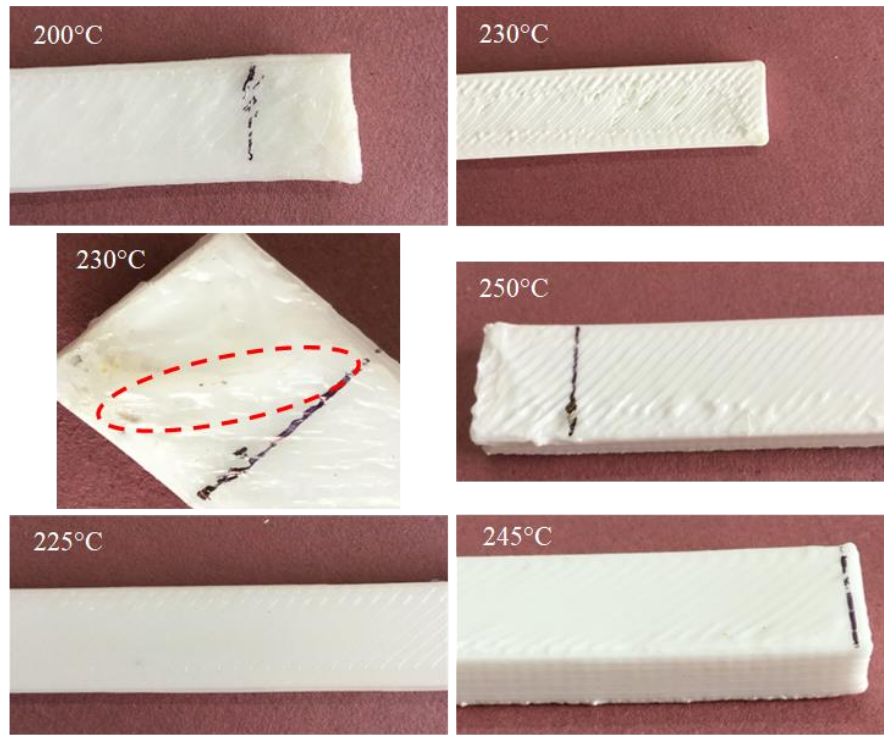


Figure 3.2. Representative print images (a) at 80-120°C bed temperatures with 45-75°C chamber temperature range (b) of SH20; Micrographs of (c) delamination at skin-core interface (d) delamination within layer and (e) defect free sample.

3.3.4 Improper flow of material

In printing core and sandwich structures, the flow of material from the nozzle plays a very important role in realizing completely rigid and dense parts. Nozzle (N1 and N2) temperatures and extrusion multiplier affect the material flow. The temperature of N1 varies from 200-230°C Table 3.1, which carries HDPE filament. N1 temperature held at 200°C results in non-uniform layer deposition, as seen in Figure 4a. The temperature of 230°C enables more material flow leading to bulk material deposition at different locations along the sample length. One such location of bulk deposition is marked in Figure 3.3a. The material continuously flows smoothly without any difficulty when N1 is set at 225°C Figure 3.3a. N2 is maintained at 200-230°C for printing H20. A similar observation is noted during the printing of HDPE through N1. Hence N2 is set at 225°C for printing H20. Figure 4b presents representative print images of H60 as this composition has maximum GMB content, i.e., the lowest content of HDPE across the chosen compositions. While printing H60, N2 is set initially at 230°C. As expected, due to lower HDPE content, small pockets Figure 3.3b are formed at several locations signifying that material did not get deposited. Such an observation might be due to the increased viscosity of H60 because of a much lower melt flow index (MFI) as compared to H and H20 compositions (Bharath HS et al. 2020). Subsequently, to increase the flow of the material, N2 is set at 250°C. The higher nozzle temperature made the material flow out continuously but with lumped deposition at several locations. Lowering the N2 temperature by 5°C (i.e., at 245°C) resulted in a good print, as seen in Figure 3.3b. Similar observations are noted while printing H40 through N2. The extrusion multiplier, as listed in Table 3.1, is the volume of material flowing out of the nozzles. This parameter decides the raster cross-section, which is dependent on MFI estimations. If the MFI reduction is lower than 60%, the extrusion multiplier is chosen as 1; otherwise, it is set at 1.2 (Bharath HS et al. 2020).



(a) (b)
Figure 3.3. Prints through (a) N1 and (b) N2.

3.3.5 Prime Pillar

Printing sandwich structures using a single nozzle is more difficult than printing with two nozzles. This is due to the time lag between the unloading of HDPE filament after skin printing and the loading of foam filaments for core printing. As the time lag increases, the earlier deposited layer solidifies before depositing subsequent layers of the core. Thereby, subsequent layer deposition results in a higher thermal gradient leading to improper layer diffusions, higher residual thermal stresses, greater shrinkage, and void/pocket formations resulting in defective prints. Further, foam print has to be resumed precisely from the predefined position. There is a good possibility of the nozzle hitting the previously deposited layers. Though this scenario is machine-dependent, isolating such a situation might widen the scope of all the commercially available 3D printers irrespective of their additional features, which comes at a cost. Hence, in the present work, N2 is fed with the foam filament against the printing support structure. Nonetheless, N2 remains idle while N1 is engaged in skin printing leading to improper material flow through N2 when it comes to action. This issue can be resolved by printing a prime pillar Figure 3.4a, a small additional

print beside the main print. Figure 3.4b and Figure 3.4c present prints without and with the prime pillar.

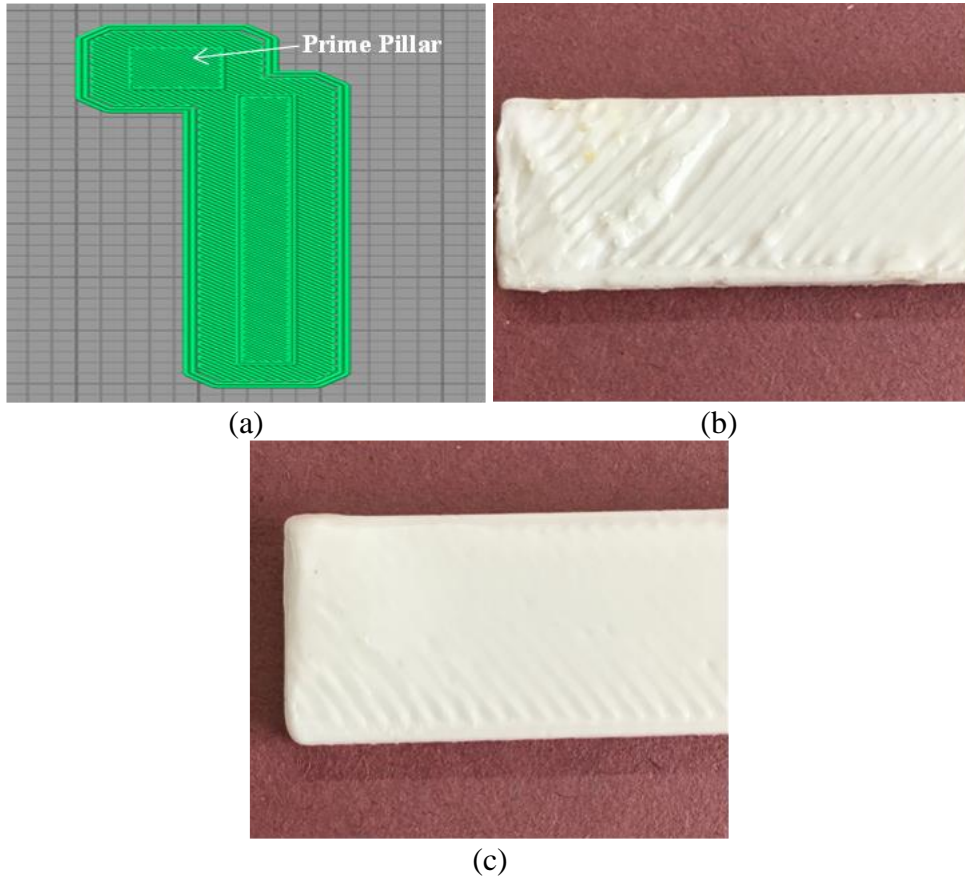


Figure 3.4. (a) Schematic representation of the prime pillar, print (a) without and (c) with prime pillar.

3.3.6 Warpage

One of the major problems in the 3D printing of HDPE and its foams is the warpage. The bed temperature is one of the critical parameters to control the warpage in the printed samples. Other printing parameters are set to suitable values based on the earlier discussions. Figure 3.5a presents a representative print image for H60. Similar observations are noted for all the printed cores. At lower bed temperature (80°C), the post-printing warpage is observed at the ends; at a relatively higher temperature (100°C), its location shifted at the center lengthwise. At 120°C, H-H60 cores are observed to be printed without any warpage, as seen in Figure 3.5a. Nonetheless, this scenario is expected to change in the sandwich due to the HDPE skin and foam core interface. The lower thermal gradient between suitable N1, N2, chamber temperatures, and bed temperature might be the reason for such a defect-free core

print. The warpage in the sandwich is observed to be multifold, as expected, due to different printing temperatures, melt flow index (MFI), and coefficient of thermal expansion (CTE). The print images for the representative SH60 sandwich are presented in Figure 3.5b. HDPE shrinks more than GMB/HDPE due to higher MFI and CTE. Though the suitable bed temperature for HDPE printing is 120°C, for sandwich prints, it is varied from 80-120°C to analyze warpage magnitude. The warpage magnitude post-printing at the sample ends was observed to be 10-20 mm, and 2-5 mm in SH20-SH60 at 80 and 100°C, respectively. The printing nozzles begin and terminate the printing at the sample ends, which might trigger the warpage at the ends for lower bed temperatures due to a higher thermal gradient between the nozzle and bed temperatures. The bed temperature of 120°C is considered suitable for sandwich samples Figure 3.5b.

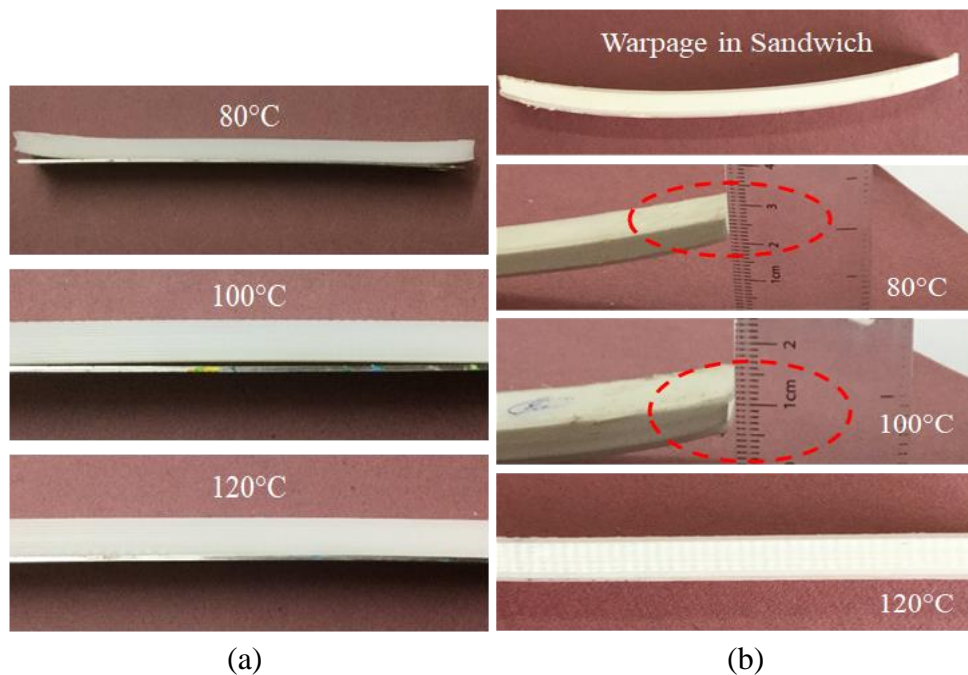


Figure 3.5. Warpage in representative (a) H60 (core) and (b) SH60.

3.3.7 Layer offset

Offsetting the layers is a major problem in sandwich printing using multi nozzles. The precise distance between the nozzles, which needs to be measured periodically, influences offset and, in turn, the print quality. The slight change in offset value deteriorates the print, as seen in Figure 3.6a. The mechanical elements and the associated errors need to be compensated using the precise measurements between the

nozzles, which needs to be set as an offset for N2. Figure 3.6a also shows the sample printed with a precisely measured offset value. These offset values play a crucial role in printing curved sandwich panels and are the future scope of this work.

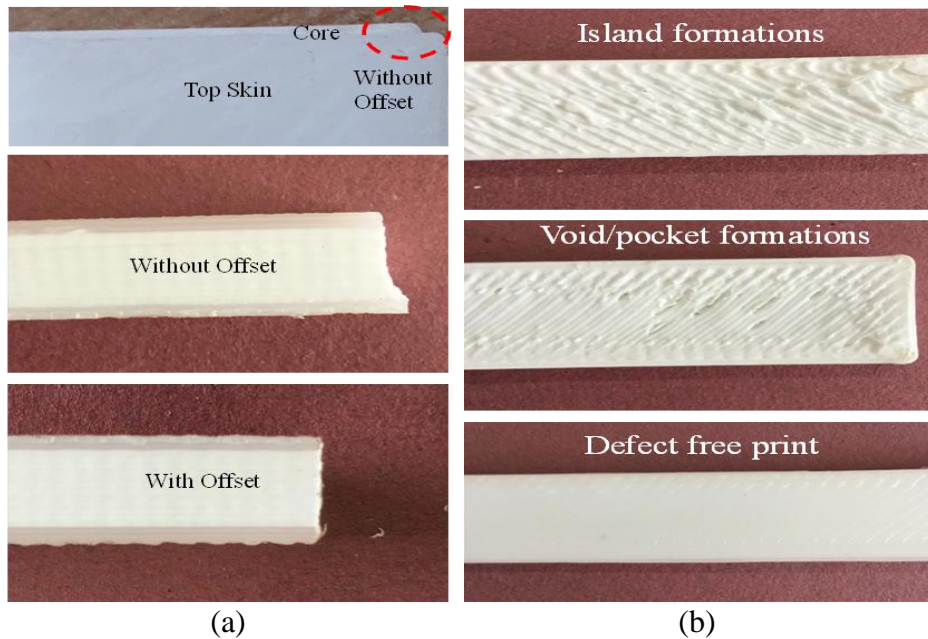


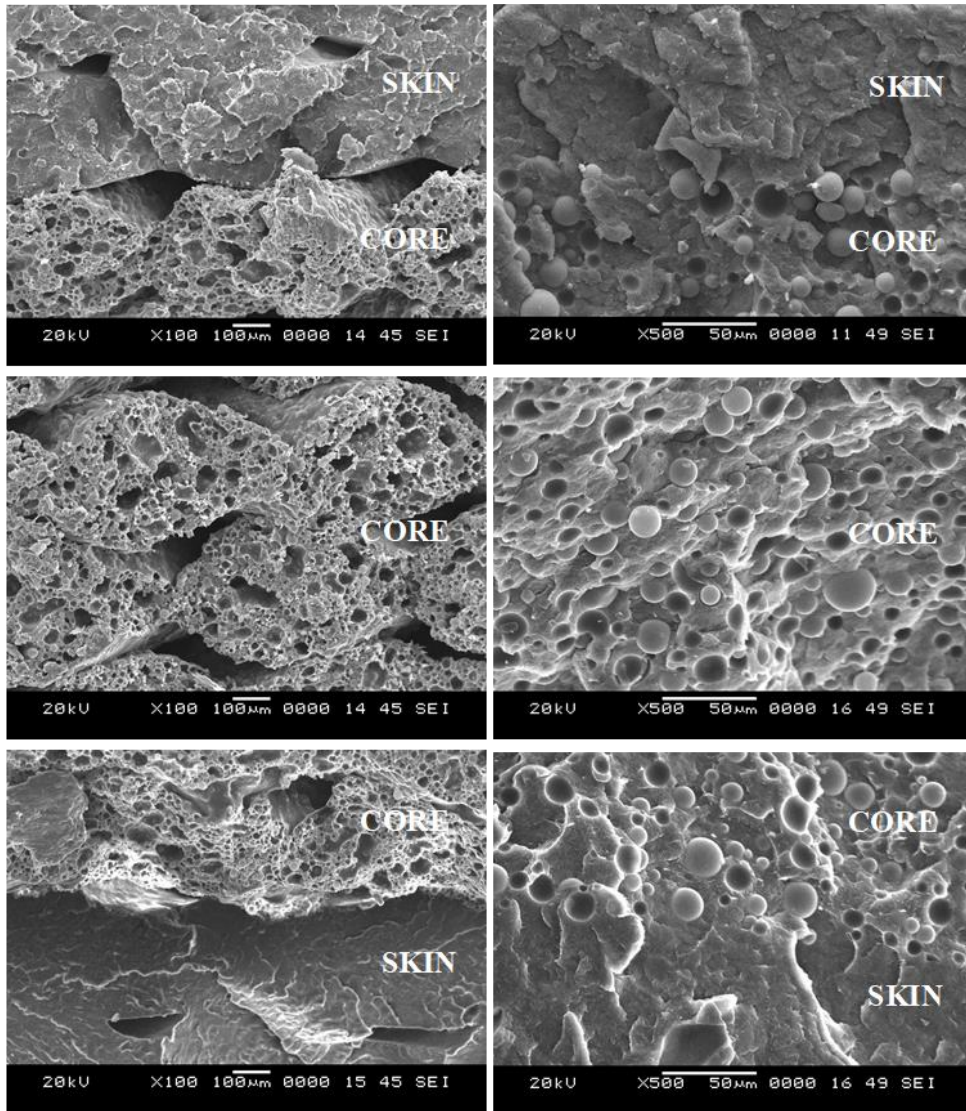
Figure 3.6. Representative sandwich prints for effect of (a) layer offset and (b) print speed.

3.3.8 Printing speed

The surface quality of the prints depends on the printing speed, which is taken in the range of 30-40 mm/sec Table 3.1, with all the other prevailing printing parameters set at suitable values. The samples printed at 30 mm/sec display small islands, as seen in Figure 3.6b. This might be due to higher heat concentration at the localized area for a longer time at lower speeds. Higher printing speed (40 mm/sec) exhibits voids/pockets due to reduced deposition time. The printing speed of 35 mm/sec results in a good smooth surface with a distinct, equally spaced raster. The layer thickness is maintained constant at 0.5 mm to precisely estimate the number of layers to be deposited for an 8 mm thick sandwich in addition to modeling simplicity in thermo mechanical analysis using FE simulations. All the core and sandwich configurations are printed at 100 % infill, rectilinear pattern, and $\pm 45^\circ$ raster angle with two outer perimeter lines and a raft offset of 50 mm. The suitable printing parameters for skin (H), core (H20-H60) and sandwich composites (SH20-SH60) are represented in Table 3.1.

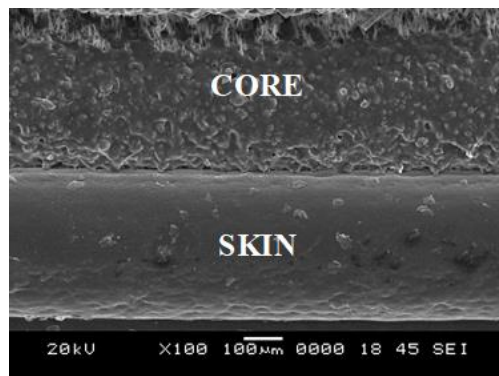
3.3.9 Micrographic Investigation

The freeze fractured micrographic investigations are carried out on syntactic cored sandwich composites printed using the lowest Figure 3.7a and suitable values Figure 3.7b, as listed in Table 3.1. The effect of improper adhesion and inadequate material flow due to the lower nozzle, bed, and chamber temperature is clearly visible in Figure 3.7a. The voids in the skin and skin-core interface are due to localized diffusion between the raster amid 100% infill. Nonetheless, such a structure resembles two and three-phase skin and syntactic foams, respectively, that might enhance energy-absorbing capabilities at the expense of the required strength. Figure 3.7b exhibits a seamless interface between the skin-core-skin interface without any voids and defects, as discussed earlier. FFF based 3D printing is typically comprised of two thermal cycles, one during filament extrusion and the other when the material flows through printer nozzles for layered deposition. Though authors could successfully print a syntactic foam cored sandwich at once, estimating thermal stresses is essential for achieving thermal equilibrium faster by reducing the heat gradients across the nozzle, bed, and chamber temperatures during and post-printing. The sandwich's warpage is substantial compared to the core, as seen in Figure 3.5. The sandwich exhibits warpage post-printing without any delamination between the skin and core Figure 3.5b, signifying the non-uniform thermal stresses. Nonetheless, suitable printing parameters resulted in the sandwich without any warpage, as seen in Figure 3.5b. By knowing the temperature distribution in the sound quality sandwich post-printing, particularly across the skin-core interface, localized heating/cooling mechanisms can be deployed to reduce the residual thermal stresses further, which might lead to a sandwich with much better mechanical properties. Thereby, in the present work, FE simulation of SH60 is adopted to estimate the temperature distribution and thermal stresses using the suitable printing parameters, as listed in Table 3.1.



(a)

(b)



(c)

Figure 3.7. Freeze fractured micrographs of representative 3DP sandwich (a) using lower and (b) suitable printing parameters from Table 3.1 (c) micrograph of the sandwich along thickness.

3.4 Thermo Mechanical Analysis

3D printing involves complex heat and mass transfer phenomenon that affects the dimensional accuracy of the final part. The thermo mechanical FE simulations are carried out using ANSYS 2020 R1 and suitable printing parameters as boundary conditions to visualize the temperature, and thermal stress distributions in 3D printed SH60 sample (post-printing). A 3D steady-state thermal analysis is conducted, and the temperature distribution is used as load input for static-structural analysis. The Hex20 element having an element size of 1 mm, is used in FE simulations. In pre-processing, the properties of the skin and core are defined. Table 3.3 presents the material properties of the SH60 sample used in the FE analysis. The sandwich sample (bottom and top skin each of 1 mm and foam core of 6 mm thick) is modeled with dimensions of 180×18×8 mm³ with layer thickness of 0.5 mm, totaling 16 layers. Before meshing, sandwich elements (skin-core-skin) are coupled for effective heat transfer. Figure 3.8a and Figure 3.8b present a sandwich FE model and mesh, respectively. The free mesh is adopted, forming 25920 elements and 138799 nodes. The convection boundary conditions are applied, as seen in Figure 3.8c, and subsequently, analysis is carried out for temperature distribution. The obtained temperature data is taken as load data for static-structural analysis to observe the stress distribution in 3D printed samples through FE simulations.

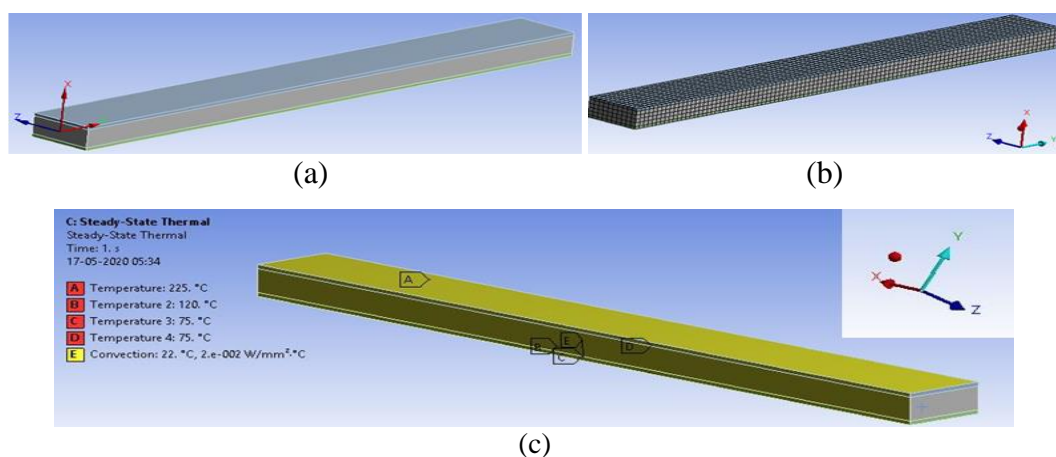
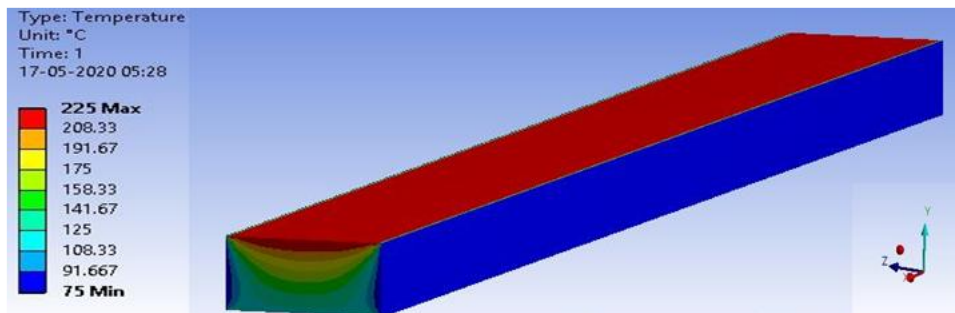
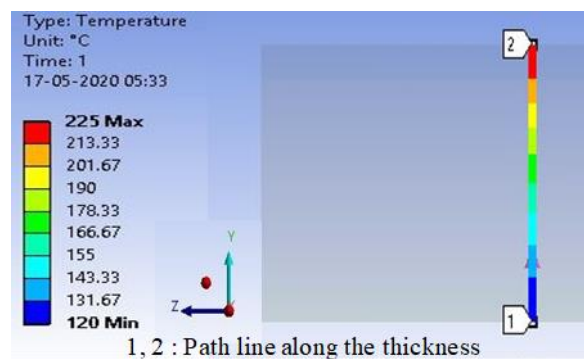


Figure 3.8. Sandwich (a) model and (b) mesh and (c) boundary conditions used in FE analysis.

The results of thermal analysis in the form of temperature distribution are presented in Figure 3.9. It is observed that temperature distribution varies from skin to core since convective heat transfer boundary condition is applied wherein chamber temperature is set at 75°C. The bottom skin will have a temperature slightly higher than the bed temperature (120°C). The top layer of the skin is subjected to 225°C. The sequential deposition of the material is observed clearly in the thermal analysis. Cyclic cooling and heating of the extruded material can be seen as minimum temperature distribution at the bottom and maximum at the top layer. The bottom layers cooled and heated cyclically as the heat gets conducted between layers. The highest temperature is noted for the just-deposited layer, whereas the side faces of the sandwich are cooling at a faster rate due to convection. The temperature distribution along the thickness of the sample is presented in Figure 3.9b. It is observed that the top skin. Figure 3.9c has the maximum temperature, and it extends to the skin-core interface. In the core Figure 3.9d, the top layer has maximum temperature while the temperature distribution at both sides of the core is lower due to convective heat transfer. Figure 3.9e presents the temperature distribution in the bottom skin, which is almost equal to the bed temperature.



(a)



(b)

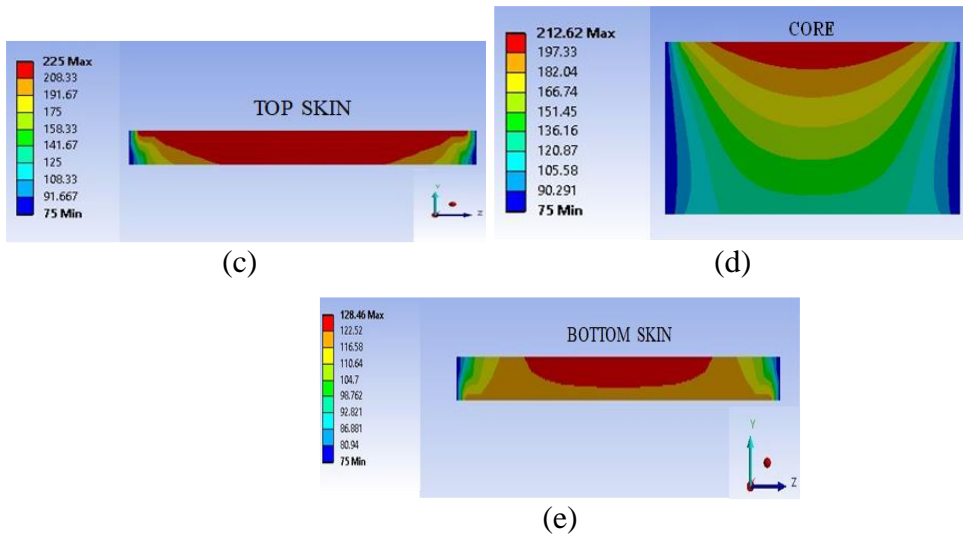


Figure 3.9. Temperature distribution in (a) sandwich (b) thickness direction (c) top skin (d) core and (e) bottom skin.

The thermal analysis results of SH60 are imported as the load data for analyzing the thermal stress distribution. Similar boundary conditions are imported from the thermal analysis for structural analysis and the frictionless support for the bottom surface. It is observed that stresses are maximum in the top skin near the lateral surfaces and minimum at the core (Figure 3.10a. Post analysis, stresses at the width and lengthwise center are presented in Figure 3.10b and are tabulated in Table 3.4.

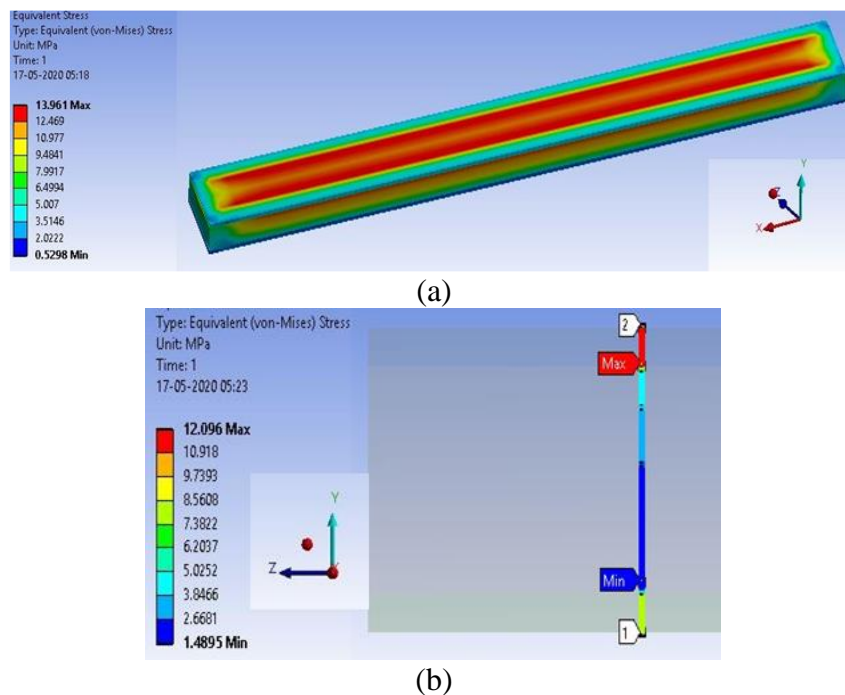


Figure 3.10. Stress (MPa) distribution in (a) SH60 (b) along the thickness.

Table 3.3. Material properties used for FE simulation.

SH60	Density (kg/m ³)	CTE (/°C)	Thermal conductivity (Wm ⁻¹ K ⁻¹)	Specific heat (cal/g-K)	Modulus (MPa)	Poisson's ratio
H60	740	8.84×10 ⁻⁵	0.3469	0.3887	1199.26	#0.296
H	950	1.48×10 ⁻⁴	0.4729	0.4617	810.25	0.425

(Bharath Kumar BR et al. 2016),(Bharath HS et al. 2020),(ISO22007-2:2015 2015)

Table 3.4. Temperature and stress distribution along the sandwich thickness computed from FEA.

Region	Sample thickness (mm)	Temperature distribution (°C)	Stress distribution (MPa)
Top Skin	8.0	225	11.54
	7.5	218.91	11.77
	7.0	212.86	12.01
Core	6.5	204.47	4.29
	6.0	196.47	3.90
	5.5	188.63	3.52
	5.0	181.02	3.13
	4.5	173.65	2.75
	4.0	166.53	2.37
	3.5	159.67	2.11
	3.0	153.06	1.86
	2.5	146.68	1.64
	2.0	140.51	1.45
	1.5	134.5	1.32
Bottom Skin	1.0	128.46	7.87
	0.5	124.21	7.89
	0.0	120	7.93

The temperature and stress distribution along the thickness of the sandwich are presented in Figure 3.11a and Figure 3.11b, respectively. Figure 3.11a depicts the temperature distribution through the thickness of SH60. This plot shows that temperature increases from the bottom to the top skin through the foam core. The bottom and top skins proximity, respectively towards the bed and nozzle, is the reason for such an observation. The stress in the bottom skin is dependent on the bed temperature. The stress distribution in the core is designated in four (I – IV) zones. The stress at the bottom skin-core interface suddenly changes the trend and decreases sharply, as seen from zone I in Figure 3.11b.

The decline continues up to 0.5 mm from the skin-core interface towards the core. This might be due to the differential thermal properties of skin and core in addition to the lower thermal conductivity of H60 compared to H. The stress levels in zone II and III increases from 1.32 to 4.29 MPa. This substantially lowers stress values in the core (zone II and III) due to hollow GMB particles, which effectively resist heat transfer because of hollow space within the microspheres. The thermal conduction mode is predominant in neat HDPE, i.e., skin in the present case. I influence the heat transfer mechanism in GMB/HDPE core) conduction between HDPE and GMB ii) convection between the gas molecules present within the hollow space of GMBs (Waddar Sunil et al. 2018). As the GMB content in the HDPE matrix increases, higher resistance to heat flow substantially reduces the thermal stresses developed in the foamed cores as compared to the skins. The rate of thermal stress rise in III is slightly higher than in II. Such a marginal change in the slope of III as compared to II might be due to zone III's proximity towards the top skin, which is printed at 225°C. The sudden rise in stress level is observed in zone IV, as it is closer to the top skin.

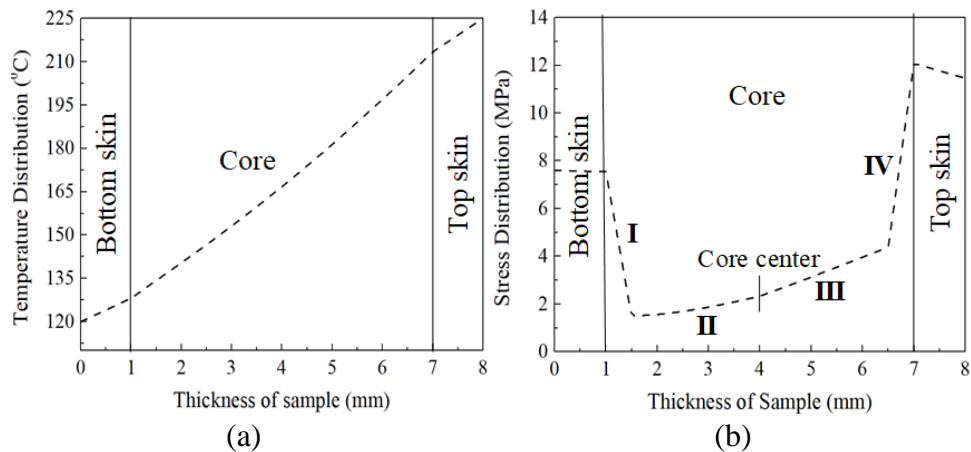


Figure 3.11 (a) Temperature and (b) stress distribution along the sandwich thickness post printing.

The FE simulations help in visualizing the stresses at critical locations. In the present investigations, such locations are at the skin core interface wherein drastic stress level changes are noted though the simulations are carried out at suitable printing parameters. Though the simulation did not show any warpage as expected due to suitable printing parameters, stress levels within the core can be minimized further to achieve thermal equilibrium in the foam cores. The possible strategies could be a)

reducing the infill %, b) usage of three-phase syntactic foams c) adopting localized cooling. The thermal stress levels in the skin can also be lowered by inducing voids (air/gas entrapment or raster gaps) and lowering the infill%. Nevertheless, the mentioned approaches might compromise strength amid higher damping properties. These strategies can be used based on the envisaged applications.

3.5 3D printing of functionally graded foams and sandwiches

3D Printing of functionally graded foams [FGF-1 (H, H20, and H40 - top side), FGF-2 (H20, H40, and H60 - top side), and FGF-3 (H, H20, H40, and H60 - top side)] and their respective sandwiches [FGSF-1 (H - lower skin; Core - H, H20, and H40; H - upper skin), FGSF-2 (H - lower skin; Core – H20, H40, and H60; H - upper skin) and FGSF-3 (H - lower skin; Core - H, H20, H40, H60; H - upper skin)] using FFF technique is not explored yet. So in the present work printing strategy followed for the 3D printing of FGFs and FGSFs is explained. For explanation purposes, FGF-3 of a total 4mm thickness is selected. Initially optimized 3D printing parameters, mentioned in Table 3.1 are selected while developing these graded foams. The two nozzles (N1 and N2) of a 0.5 mm diameter FFF 3D printer procured from AHA 3D Innovations, Jaipur, India, have been exploited to develop FGFs. 3D printing of FGF-3 is done by inserting HDPE (H) filament in N1 and H20 in N2. Initially, a 0.5 mm raft of H is printed by N1, and subsequently, the first material composition of H is printed until the required thickness of 1 mm gets deposited. Immediately after that, N2 sweeps in action in place of N1 with offset set in simplify 3D and deposits H20 for the next 1 mm. After depositing two material compositions (H and H20), the machine is paused for 30 seconds, nozzles are lifted to a 10 mm height, N1 is replaced with H40, and H60 is fed in N2. Both N1 and N2 are purged for 30 seconds to ensure an adequate flow, and nozzles are positioned to the starting location for printing. The printing cycle is repeated for H40 and H60 to print 1 mm each by N1 and N2, respectively. Post printing, FGF of 4 mm is allowed to cool on the machine bed until room temperature to minimize residual stresses. A similar procedure is followed for print FGF-1 (H, H20, and H40 - top side), FGF-2 (H20, H40, and H60 - top side), FGSF-1 (H - lower skin; Core - H, H20, and H40; H - upper skin), FGSF-2 (H - lower skin; Core – H20, H40, and H60; H - upper skin) and FGSF-3 (H - lower skin; Core - H,

H20, H40, H60; H - upper skin). Here the frequency of the filament replacement depends upon the number of material of gradation present in the sample to be 3D printed. A pictorial representation of 3D printed samples and the sequence followed while developing is shown in Figure 3.12.

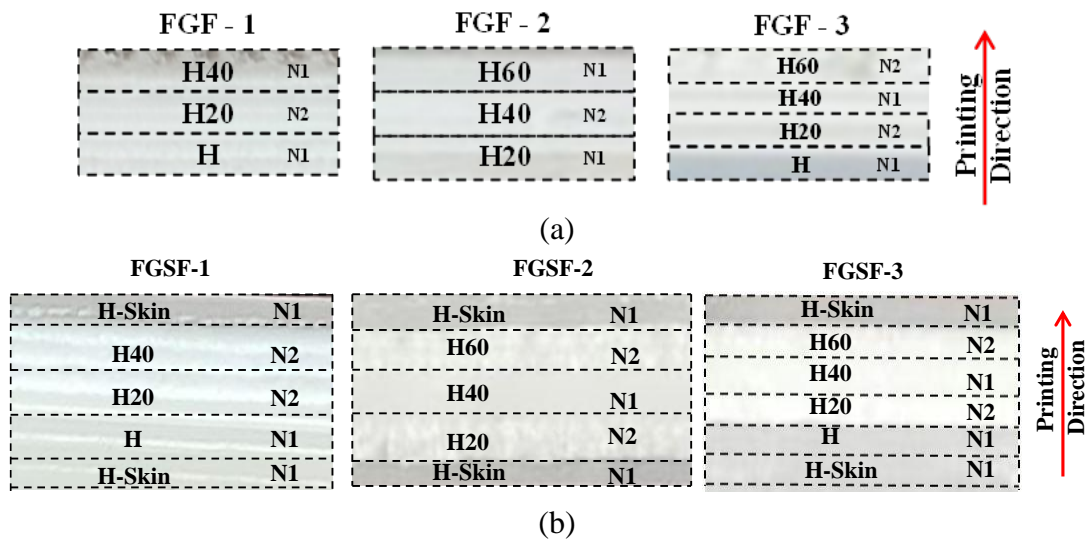


Figure 3.12 3D Printing strategy for FGF and FGFS

3.5.1 SEM analysis of 3D printed FGF and FGFSs'

The micrographic analysis is performed to observe the filler sustainability, filler and matrix interface, and bonding between the layers. Figure 3.13a presents the micrographic image of FGF. In microscopic analysis, it is observed that the layers are properly fused, leading to the formation of seamless bonding, which helps in effective load transfer between different material compositions. Even at higher magnification, GMBs breakage is not observed, which resembles that the parameter chosen for blending, filament extrusion, and 3D printing is feasible Figure 3.13b.

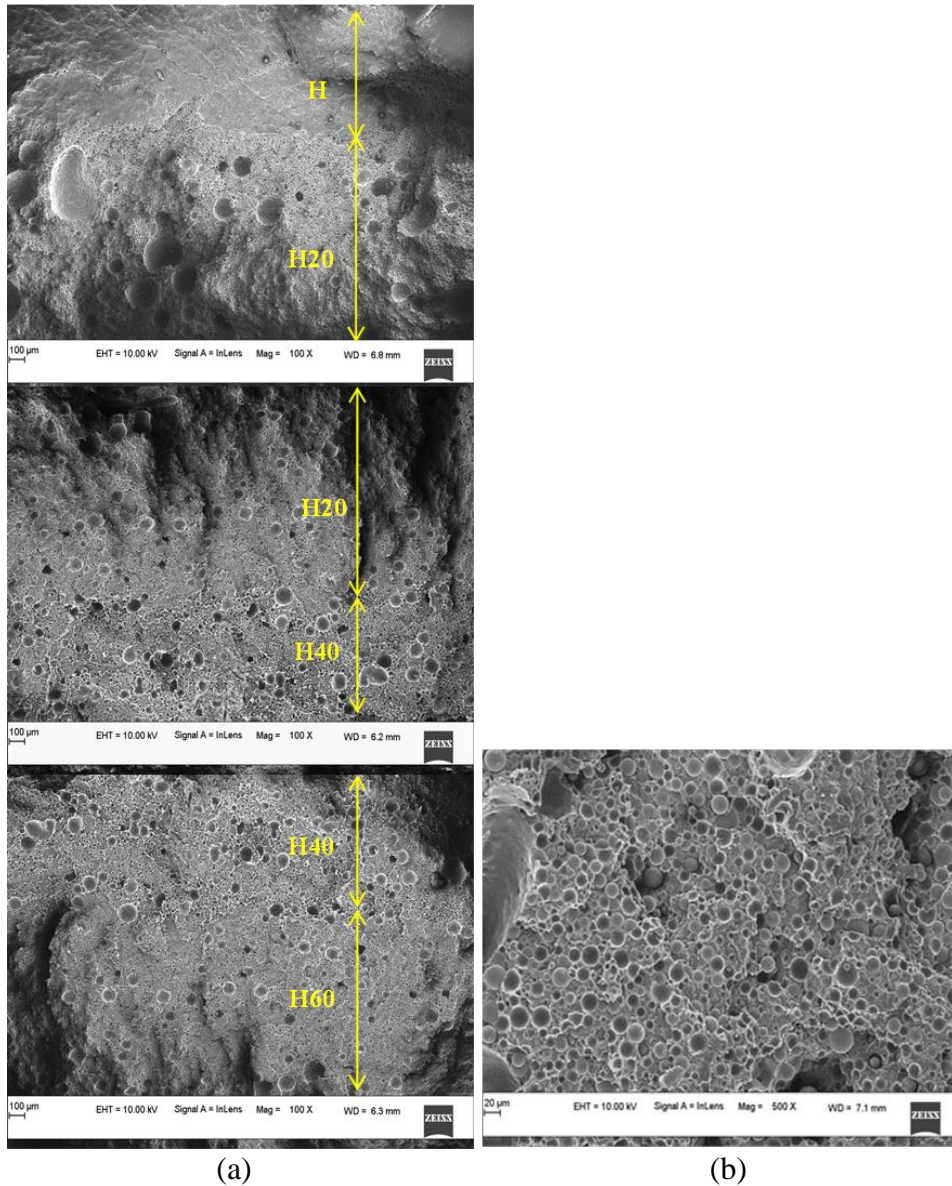


Figure 3.13 Representative SEM images of (a) FGF interfaces and (b) GMB Sustainability

3.6 Micro CT

The micro-CT is carried out on 3D printed graded foams to explore the interfacial bonding and porosity distribution. The results of the micro-CT are presented in Figure 3.14. There is no interfacial defect/delamination between the 3D printed layers of HDPE and foam interfaces, as evident from the CT scan images. The micro-CT imaging shows that the HDPE zone is porous-free. Among foams, minimum microporosity is observed in H20 due to the lower filler restriction forces toward matrix movements at lower GMB loadings. Though such porosities might compensate

for few mechanical properties, these in-situ voids enhance weight-saving potential, which might not be possible alone with GMBs.

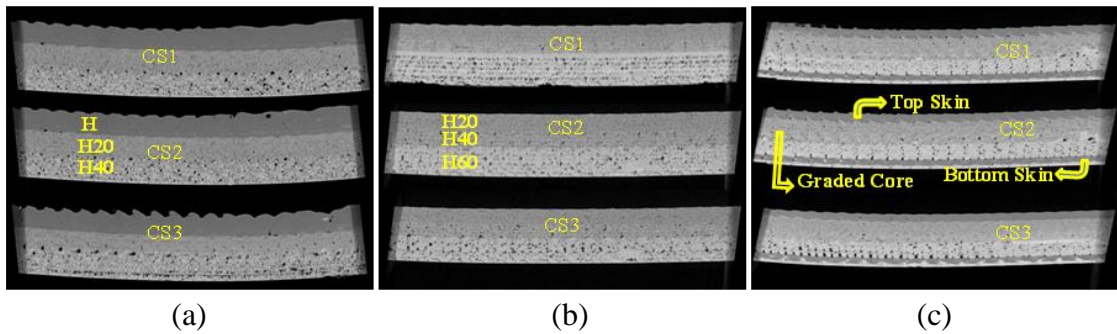


Figure 3.14. Micro CT of (a) FGF-1, (b) FGF-2 and (c) FGSF-2.

(*CS=Cross Section)

3.7 Surface roughness

Surface roughness is one of the major parameters that significantly affect the part quality. Moreover, as the current work deals with the 3D printing (layer-by-layer process) of the filler reinforced composite, it significantly affects the part quality instead of controlling the surface roughness of the sample by post-processing operations like finishing, polishing, etc. It is important to control it at the manufacturing stage by studying the different parameters of the manufacturing method by observing its effect on controlling the surface roughness. As the current work deals with 3D printed syntactic foam composite, in current work effect of filler volume fraction, layer height, and printing speed is studied. The surface roughness of the 3D printed sample along its circumference depends on the layer height and at top and bottom surfaces due to rasters on it. So the initial study has done on a different surface, as mentioned above, by printing the sample at 0.5mm layer height. A 3D non-contact profilometer is used for analyzing the surface roughness by choosing 5 μm as the step size. Initially, 3D printed pure HDPE, and H60 samples are tested for surface roughness. It is observed that the average surface roughness (Ra) for HDPE and H60 are 8.965 and 37.49 μm , and the mean depth of furrows is 9.109 and 71.57 μm . The 3D surface plot of amplitude and furrows is shown in Figure 3.15. These furrows on the surface are due to filler particles in the matrix material and gaps formed due to rasters. This minimum surface roughness value of HDPE is due to its good flow ability, and the comparatively higher surface roughness of H60 is due to furrows

formed due to restrictive filler forces. These furrows on the surface play a crucial role in restricting the flow of material deposited over the past layer, leading to the porosity between the layers. This porosity helps in enhancing the weight-saving potential. The maximum height of roughness profile (Rz), average surface roughness (Ra), and root mean square (RMS) deviation of the roughness profile (Rq) value of pure HDPE and composite with a high filler percentage of 60 volume % are mentioned in Table 3.5. The average surface roughness value for H, H20, H40, and H60 are mentioned in Table 3.6. From the results, it is observed that with an increase in filler percentage, surface roughness increases.

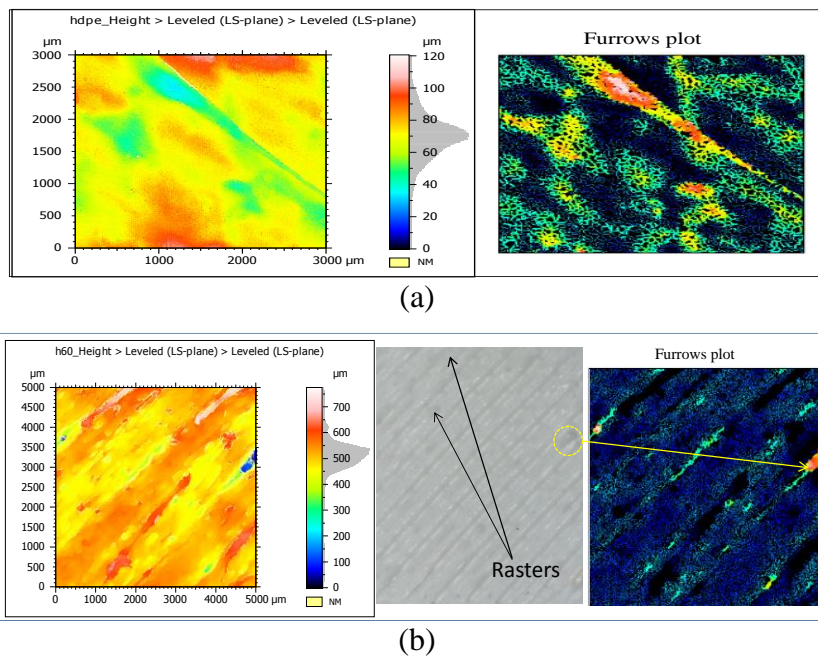


Figure 3.15. Surface roughness of (a) HDPE and (b) H60.

Table 3.5. Surface roughness values of HDPE and H60.

Parameters	Amplitude of parameters	
	HDPE	H60
Maximum height of roughness profile (Rz) (μm)	120.5	774.5
Average surface roughness (Ra) (μm)	8.965	37.49
Root-mean-square (RMS) deviation of the roughness profile (Rq) (μm)	11.73	55.36

Table 3.6. Average surface roughness of foams.

Composite	HDPE	H20	H40	H60
Average surface roughness (Ra) (μm)	8.96	19.73	24.90	37.49

This surface can be controlled by choosing less layer height, but as the current work deals with the FGM, In order to maintain the layer multiplier corresponding to the sample thickness, layer height is chosen as 0.5mm. The surface roughness of the sample over the circumference is measured in two directions (1) Along the layer and (2) Across the Layers, as shown in Figure 3.16, and Rz, Ra, Rq values are mentioned in Table 3.7.

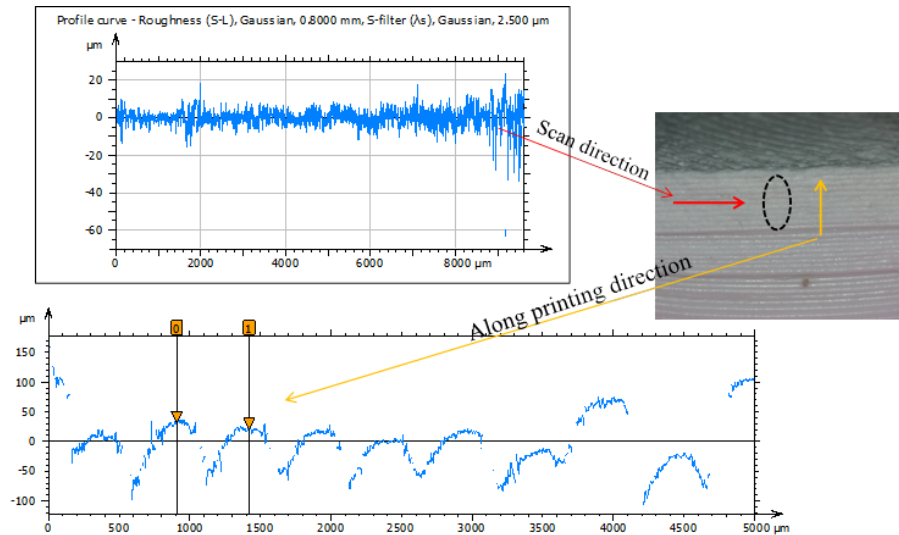


Figure 3.16. Surface roughness profile curve of 3D printed sample in different directions of printing.

Table 3.7. Amplitude parameters along thickness direction & along width direction.

Amplitude paramètres	Along thickness direction	Along direction of width
Rz (μm)	111.1	27.5
Ra (μm)	20.57	3.06
Rq (μm)	25.34	4.03

3.8 Density

Physical property like density plays a crucial role in deciding the weight reduction potential of the foams. In accordance with ASTM D792-20, experimental densities of 3D printed FGF and FGFS beams are estimated using the contech analytical balance.

To estimate the accuracy of the experimental densities, theoretical densities of all 3D printed FGF and FGFSs are calculated using the rule of mixture Equation 2.2. For evaluation and comparison of weight reduction potential, the experimental density of the H, H20, H40, and H60 are taken from our previous work (Bharath HS et al. 2020). Measured experimental densities and calculated theoretical densities, weight reduction potential, and void percentage of FGF and FGFSs' are mentioned in Table 3.8 and Table 3.9.

Table 3.8. Density and weight saving potential of FGFs'.

FGFs Type	Plain foams					FGFs					
	Layer	Foam Type	ρ_{th} (kg/m ³)	ρ_{exp} (kg/m ³)	ϕ_V (vol. %)	Weight Saving (%) Potential w.r.t H	ρ_{th} (kg/m ³)	ρ_{exp} (kg/m ³)	ϕ_V (vol. %)	Weight Saving (%) Potential w.r.t H	
1	1 (top)	H40	810	746±18	7.9	19.53	880	841.56±114.36	4.36	9.22	
	2	H20	880	826±136.14	10.90						
	3	H	950	927±122.42	-----						
2	1 (top)	H60	740	668±109.73	27.94	810	746.89±147.79	19.42			
	2	H40	810	746±18	7.9						
	3	H20	880	826±136.14	10.90						
3	1 (top)	H60	740	668±109.73	27.94	845	792.24±106.24	14.53			
	2	H40	810	746±18	7.9						
	3	H20	880	826±136.14	10.90						
	4	H	950	927±122.42	-----						

Table 3.9. Density and weight saving potential of FGFSF.

FGFSF	Composition	ρ_{th}	ρ_{exp}	Void % (ϕ_V)	Weight Saving
-------	-------------	-------------	--------------	---------------------	---------------

Type		(kg/m ³)	(kg/m ³)		Potential (%)
					With respect to H
HDPE	H	950	927 ± 12	2.42	-----
FGSF1	H-H20-H40-H-H	897.5	850 ± 09	5.29	8.3
FGSF2	H-H20-H40-H60-H	845	794.3 ± 13	6.0	14.31
FGSF3	H-H-H20-H40-H60-H	871.25	810 ± 07	7.03	12.6

The results show that weight reduction potential is higher for the sample with comparatively higher GMB volume percentage. It is also observed that the percentage deviation between the experimental and theoretical densities for FGFs is 4.36, 7.79, and 6.24 due to voids induced due to residual micro-porosity in prints (Equation 2.3). The printer setting of 100% infill does not equal zero porosity, as the layered deposition results in a residual micro-porosity. In this contribution, micro-porosities are considered to be inherent in the printed material. Nonetheless, such residual voids help increase the weight-saving potential compared to syntactic foams, which is the primary advantage for buoyancy applications. Further, these voids enhance damping and energy absorption. The density of FGF-1 is 9.22 % lower than H and 12.8 % higher than H40, whereas the density of FGF-2 is 19.52 % lower than H and 11.80 % more than H60. FGF-3 density is more than FGF-2 and less than FGF-1. FGF-3 shows 18.56 % more density than H60. FGF-2 density is lesser compared to FGF-1 and FGF-3 and is due to the presence of higher GMB. These voids made 3D printed FGFs three-phase syntactic foams. Among FGFs, FGF-2 has a higher weight-saving potential (19.52 %) compared to plain HDPE. Among all FGSFs, FGSF-2 exhibited the lowest density of 0.93 and 0.98 times, respectively, of FGSF-1 and FGSF-3, having the highest weight-saving potential of 14.31 %. Compared to neat H, the densities of FGSF-1, FGSF-2, and FGSF-3 are 8.3, 14.31, and 12.6 % lower. This signifies the capability of FGF and FGSFs to substitute plain HDPE for weight sensitive applications. Further, design flexibility and complex shaped integrated components realization through 3D printing without additional tooling costs are most beneficial compared to conventional sandwich manufacturing routes.

Conclusion

3D Printing Parameters

The plain syntactic foam, functionally graded syntactic foam, and their respective sandwiches, are successfully 3D printed all at once without any defects. Among many substrates used in commercially available 3D printers for printing, SEBS FG1901 is the most suitable for printing the GMB/HDPE cored sandwich. It showed very good adhesion and exhibited an easily detachable feature post-printing. Both the nozzles available in printers are utilized for printing sandwich skin and core at once. All the printing parameters are suitable for printing H, H20-H60, SH20-SH60, FGF-1 - FGF-3, and FGSF-1 - FGSF-3 are listed below:

- Printing temperature for H: 225°C; H20: SH20 - 225°C, H40 and H60 - 245°C
- Extrusion Multiplier: H, H20, and H40 - 1, H60 - 1.2.
- Bed and chamber temperatures of 120 and 75°C, respectively.
- Speed of printing: 35 mm/s.

SEM Analysis and Micro CT

- SEM analysis revealed that layers are properly fused with each other.
- There is no observable filler failure, and this resembles that blending, extrusion, and printing parameters are selected properly without any extra shear forces.
- Interface bonding between the filler and matrix is not proper in some places, and this can be eliminated by adopting some surface treatment operations for filler.
- Micro CT scan analysis showed that there is no delamination defect between the layers.
- There is no observable porosity in HDPE layers this is due to lack of fillers restriction forces.
- Porosity percentage increases with an increase in filler percentage, and it is higher in H60 layers. This porosity helps in enhancing weight reduction potential and energy absorption.

Density

- Density of syntactic foam decrease with an increase GMB volume percentage.
- The measured density of all 3D printed syntactic foams-based FGFs is less than HDPE, signifying that foams have good weight reduction potential. 3D printed FGF-1, FGF-2, and FGF-3 have weight-saving potential of 9.27, 19.52, and 14.56 %.
- Compared to neat H, the densities of FGSF-1, FGSF-2, and FGSF-3 are 8.3, 14.31, and 12.6 % lower.
- Weight saving potential of foam helps in replacing plain HDPE with graded foams for weight-sensitive applications.

4. COMPRESSION RESPONSE

4.1 compressive behavior of functionally graded core

The lightweight FGF and FGSFs' developed in the present work can be utilized to integrate components for buoyancy-based marine applications exposed to upward thrust (hydrostatic compression force). Hence, it is mandatory to ascertain the compressive properties of this material system. Figure 4.1 presents the test setup and the representative FGF deformation post-test. The compressive stress-strain plots of 3D printed plain H, H20-H60, and FGF-1 to FGF-3 samples are shown in Figure 4.2, respectively, and the results are tabulated in Table 4.1. In-house built Matlab code calculates the compressive modulus and yield strength of the 3D printed plain foams and FGFs. All 3D-printed foams under compressive load exhibited ductile deformation without any visible crack formation over the sample surfaces during testing. The compression stress-strain graphs plotted from experimental results exhibit three regions (i) linear elastic region along with non-linear yielding zone, (ii) smaller plateau region, and (iii) densification region where an increase in the stress with minimum strain is observed. In the 3D printed samples, the crystalline structure is formed due to cross-linking of the polymer chain, offers resistance to the deformation under the applied load, resulting in higher strain stress. For all the foams in the elastic region, stress increases linearly pertaining to strain, and the slope of this linear elastic region is used to calculate the compressive modulus. This linear region is observed up to the minimum strain, less than 0.1 mm/mm. This linear elastic region terminates with a small non-linear knee-shaped curve with a positive slope, which helps compute the compressive yield strength of FGFs. This yield behavior is due to the deformation of an entangled network under high viscosity which induces inter and intralaminar shear forces (Hobeika S et al. 2000, Omar Mohd Firdaus et al. 2012). These forces promote the elongation of the residual micro-porosities and voids. These elongated voids absorb energy before getting collapsed (Jeyachandran Praveen et al. 2020). Among all the 3D printed plain samples, H60 showed higher modulus, and HDPE showed high strength. This higher strength of HDPE is due to its viscoelastic behavior, and barrier-less flow (no filler), resulting in less void formation with the compromise in weight reduction potential compared to foams. The plain foams and

FGFs might exhibit much better strength than HDPE post surface modification of the constituents, enhancing interfacial bonding between them. In the present work, constituents are used in as received conditions.

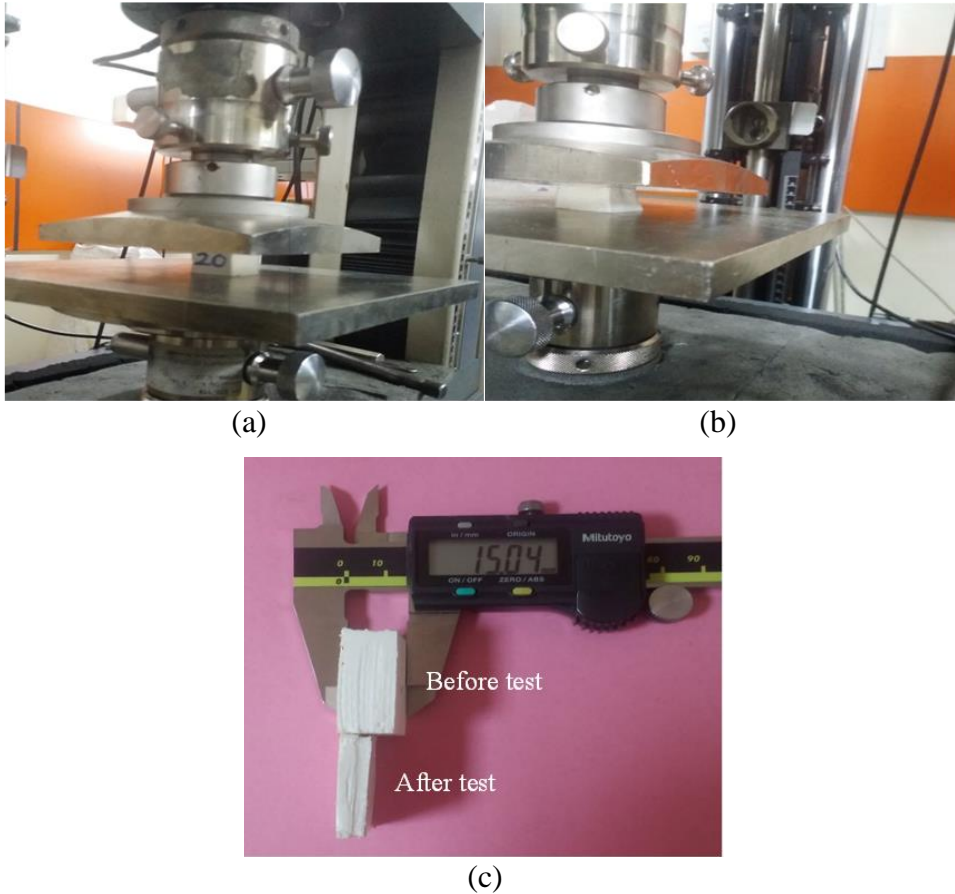


Figure 4.1. (a) Experimental Setup for flatwise compression (b) test in progress and (c) representative sample deformation post compression.

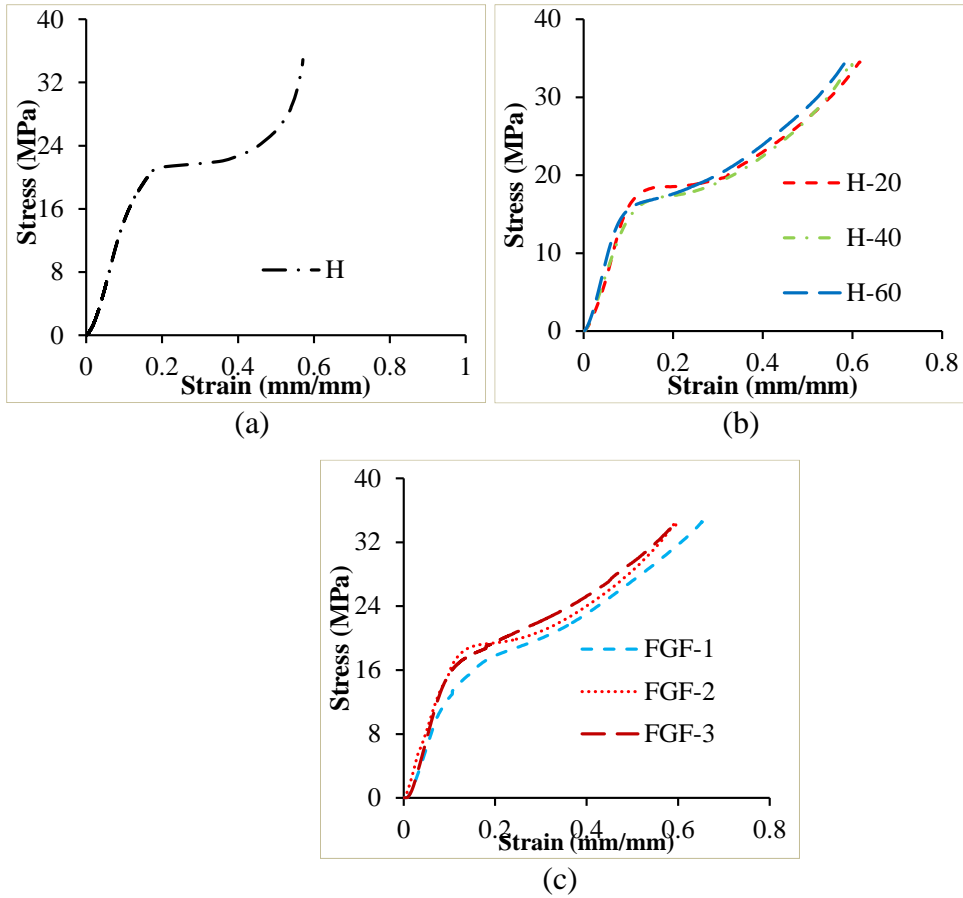


Figure 4.2. Representative Stress-Strain Plots of 3D printed (a) H, (b) Plain (H20, H40 and H60) and (c) functionally graded (FGF-1, FGF-2 and FGF-3) samples.

Table 4.1. Compressive properties of 3D printed FGFs.

Composition	Modulus (MPa)	Yield Strength (MPa)	Peak Stress (MPa)	Plateau Stress (MPa)	Energy at 50% Strain (MJ/m ³)
H	346.41±9.57	17.23±0.45	37.67±0.13	21.0±0.30	5.63±0.18
H20	332.90±13.23	15.94±0.28	34.51±0.27	18.92±0.02	5.70±0.56
H40	410.55±10.40	13.90±0.75	34.57±0.19	18.30±0.80	5.88±0.49
H60	442.18±12.28	13.89±0.16	34.40±0.02	17.54±0.19	6.30±0.67
FGF-1	373.34±9.53	14.77±0.38	34.53±0.1	18.78±0.07	6.28±0.83
FGF-2	382.52±11.80	16.67±0.08	34.48±0.05	19.54±0.12	6.24±0.54
FGF-3	345.27±9.20	12.12±0.24	33.68±0.20	18.19±0.09	7.17±0.27

The compressive modulus of foams increases with an increase in GMB volume %. Among foams, H60 showed a higher compressive modulus of 1.32 and 1.07 times that of H20 and H40. With an increase in the filler %, the yield strength of the foam is slightly reduced due to an increase in the porosity due to the residual micro-porosity. The Yield Strength of the 3D printed syntactic foams is higher for H20 than H60. They are increasing the load beyond yield strength resulting in the collapse of the in-situ voids. The collapsing of voids results in higher strain without increasing the stress leading to a small plateau region formation. The plateau region of all foams observed between 0.1 to 0.3 mm/mm of strain. The plateau region for H20, H40, and H60 is observed at stress values of 18.37, 17.31, and 17.03 MPa. The Plateau region for H20 is distinguishable, as seen in Figure 4.2b. Among foams, the plateau region is at higher stress for H20 than H40 and H60 prints. Energy absorption at 50 % strain for printed H20, H40, and H60 samples are 5.7, 5.8, and 6.3 MJ/m³. Further, with higher loads, the plateau region is followed by an increase in stress with less deformation exhibiting strain hardening phenomenon. This gradual increase in stress with lower strains is due to the densification caused by the collapse of in-situ voids, micro-porosities, and, most importantly, the failure of the hollow GMBs. Once the load increases beyond the plateau region, the filler particles start getting crushed. The void space left post GMB failure/crushing gets occupied by the HDPE matrix due to continued compressive forces leading to the densification phenomenon. An increase in densification stress with respect to strain for H20, H40, and H60 is observed up to the peak stress values of 34.51, 34.57, and 34.4 MPa, respectively. The amount of energy absorption signifies the toughness which is calculated by measuring the total area under the stress-strain curve. These toughness values for H, H20, H40, and H60 are measured as 11.26, 11.73, 11.84, and 12.61 MJ/m³ respectively. The total energy absorption of the H60 is 11.98 % more than HDPE. As the strength-to-weight ratio of composites has significant importance in its applications, specific foams' specific properties are presented in Table 4.2.

Table 4.2. Specific properties of plain and FGFs.

Composition	Specific modulus (MPa/kg/m ³)×10 ⁻³	Specific Yield strength (MPa/kg/m ³)×10 ⁻³
H	373.68	18.58
H20	403.02	19.29
H40	550.33	18.63
H60	661.94	20.79
FGF-1	443.62	17.55
FGF-2	512.15	22.31
FGF-3	435.78	15.30

Results revealed that foams exhibited better specific properties compared to H. The specific compressive modulus of the plain foams increases with an increasing GMB %. FGF - 2 and H60 exhibited the highest specific yield strength and modulus of 22.79 and 661.94 (MPa/kg/m³) ×10⁻³, respectively. FGFs exhibited a similar type of compression behavior to plain foams. The compression stress-strain plots and results of FGFs are presented in Figure 4.2c, and the results are listed in Table 4.1. Under initial compressive load, FGFs exhibited a linear elastic region and continued up to 0.1 mm/mm strain. The linear elastic region shifted to a nonlinear mode upon further loading. The compressive modulus and yield strength of FGF-2 are higher than FGF-1 and FGF-3. The compressive modulus of FGF-2 is 1.02 and 1.10 times that of FGF-1 and FGF-3, respectively. The yield strength of FGF-2 is 1.12 and 1.37 times that of FGF-1 and FGF-3, respectively. Among all the FGFs, the plateau region is distinguishable in FGF-2 Figure 4.2c due to comparatively more filler %, in-situ voids, and residual porosity. The Plateau region of FGF-1, FGF-2, and FGF-3 is observed at 18.78, 19.54, and 18.19 MPa. Energy absorption at 50% strain is higher for FGF-3 than other FGFs. Further, the increasing load increases the stress with lower strains due to the densification phenomenon. The toughness values of FGF-1, FGF-2, and FGF-3 are computed to be 12.25, 12.07, and 13.47 MJ/m³, respectively. Total Energy absorption of FGF-1, FGF-2, and FGF-3 are 8.79, 7.19 and 19.62 % more than plain HDPE. FGF-2 exhibited better specific properties among all functionally graded foams with specific modulus and strength values of 512.06 and

22.3 (MPa/kg/m³) × 10⁻³. Specific properties of FGF-3 are lower as compared to FGF-1 and FGF-2. Among all plain and FGFs, H60 has a higher modulus. The 3D printed H exhibited better yield strength with 1.08 and 1.03 times H20 and FGF-2. The energy absorption rate at 50 % strain is higher for printed FGFs than plain foams. The total energy absorption rate for FGF-3 is 1.06 times H60. Among all plain foams and FGFs, the highest plateau stress is observed for FGF-2 at 19.4 MPa. Improvement of yield strength and energy absorption rate with comparable modulus values in FGFs shows its potential for replacing pure H and plain foams in buoyancy-aided deep-sea naval applications.

4.1.1 Failure Mechanism

Failure of FGFs takes place in a layered fashion along the thickness direction when subjected to compressive load. With the increase in load, crushing gets initiated from the weaker layer with less strength and progresses toward the stronger layers. This type of failure, where weak layers fail first to protect stronger ones, is a sacrificial failure mechanism. In the present work, the failure of FGFs has undergone a similar type of behavior. When the compressive load is applied on the FGF-1, crushing is initiated at the H40, which has a compressive strength of 13.9 MPa, and propagated to H20, which exhibits a strength of 15.9 MPa protecting the HDPE, which has a strength of 17.23 MPa. This sacrificial phenomenon is presented in Figure 4.3a. A similar failure mechanism is observed in all FGFs Figure 4.3b. SEM analysis on compression-tested samples reveals that fillers act like flow barriers to the HDPE matrix Figure 4.4a. Higher compressive loads elongate the in-situ voids and residual micro-porosities, as seen in Figure 4.4b. The void-collapsing phenomena lead to higher energy absorption. All the GMBs in as printed samples of plain and FGFs are seen to be intact in Figure 4.5a, implying the chosen process parameters suitability. During compression, GMBs fracture due to intense particle interactions and is prominent at higher GMB contents (marked areas in Figure 4.5b). Particle-to-particle interactions intensify with higher compressive loads at much lower strain values and, subsequently more GMBs fracture. The layers also start to push against each other and eventually get mechanically merged, as seen in Figure 4.5c.

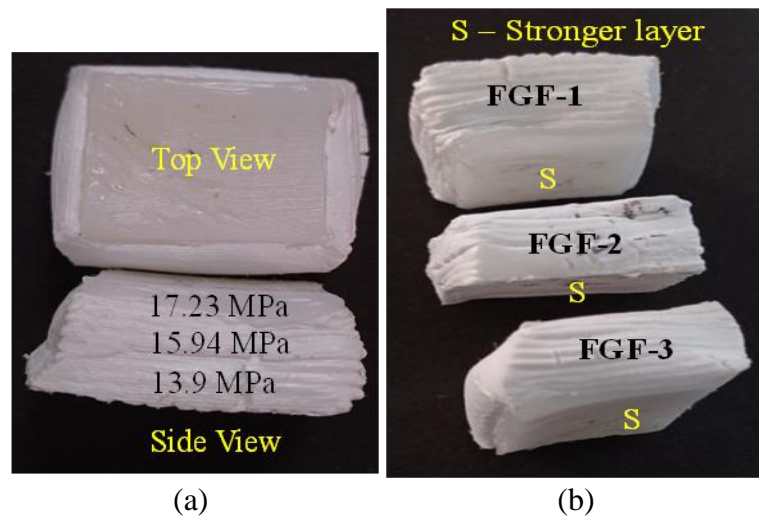


Figure 4.3. (a) Compressed representative FGF print (b) post tested FGFs.

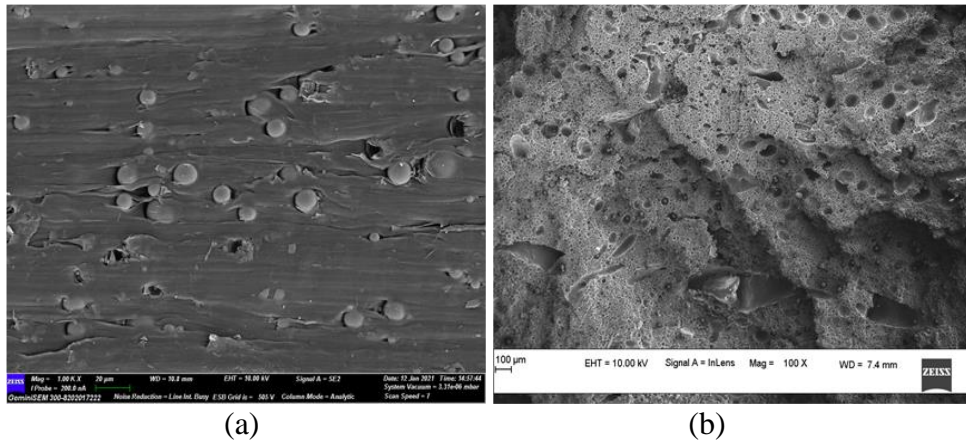


Figure 4.4. Representative freeze fractured 3D printed sample showing (a) material flow around GMBs and (b) void elongation and collapse during compression.

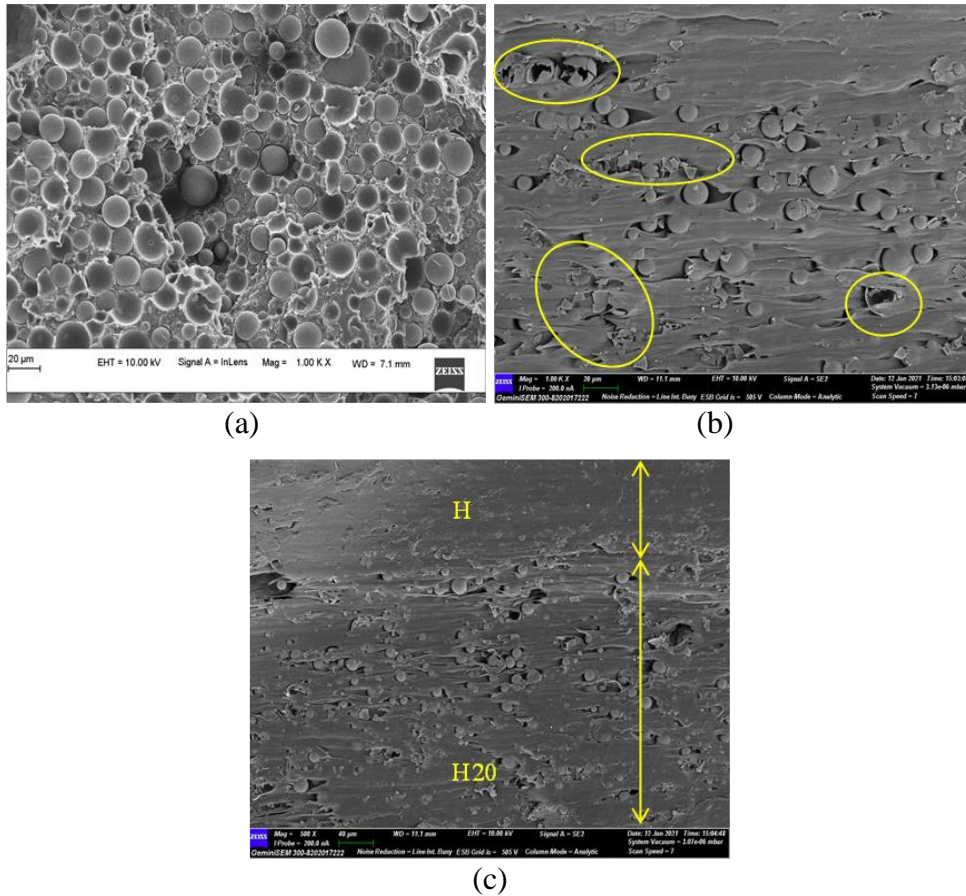


Figure 4.5. Representative of filler sustainability in (a) pre-tested and (b) post tested samples and (c) at the interface.

Failure of filler

In particulate composites, the deformation and failure are classified into three types, as shown in Figure 4.6a. They are (i) Fracture of the filler (hollow GMB), (ii) interface failure of filler and matrix, which is expressed as de-bonding, and (iii) dislodging of the filler. These failure occurrences in the sample are caused due to increase in the compressive load, which increases the inhomogeneity leading to the stress concentration. The stress concentration factor depends on the void geometry (MK. 1982, Pilkey Walter D et al. 2020). The inhomogeneity caused due to failure of the filler makes a sudden change in the space available for the matrix and other GMB debris to occupy, leading to the localized stress concentration (Figure 4.6b). GMBs failure under higher compressive loads leads to plastic flow of the matrix, aiding hollow space occupation. Further, it leads to particle-to-particle interaction resulting in the densification phenomenon.

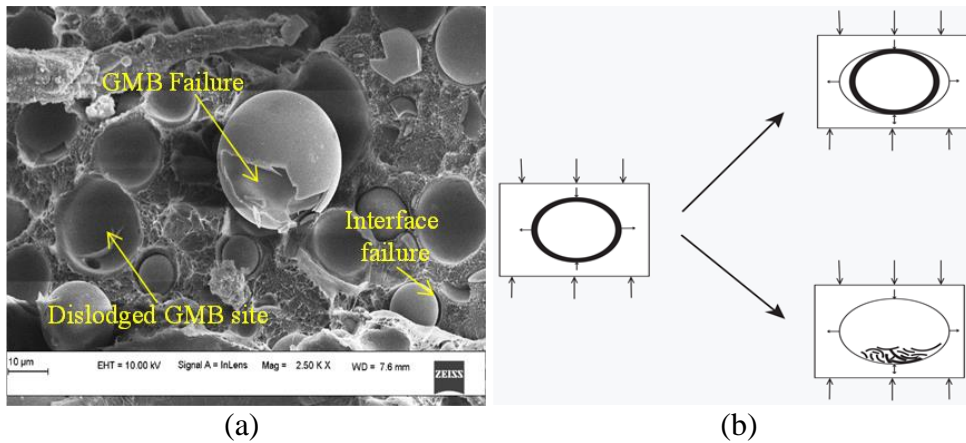


Figure 4.6 Representative (a) SEM of post-tested sample and (b) filler failure mechanism.

4.2 compressive behavior of functionally graded sandwich core

Functionally graded sandwich composites found their application in wide areas like buoyancy aided naval applications where these structures come across compressive forces. So studying the compressive response of these functionally graded sandwich foams is very important. So all three FGFSs are tested by applying the load at a cross-head displacement velocity of 0.5mm/min (Figure 4.7). From the experimental results, these foams exhibited three different phenomenon's similar to FGFs while deforming (Figure 4.8a). The SEM of post tested sample is shown in Figure 4.8b. FGFSs exhibited a similar type of sacrificial failure mechanism. Experimentally evaluated compressive properties of sandwich samples are mentioned in Table 4.3.

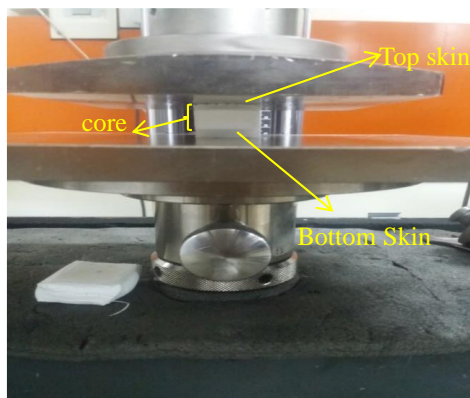


Figure 4.7. 3D printed FGSF-2 mounted in UTM.

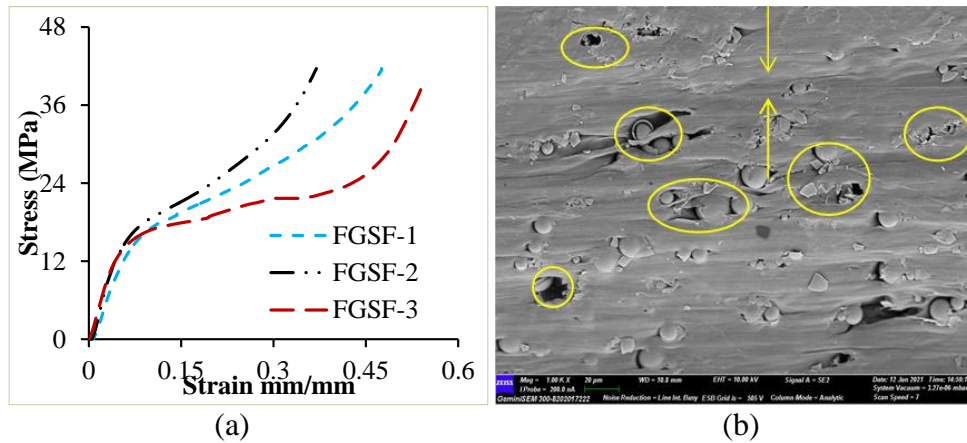


Figure 4.8. Compressive response (a) FGSFs and (b) Collapse of interface and filler.

Table 4.3 Compressive properties of FGSFs

Composition	Modulus (MPa)	Yield Strength (MPa)	Total Energy Absorption (MJ/m ³)	Specific Modulus (MPa/kg/m ³) × 10 ⁻³	Specific Yield Strength (MPa/kg/m ³) × 10 ⁻³
FGSF-1	369.15±7.31	16.22±0.83	14.02±0.59	455.71	19.08
FGSF-2	416.90±9.74	16.83±0.25	13.90±0.12	524.86	21.18
FGSF-3	395.74±4.04	12.9±1.07	16.13±0.85	465.57	15.92

Results show that among all FGSF's, FGSF-3 exhibited higher energy absorption and FGSF-2 exhibited higher modulus. This higher modulus of FGSF-2 is due to the presence of a higher GMB volume percentage. Specific results showed that among all FGSFs, FGSF-2 exhibited better specific strength and modulus. Comparative results of FGF and FGSFs showed that FGSFs outperformed their corresponding FGFs in terms of strength and modulus.

Conclusion

The compressive behavior of plain and functionally graded foams realized through 3DP is presented in this paper. The results are summarized as follows.

- Plain and FGFs are printed using suitable printing parameters, having seamless bonding between the layers and different compositions.
- The measured density of all 3D printed syntactic foams-based FGFs is less than HDPE, signifying that foams have good weight reduction potential. 3D printed

FGF-1, FGF-2, and FGF-3 have weight-saving potential of 9.22, 19.52, and 14.53 %.

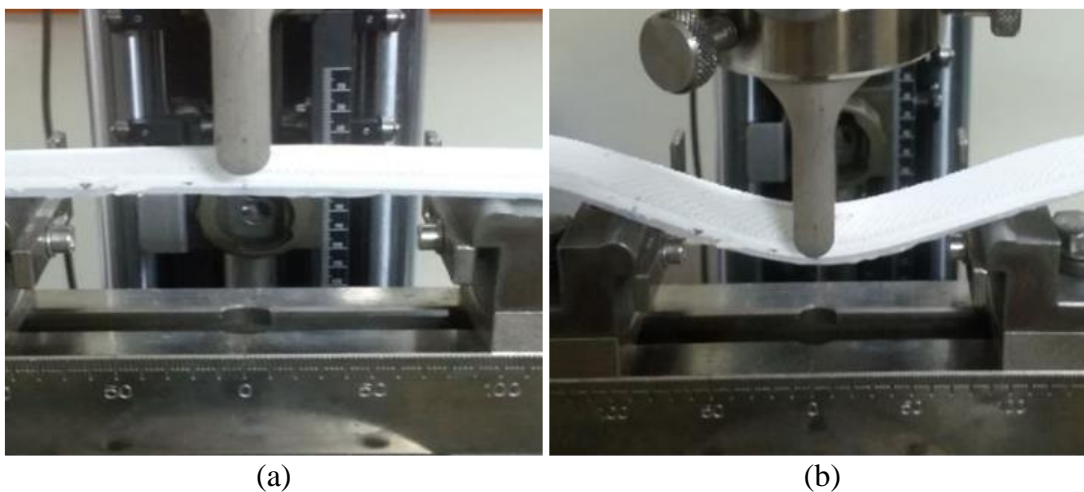
- The compressive modulus increased with GMB content in plain foams, and among FGFs, FGF-2 exhibited higher compressive modulus than FGF-1 and FGF-3.
- The yield strength of the plain foams decreases with an increase in filler volume %.
- Foams exhibited better specific properties compared to H. The specific modulus of H60 is 1.7 times that of pure HDPE. FGF-2 exhibited better specific strength than all 3D printed samples, which is 1.2 times of pure HDPE.
- FGFs exhibited better energy absorption than foams and is 8 to 19 % more than pure HDPE. FGF-3 exhibited the highest energy absorption rate at 50 % strain with 7.17 MJ/m³.
- Among all FGSFs, FGSF-3 exhibited better energy absorption potential. At the same time, FGSF-2 exhibited better specific properties.
- Comparison among all FGF and FGSFs' showed that FGSFs exhibited higher modulus and strength when compared with their respective cores.

Syntactic foams are mostly used in buoyancy aided and deep-sea applications where compressive properties play a crucial role. FGF and FGSFs with higher specific strength, design, and geometrical flexibility aided with integrated components (joint less - leak proof) possibility through 3D printing opens new avenues to design and manufacture complex parts for weight-sensitive applications.

5. FLEXURAL RESPONSE

Functionally graded foam beams are developed for weight-sensitive applications in aeronautical and naval sectors, where these structures are subjected to transverse loading conditions. Thereby, investigating the flexural response and failure mechanisms of 3D printed FGF, and FGFSF beams is of utmost importance. Three-point bending test is performed on all 3D printed FGF and FGFSFs to study their response toward transverse loading conditions (Figure 5.1a) as all the samples did not undergo fracture phenomenon. The bending test is performed until 10 % strain. Upon gradual increase in load with respect to time, the sample initiated with elastic behavior and continued to reach its yield zone, as seen in Figure 5.1b. With further increase in load, FGF-2 and FGFSF-2 exhibited crack initiation and subsequent propagation. In contrast, the remaining samples of FGF and FGFSF did not exhibit any crack initiation even at a higher deformation state, as seen in Figure 5.1c and Figure 5.1d.

The semi-crystalline HDPE gets melted and cools slowly onto the build platform in the 3DP process. During the process of cooling, HDPE undergoes the phenomenon of contraction well within limits leading to the tight packing of GMBs. Further, cooling naturally on the build platform induces circumferential compressive stresses. These induced stresses increase the HDPE matrix's yield phenomenon and arrests crack propagation.



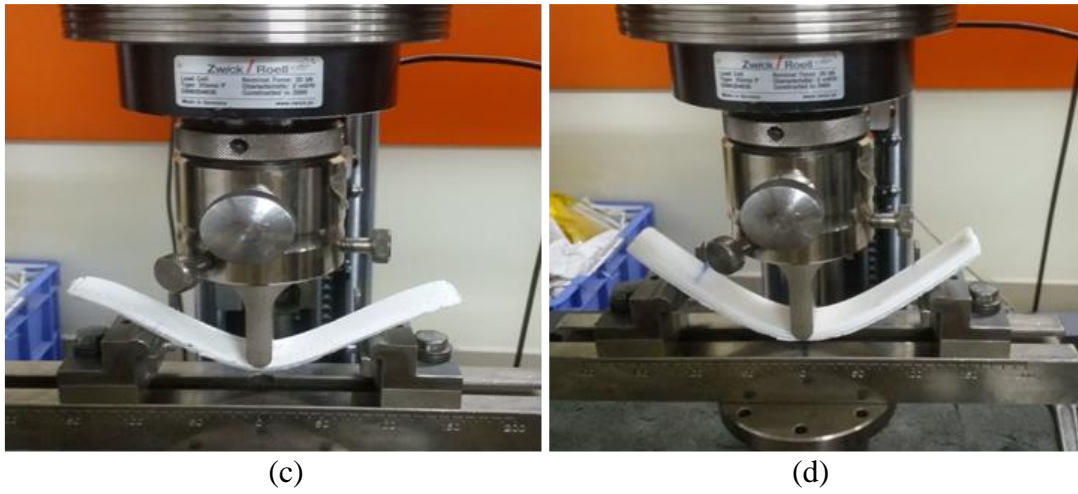


Figure 5.1. Three Point bending test of FGF-3 (a) Initial mounting on fixtures (b) post yield zone (c) Sever deformation (d) FGsf-3 sever deformation.

5.1 Flexural response of FGFs

5.1.1 Experimental Results

In the current work, all FGFs are tested at the rate of 2.54 mm/min. Representative stress versus strain graphs of FGFs are depicted in Figure 5.2 and experimentally obtained modulus and strength are listed in Table 5.1.

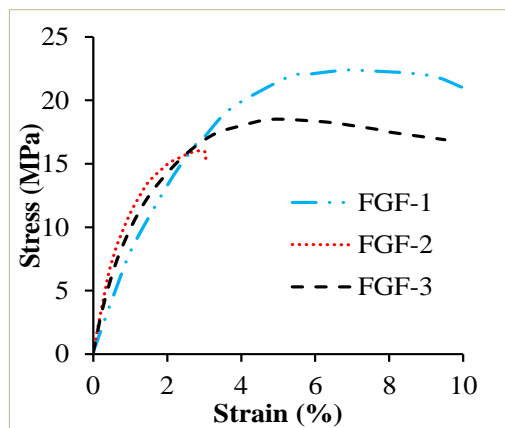


Figure 5.2. Stress-Strain response of 3D printed FGFs.

Table 5.1. Density and Flexural Properties of FGFs.

Density (kg/m ³)	FGF type	Configuration (Bottom to upper side)	Flexural Modulus (MPa)	Flexural Strength (MPa)
841.56±11	FGF-1	H-H20-H40	1185±12.41	22.6±1.7
746.89±14	FGF-2	H20-H40-H60	1325±9.71	16.1±0.9
792.24±10	FGF-3	H-H20-H40-H60	1278±13.02	17.9±1.4

The results show that FGF-2 showed higher modulus and lower strength. A higher volume fraction of reinforced GMB in FGF-2 made it stiffer than other FGFs. This higher stiffness is the primary reason which leads FGF-2 to exhibit brittle fracture. The modulus of FGF-2 is 1.03 and 1.11 times that of FGF-3 and FGF-1. Across all FGFs, FGF-1 exhibited better strength due to lower in-situ micro porosity embedment during different processing stages. From the experimental results, it is observed that with an increase in the GMB volume percentage, the modulus of the graded foams increased with comparable strength. There are two reasons for observing the decreasing trend of strength with an increase in filler. 1) As in the composite, the filler particles take place a significant role in load-bearing. A weak interface between the filler and matrix leads to an improper transformation of subjected load from matrix to filler, which minimizes the material systems strength 2) Increase in void percentage with an increase in the filler volume fraction. Once the sample reaches the yield zone, crossing its elastic limit, the porosity formed between raster due to layered printing acts as the catalyst for stress drop and subsequent sample failure. As the effect of these two phenomena is comparatively less in FGF-1, it exhibited better strength than others, compromising rigidity and weight-saving potential. The flexural strengths of FGF-1 are 1.26 and 1.40 times that of FGF-3 and FGF-2. The specific properties like strength and modulus of FGFs are crucial for weight sensitive application. The specific properties of these respective FGFs are mentioned in Table 5.2. From the results, it is observed that FGF-2 exhibited better specific properties. This is due to the presence of a higher volume percentage of GMB.

Table 5.2. Specific Properties of FGFs.

FGF Type	Specific modulus (MPa/kg/m ³) × 10 ⁻³	Specific strength (MPa/kg/m ³) × 10 ⁻³
FGF-1	1408.099	26.85
FGF-2	1774.022	21.556
FGF-3	1613.14	22.59

5.1.2 Finite Element Analysis of Flexural response

FE analysis showed that stress on the top layer subjected to compressive force is higher than the bottom layer under tensile force Figure 5.3. The one possibility for

such an unsymmetrical stress distribution along the thickness direction is the presence of a neutral axis near the top layer (Table 5.3). The deviations between FEA and experimental values increase with filler content (Table 5.4). This might be due to geometric inhomogeneities like porosity, interface de-bonding between the constituent materials, and the isometric material property assumptions. Moreover, the deformation values mentioned in the current paper are the average values of a complete set of samples tested for each configuration. If the comparisons are estimated corresponding to the highest deformation sample, this deviation is noted to be 5-15 %.

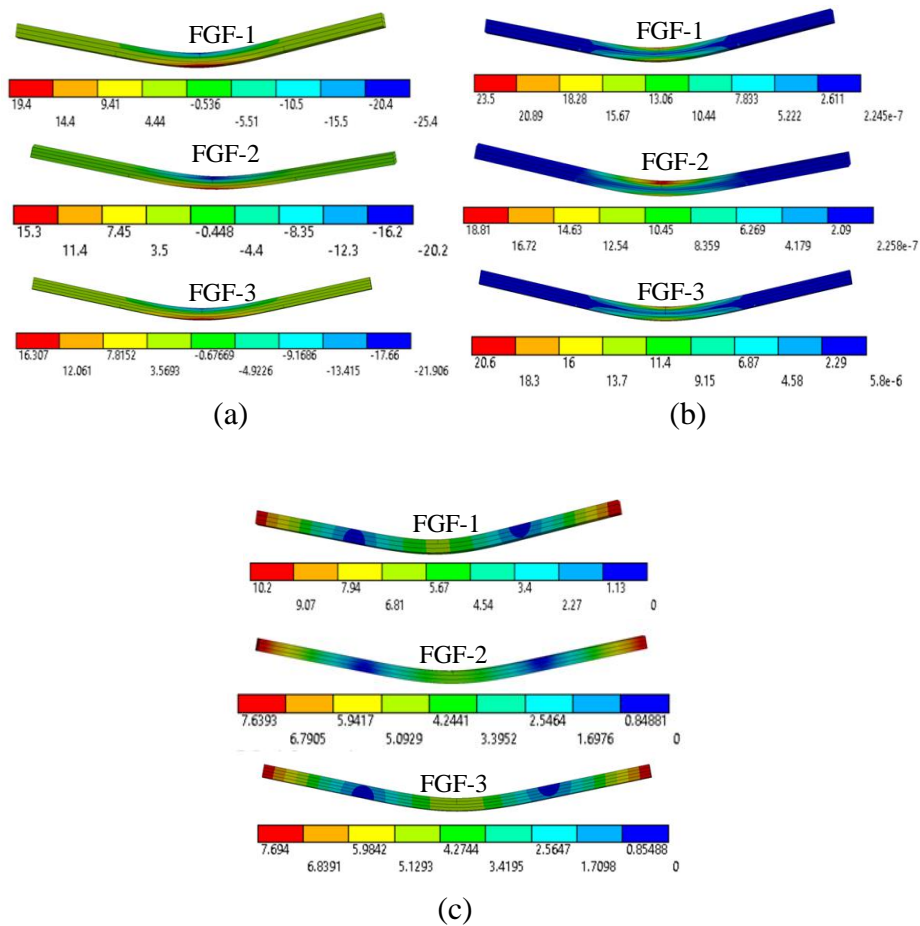


Figure 5.3. FEA results of FGFs (a) stress distribution in X-axis (b) Von-misses stress and (c) deformation.

Table 5.3. Position of neutral axis.

Sample Type	Centroid axis position (mm)	Neutral axis position (mm)	% Deviation of neutral axis from centroid axis (%)
FGF-1	3	3.226	7.53
FGF-2	3	3.209	6.96
FGF-3	3	3.267	8.90

Table 5.4. Experimental and FEA comparison of graded foams.

Sample Type	Stress (MPa)		Error (%)	Deflection (mm)		Error (%)
	Experimental	FEA		Experimental	FEA	
FGF-1	22.60	22.662	0.27	4.88	5.86	16.72
FGF-2	16.1	18.75	14.13	3.11	4.37	28.83
FGF-3	17.9	19.58	8.58	3.58	4.83	25.87

5.2 Flexural response of FGFSF

5.2.1 Experimental Results

With the aim of controlling the rate of stress drop and delaying the failure probability of crack initiation from the bottom-most tensile layers under transverse load, FGFSFs are 3D printed all at once. These FGFSFs are realized by sandwiching FGF core in 3D printed HDPE skin. A three-point bending test for FGFSFs is performed at a 3.41 mm/min loading rate. Results acquired through experimental investigation are presented in Table 5.5. The results show that FGFSFs exhibited superior strength compared to their respective FGFs, which shows sandwiches' significance in improving the beams' strength. Experimental responses of stress versus strain for respective FGFSFs are depicted in Figure 5.4. This plot shows that FGFSFs exhibited similar behavior to core with comparatively higher yield strength. FGFSF-2 exhibited rigid behavior compared to FGFSF-1 and FGFSF-3. FGFSF-2 exhibited a higher flexural modulus of 1.23 and 1.19 times that of FGFSF-1 and FGFSF-3. FGFSF-1 exhibited higher strength of 1.15 and 1.06 times than FGFSF-2 and FGFSF-3. Even at higher deformation conditions, there is no observable macroscopic crack initiation in FGFSF-1 and FGFSF-3 (Figure 5.1d). Figure 5.1d also exhibits the absence of delamination failure at the skin and core interface, even at the higher deformation stages.

Table 5.5. Experimental flexural properties of FGSFs’.

Density (kg/m ³)	FSGF Type	Configuration (Bottom to upper side)	Flexural Modulus (MPa)	Flexural Strength (MPa)
850 ± 09	FGSF-1	H-H-H20-H40-H	910.5±8.20	24.1±0.67
794 ± 13	FGSF-2	H-H20-H40-H60-H	1120±11.53	20.9±0.43
810 ± 07	FGSF-3	H-H-H20-H40-H60-H	935±13.14	22.54±1.10

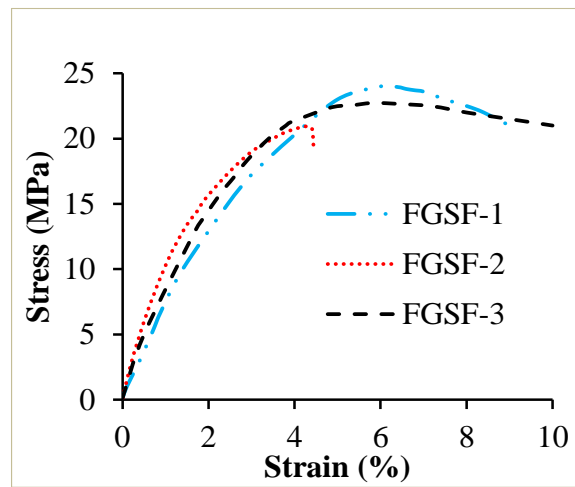


Figure 5.4. Stress-Strain response of 3D printed FGSFs’.

The above observations indicate that developing sandwich structures all at once through 3D printing and with gradual variation of properties along the core helps overcome the most probable delamination defects in sandwiches processed through traditional methods. Further, specific properties are crucial in showing their significance in weight-sensitive applications. Hence, the specific properties FGSFs are listed in Table 5.6.

Table 5.6. Specific properties of FGSFs’.

FSGF Type	Specific modulus (MPa/kg/m ³) × 10 ⁻³	Specific strength (MPa/kg/m ³) × 10 ⁻³
FGSF-1	1071.176	28.352
FGSF-2	1410.046	26.322
FGSF-3	1154.320	27.827

5.2.2 Finite Element Analysis of Flexural response

FE analysis showed that stress on the top layer subjected to compressive force is higher than the bottom layer under tensile force (Figure 5.5 a). The one possibility for such an unsymmetrical stress distribution along the thickness direction is the presence of a neutral axis near the top layer Table 5.7. The deviations between FEA and experimental values increase with filler content (Table 5.8). This might be due to geometric inhomogeneities like porosity and interface de-bonding between the constituent materials and the isometric material property assumptions. Moreover, the deformation values mentioned in the current paper are the average values of a complete set of samples tested for each configuration. If the comparisons are estimated corresponding to the highest deformation sample, this deviation is noted to be 5-15 %.

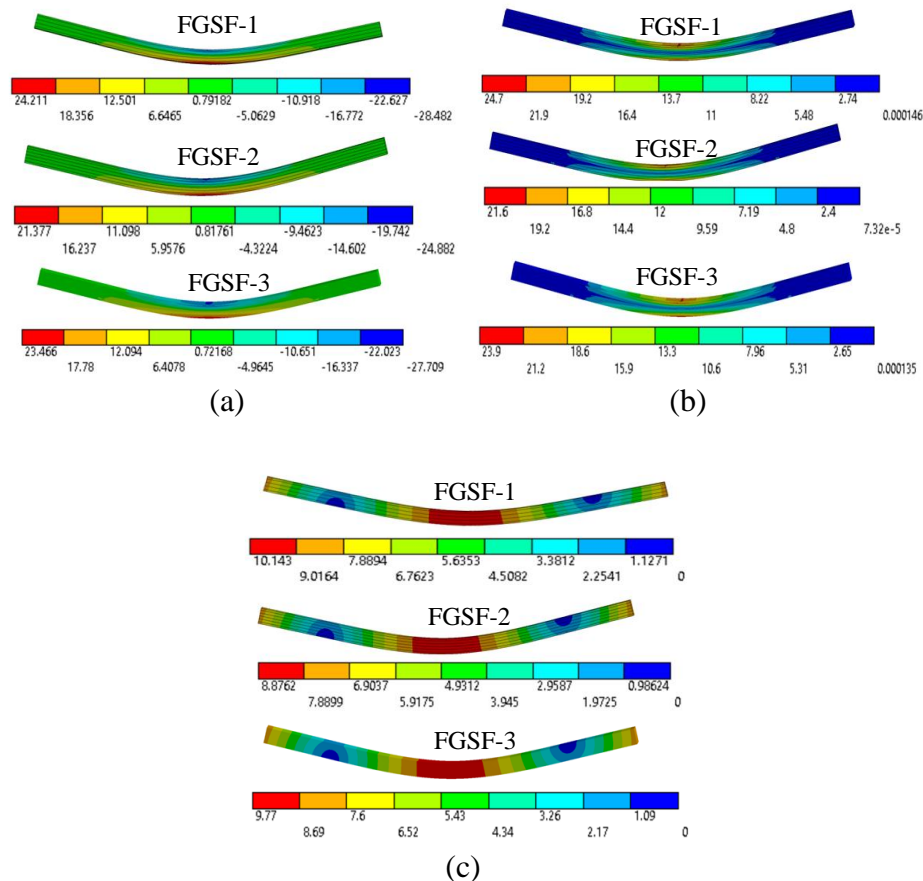


Figure 5.5. FEA results of FGFSs (a) stress distribution in X-axis (b) Von-mises stress and (c) deformation.

Table 5.7. Neutral axis position in FGSFs’.

Sample Type	Centroid axis position (mm)	Neutral axis position (mm)	% Deviation of neutral axis from centroid axis (%)
FGSF-1	4	4.142	3.55
FGSF-2	4	4.140	3.50
FGSF-3	4	4.066	1.65

Table 5.8. Experimental and FEA comparison of FGSFs’.

Sample Type	Stress (MPa)		Error (%)	Deflection (mm)		Error (%)
	Experimental	FEA		Experimental	FEA	
FGSF-1	24.1	24.30	0.82	9.03	10.15	11.03
FGSF-2	20.9	19.75	5.50	6.36	8.27	23.09
FGSF-3	22.54	21.99	2.44	8.22	8.88	7.43

5.2.3 Failure Mechanism of FGSFs

The most probable failure mechanisms observed in sandwich structures are delamination at the skin and core interface, core shear, indentation, and face wrinkling/micro buckling (Lingaiah K and BG. 1991, Triantafillou Thanasis Christos and J. 1987). The type of failure depends on the skin geometries and strength, processing method, and core materials composition (Triantafillou Thanasis Christos and J. 1987). Among these failure possibilities, even at higher loading conditions, delamination at the skin and core interface is not observed in the present work, as seen in Figure 5.1d. This is due to the formation of seamless bonding and properly fused skin and core layers owing to the suitability of the printing parameters. During flexural loading, the bottom skin undergoes tensile stresses, while the top skin is subjected to compressive stresses. An indentation on the top skin at the point of contact with the wedge is observed. This might be due to the applied load on the sample reaching beyond the compressive yield strength of the skin. Among all the tested samples, shear failure is observed only in FGSF-2 (Figure 5.6), whereas it was absent in FGSF-1 and FGSF-3.

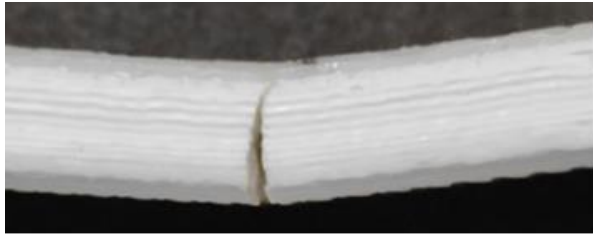


Figure 5.6. Fractured FGSF-2.

5.3 Comparison of FGF and FGSFs

The driving force for developing the graded foam cored sandwiches over plain cored sandwich composites is the elimination of sharp transition of stiffness and thermal properties at the skin and core interface. Initially, functionally graded foam cores are developed and tested to study their flexural response, and then their respective sandwiches are developed and investigated further. The respective properties of the plain core and their corresponding sandwiches are referred from previously published works on foams for comparing graded foams with plain foams (Bharath HS et al. 2021). A comparative study shows that the flexural modulus of FGFs increased in the range of 19.6 to 33.83 % higher than pure HDPE. The flexural strength of FGF-1 is comparable with HDPE, whereas it is 49.66 % higher than H60. Compared to plain sandwiches, graded compositions exhibited 10.5 to 22.1 % higher strength. Smooth variation of properties helps eliminate the deleterious effects like thermal expansion mismatch while processing and sharp stiffness transition at the interface of skin and core when subjected to mechanical loadings. The above two mentioned phenomena significantly control the shear stresses and enhance the strength of the 3D printed graded foams. FGF and FGSF showed that FGF-2 and FGSF-2 exhibited higher specific modulus compared to their other respective configurations. Among FGF and FGSFs, FGFs exhibited higher specific modulus than their corresponding sandwiches (Figure 5.7a). From the specific strength perspective, FGSFs show superior behavior compared to their respective FGFs, as seen in Figure 5.7b.

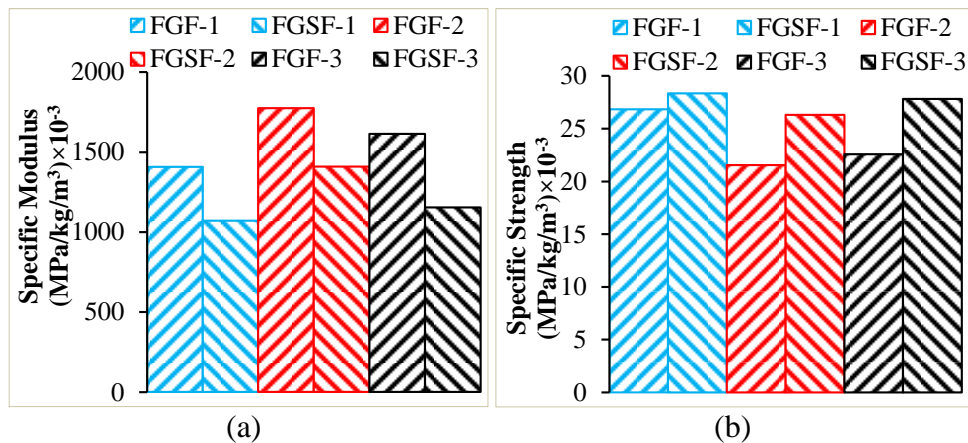
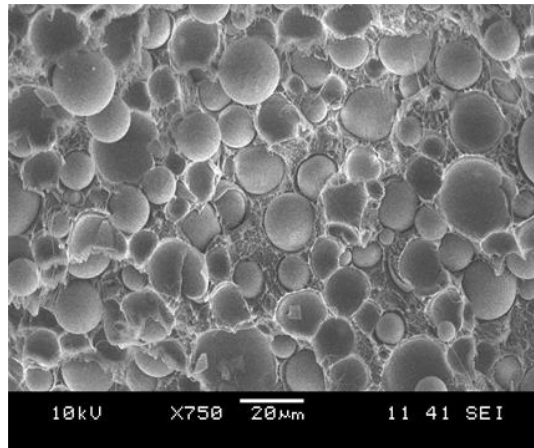


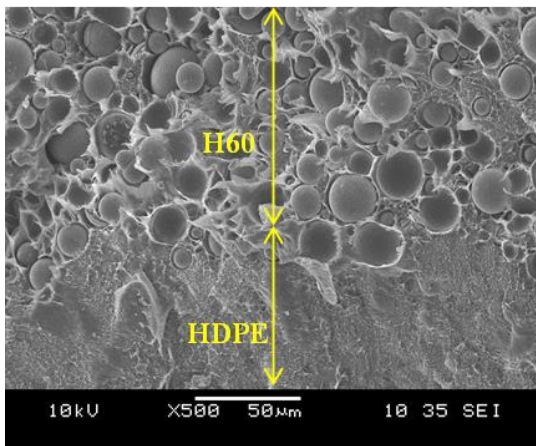
Figure 5.7. Comparison of FGF and FGSF (a) Specific modulus and (b) specific strength.

5.4 Micrographic analysis

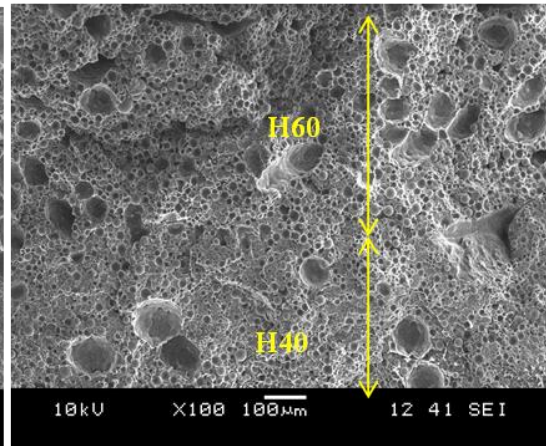
Filler sustainability and interface bonding are observed using SEM analysis on freeze fractured 3D printed graded foams (Figure 5.8). It's clearly evident from the micrographs that no filler breakage evidently implies the suitability of the chosen processing parameters at all three stages of blending, extrusion, and 3DP. The seamless interface between the HDPE skin and foamed core (H60) and within the core (H60/H40) is shown in Figure 5.8b and Figure 5.8c. This is due to the proper fusion of one layer with another, which signifies the appropriate deposition rate. This seamless bonding helps in effective load transfer from one material layer to another. Moreover, adequate bonding signifies bond strength. Interlaminar delamination is absent, which might creep in owing to the higher stresses caused due to the applied load at the interface of layers than the bond strength. Lower bonding strength results in delamination or cracks propagation along the longitudinal direction at the interfaces, which is not seen for the proposed methodology of 3DP of FGSFs. Only type-2 of FGF and FGSFs underwent fracture among all the printed samples. SEM analysis at the fractured cross-section showed that due to induced tensile and compressive stresses in the layers below and above the neutral axis, one layer is diffused into the other more firmly exhibiting yielding phenomenon of HDPE during crack propagation leading to the polymer fibre elongation Figure 5.8d. Filler failure is not observed. Nevertheless, GMBs are observed to be de-bonded from the HDPE matrix (Figure 5.8e), which is very much anticipated as both, the HDPE and GMBs are used without any surface modifications.



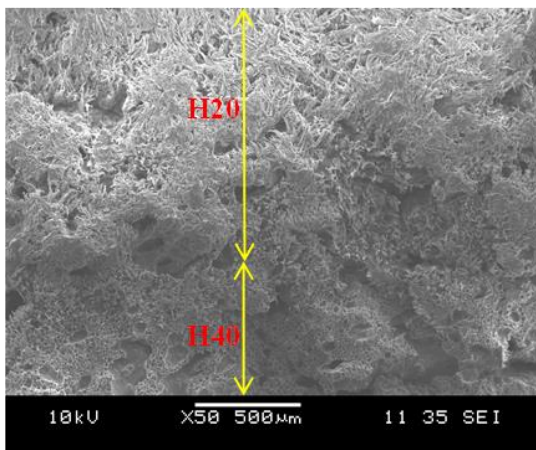
(a)



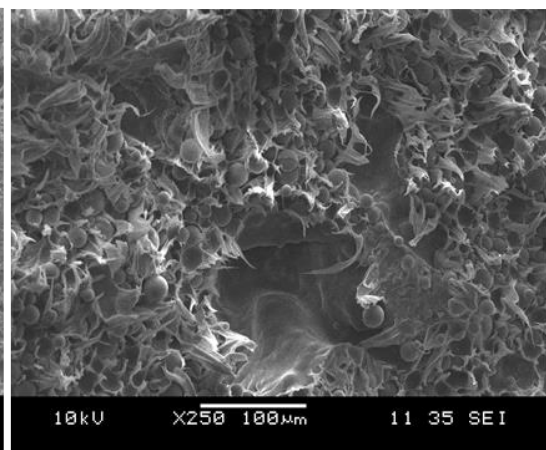
(b)



(c)



(d)



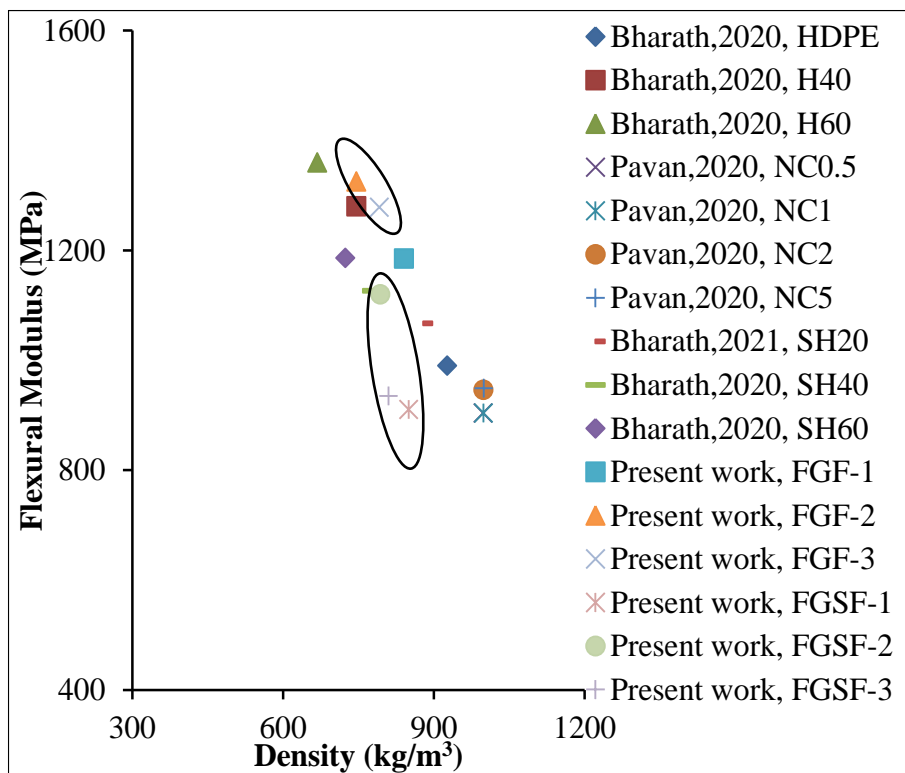
(e)

Figure 5.8. SEM of graded foams (a) GMB sustainability (b) HDPE and core interface (c) interface among (d) layer diffusion at fractured cross section and (e) de-bonding.

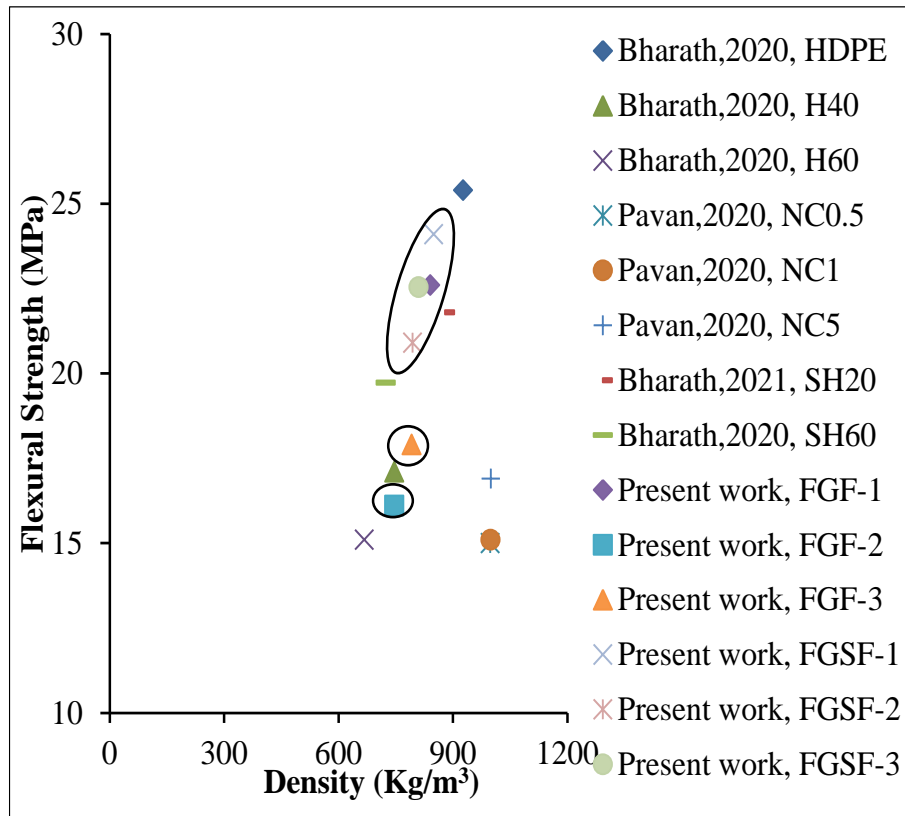
5.5 Property Chart

The property chart compares flexural properties as a function of the density of the developed composite. The properties of FGF and FGFSs are compared with plain

composites of similar and dissimilar materials developed using the 3D printing process (Beesetty Pavan et al. 2020, Bharath H. S et al. 2021). Comparative results showed that, apart from the H60, FGF-2 exhibited a better modulus value than others and is nearer to H40 values (Figure 5.9a). The strengths of the FGF-2 are higher than H60 and H40. From the strength point of view, FGFSs exhibited superior response compared to other materials, as seen in Figure 5.9b. With comparable modulus and density, better strength is observed in the graded foams.



(a)



(b)

Figure 5.9. Property chart (a) flexural modulus and (b) flexural strength.

Conclusion

- FGSFs exhibited better strength compared to FGFs. Among all samples, FGF-2 exhibited the highest modulus.
- Modulus of FGF-2 enhanced by 33.83% compared to pure HDPE.
- All at once, 3D printed FGSFs exhibited better strength compared to non-graded foams.
- FGFs exhibited higher specific modulus than their corresponding sandwiches
- FGSFs exhibited higher specific strength than their corresponding cores
- Due to material property gradation, the asymmetric stress distribution is observed along the thickness direction.
- No delamination is observed, even at higher deformations.
- Only type-2 of FGF and FGSFs underwent fracture among all the printed samples.

6. VIBRATION BEHAVIOUR

6.1 Buckling and free vibration of functionally graded core under axial compression

An SEM image of the 3D printed graded foams is shown in the figure. From Figure 6.1a, it is observed that layers are properly fused without any delamination. The freeze-fractured cross-section at the interface of the HDPE and foam is shown in Figure 6.1b. From this, it is observed that even the interface between the dissimilar compositions was properly fused, and there is no observable filler failure in the sample (Figure 6.1c).

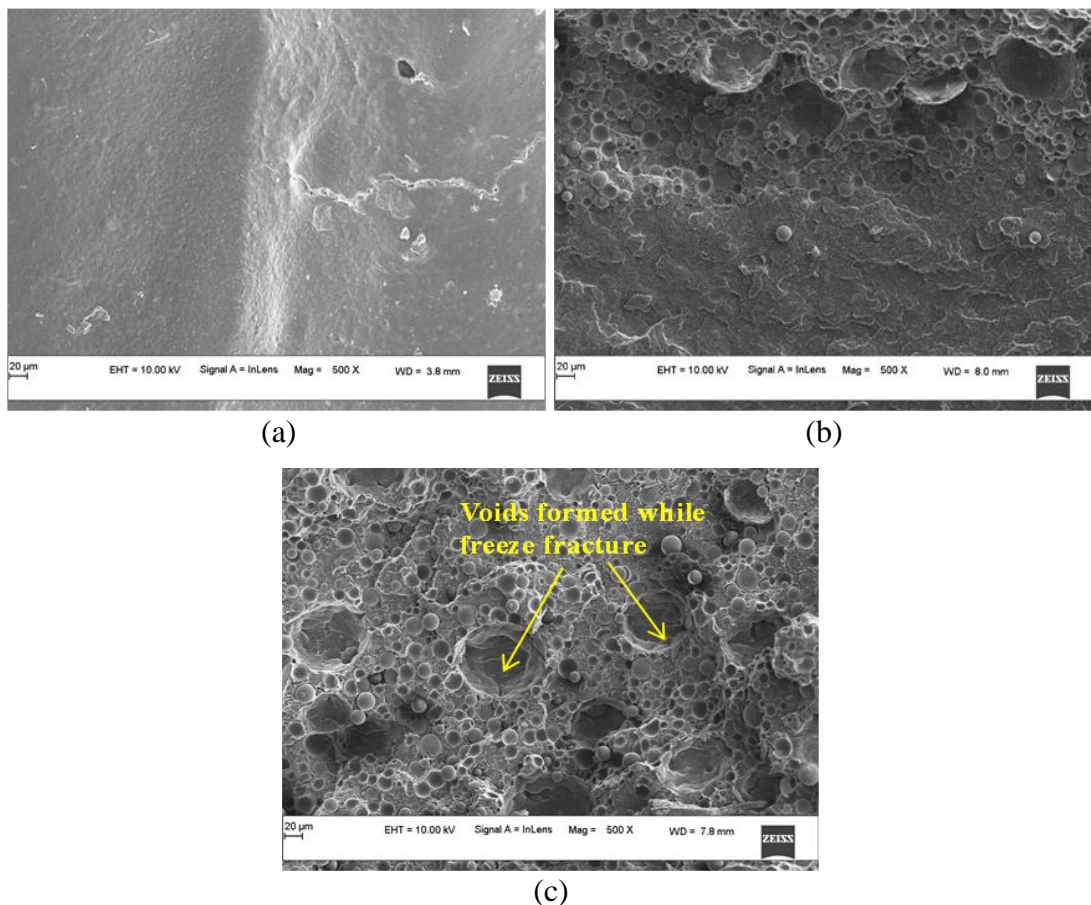


Figure 6.1. (a) seamless deposition between two adjacent layers (b) interface between H and H20 in 3D printed FGF – 1 and (c) GMB sustainability.

6.1.1 Buckling behaviour of FGFs.

3D printed FGFs are subjected to axial compressive force under clamped-clamped conditions using UTM. Compressive force on the sample is slowly increased by moving the upper fixture at 0.2 mm/min. The process continued until the sample

underwent the buckling phenomenon. Once the load and deflection curve in the DAQ is observed to be stabilized by a steady rise in deflection at constant load, the test is terminated. All FGFs are subjected to the buckling test and exhibited global buckling with a maximum deflection at the center and zero deviations at the fixed supports. The typical pre and post-buckling regions of FGF-2 are shown in Figure 6.2. No delamination between the layers is observed in the buckled sample, which signifies that all samples are printed with apt parameters having a very good bonding between the graded layers. The experimentally acquired load-deflection graph for HDPE and FGFs is presented in Figure 6.3.

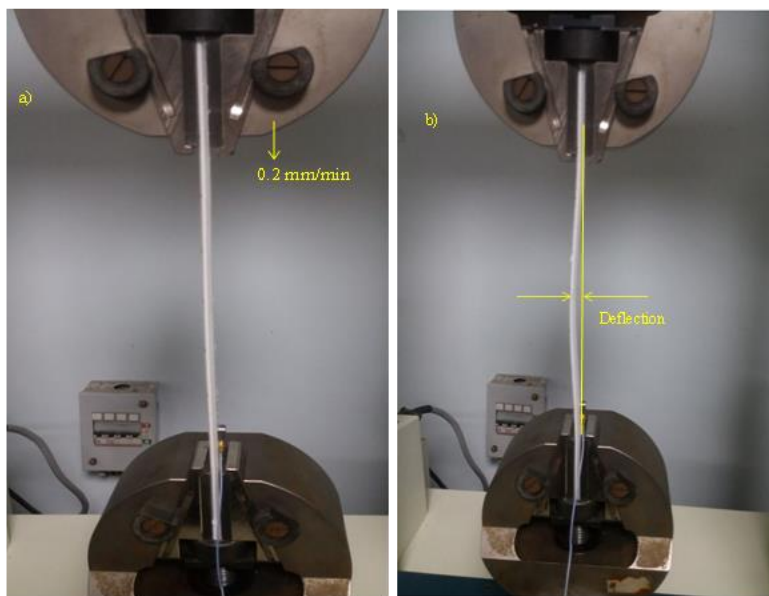


Figure 6.2. Representative FGF in (a) pre and (b) post buckling regimes.

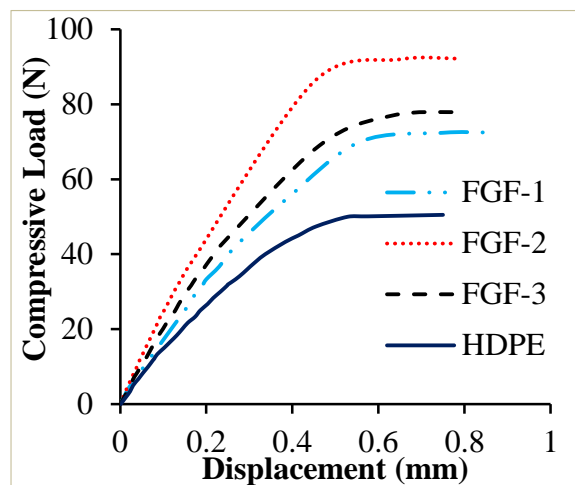


Figure 6.3. load and deflection graph of HDPE and FGFs'.

P_{cr} of FGFs is evaluated from load and deflection curve using MBC and DTM methods. Figure 6.4 shows the graphically evaluated P_{cr} of representative FGF-2. Critical buckling load of FGFs calculated using experimental and numerical analysis is listed in Table 6.1.

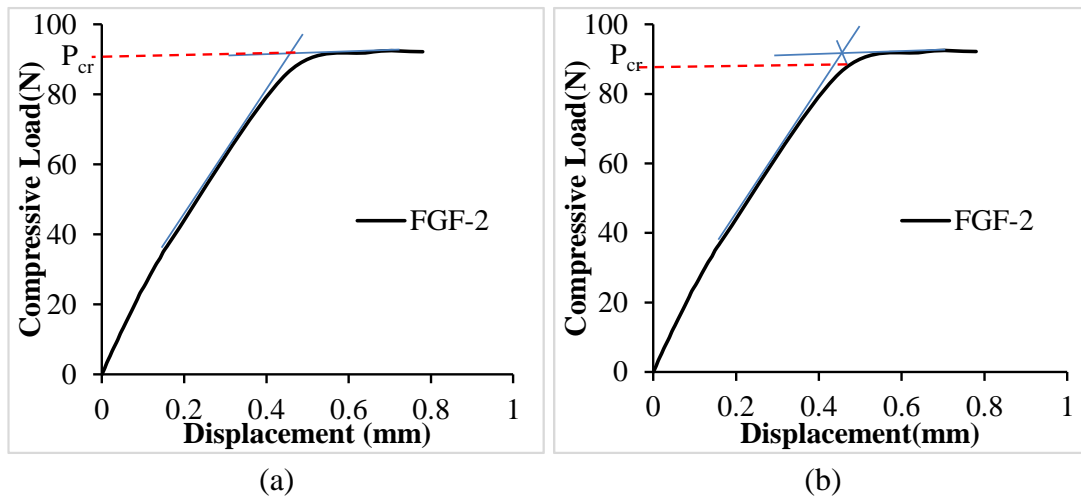


Figure 6.4. Representative load and deflection graph for evaluating P_{cr} using (a) DTM and (b) MBC method.

Table 6.1. Experimental and numerical P_{cr} of FGFs’.

Material	Experimental P_{cr} (N)		Numerical P_{cr} (N)		% Deviation of experimental with respect to numerical	
	DTM	MBC	DTM	MBC	DTM	MBC
FGF-1	71±2.76	68±1.90	72	69.5	1.38	2.17
FGF-2	91±1.53	88±1.64	95	91.0	4.21	3.29
FGF-3	75±2.27	72±1.83	76	73.5	1.35	2.04

Adding hollow GMB particles as the filler having higher moduli than HDPE helps improve the stiffness. This increase in stiffness makes FGFs exhibit higher buckling strength compared to H. Compared to pure HDPE, the buckling strength of FGF-1, FGF-2, and FGF-3 calculated using DTM and MBC methods increased by 39, 78.4, 47 %, and 44.68, respectively, 87.23, 53.19 %. Among all FGFs, FGF-2 exhibited the highest buckling strength of 91 and 88 N, as computed by graphical DTM and MBC methods. P_{cr} of FGF-3 is higher compared to FGF-1 and lower than FGF-2. A similar trend is also observed for P_{cr} evaluated using numerical analysis. Moreover, it is observed that P_{cr} of FGFs calculated using numerical analysis exhibited slightly

higher values than experimental values. This deviation is observed to be 1 to 4.5 % for both DTM and MBC methods. There are three possible reasons for this deviation (i) residual micro-porosities though such in-situ voids help in increasing the weight reduction potential, (ii) assumption of quasi-isotropic response, and (iii) assumed GIF value in the numerical estimation. In the present work, GIF is varied in the range of 0.0001 to 0.001. It is observed that the load and deflection result of numerical analysis matches with experimental results with GIF of 0.0008, 0.0004, and 0.0008 for FGF-1, FGF-2, and FGF-3, respectively (Figure 6.5).

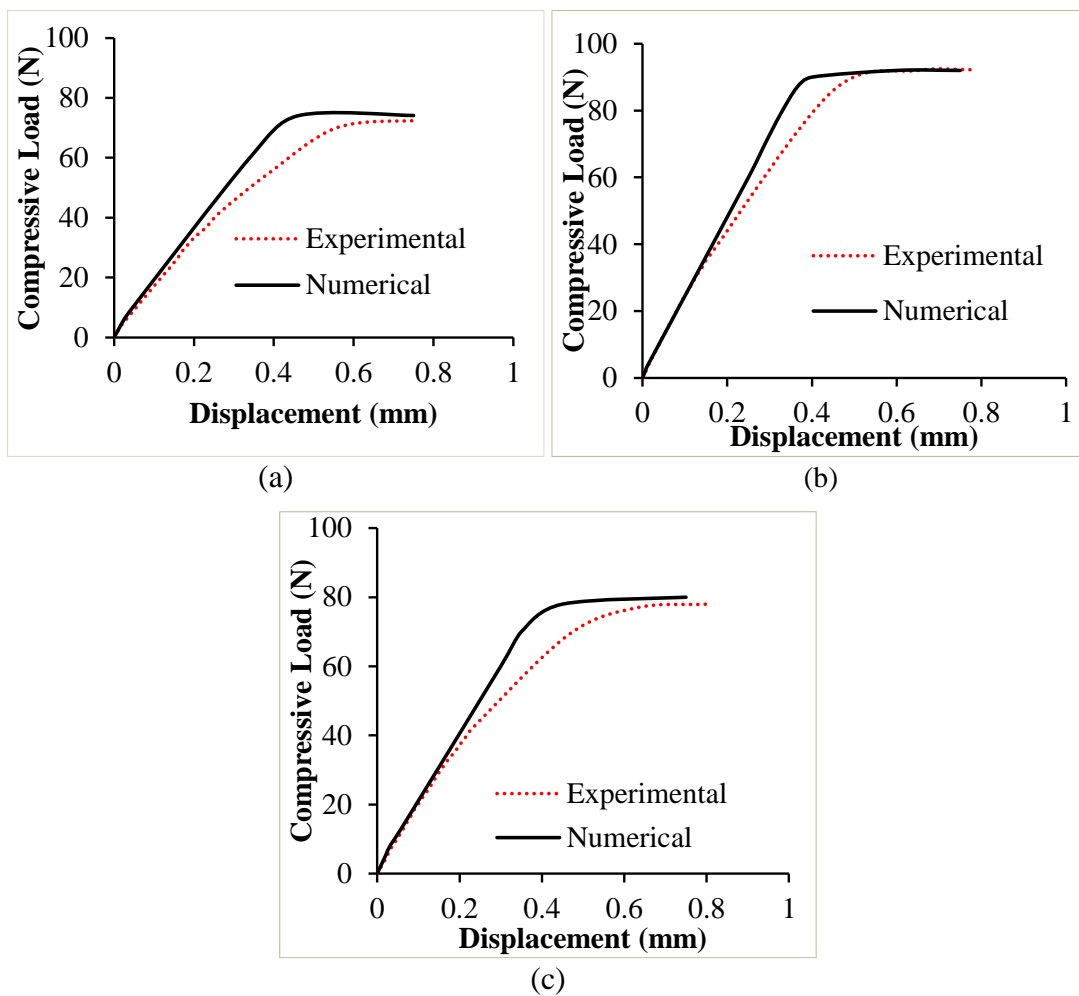


Figure 6.5. Load-deflection comparison of (a) FGF-1 (b) FGF-2 and (c) FGF-3.

Comparative studies of P_{cr} calculated using DTM and MBC reveal that the DTM method overestimated 6 to 7 % higher P_{cr} than MBC. P_{cr} As mentioned earlier, calculations using DTM and MBC are considered upper and lower boundary limits. Furthermore, a comparison of the plain SF with FGFs reveals that P_{cr} of FGF-2 are 1.75, 1.33, and 1.05 times and FGF-1 is 1.36, 1.04, and 0.82 times higher than their

respective SF compositions. Smooth variation of properties along thickness direction and presence of higher GMB vol. % made the FGF-2 withstand a higher uniaxial compressive load for the same deflection than FGF-1 and FGF-3, which is observed in experimentally obtained load-deflection graphs (Figure 6.3). Figure 6.6 shows that the variation in modulus is smooth for FGF-3 compared to FGF-1 and FGF-2. However, the variation in modulus for FGF-3 is more asymmetric than FGF-2. Due to this reason, the effective bending stiffness of FGF-2 is better than FGF-3, which reflects in the enhancement of buckling and frequencies of FGF-2 beams. By all the above observations, it is concluded that FGF-2 has higher stiffness among all FGF beams. Moreover, gradual variation of micro-porosity helps control the stresses induced in the beam under loading conditions, favoring the sample to inhibit its deflection rate. This phenomenon is absent in plain foams, which made 3DP FGFs exhibit superior properties compared to plain SFs. This shows the potential of FGFs in replacing plain beams for weight-sensitive structural applications.

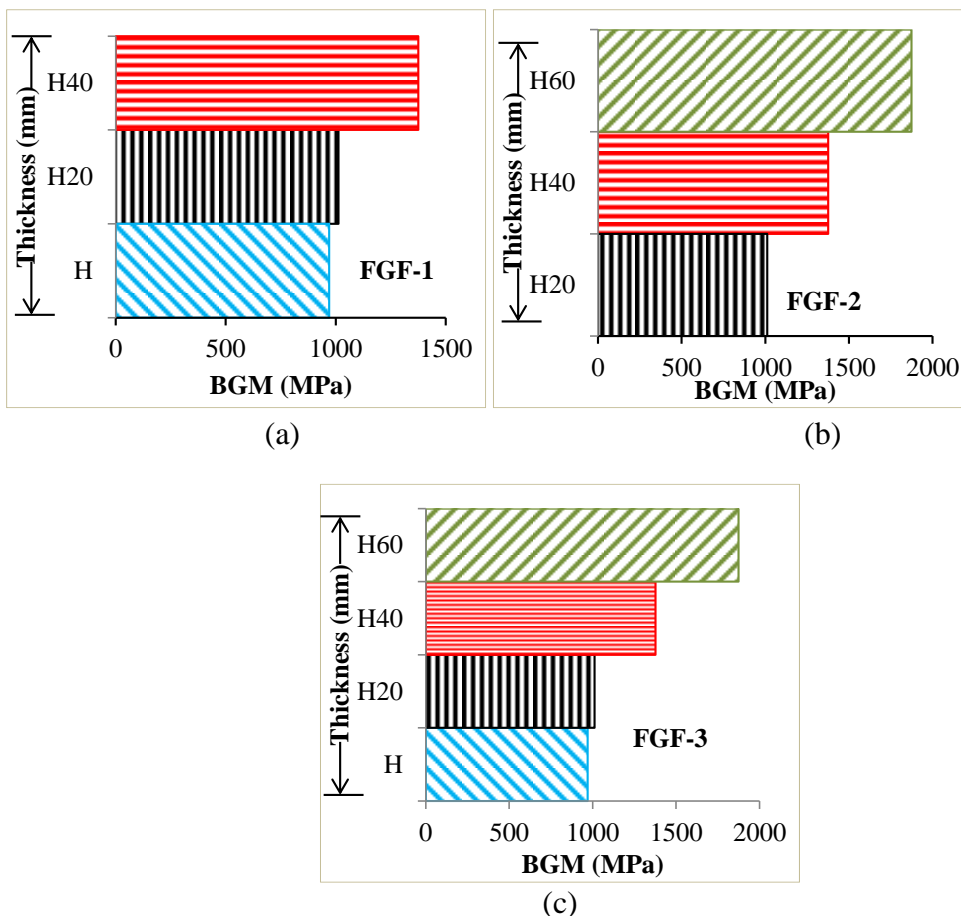


Figure 6.6. FGFs Vs variation of Bardella-Genna modulus along the thickness of (a)FGF-1 (b)FGF-2 and (c)FGF-3.

6.1.2 Free Vibration

FGFs are investigated for free vibration under uniaxial compressive load. FGFs are marked with eight points (Figure 2.13) by maintaining a constant distance between two consecutive points. The sample is excited at each marked point using a roving impact hammer, and the corresponding FRF is measured using an accelerometer. The typical FRF of the FGF-2 sample is shown in Figure 6.7a. Natural frequencies with respect to the first three modes are computed using DEWESoft. Results reveal that at mode-1, frequencies decreased initially with an increase in load, and after buckling the P_{cr} trend reverses as seen from Figure 6.7b.

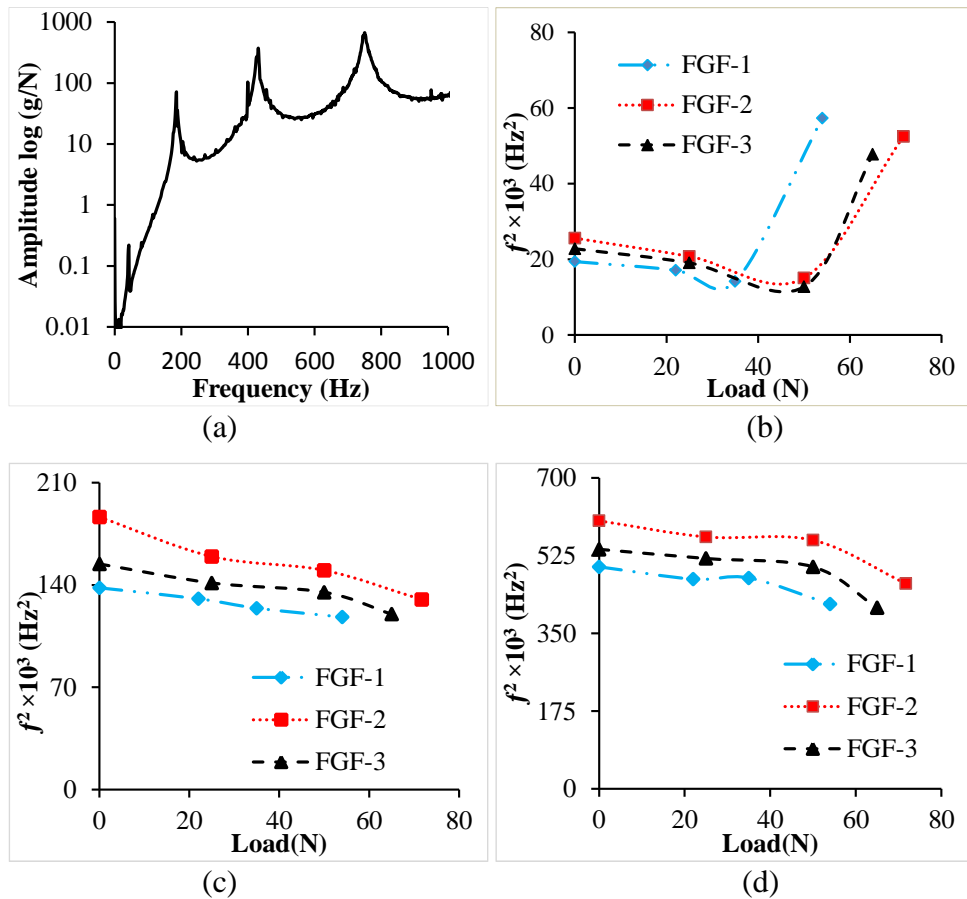


Figure 6.7. (a) FRF plot of FGF-2 and plots for comparing effect of uniaxial compressive force on natural frequencies at (b) Mode 1 (c) Mode 2 and (d) Mode 3.

This might be due to a gain in stiffness in the post-buckling regime. Similar behavior is observed in earlier studies conducted on the isotropic/composite beams and columns (Rajesh M and Jeyaraj. 2017, Wu Helong et al. 2015). As the P_{cr} is calculated corresponding to primary mode, natural frequency trend in post buckling

region is not observed for mode-2 and mode-3 as evident from Figure 6.7c and Figure 6.7d, respectively. For all the envisaged modes, FGF-2 exhibited higher frequencies compared to FGF-1 and FGF-3, which might be due to the higher stiffness exhibited by FGF-2. Experimentally evaluated natural frequencies corresponding to the first three modes at different loads are tabulated in Table 6.2.

Table 6.2. Influence of uniaxial compressive load on natural frequencies of FGFs.

FGF Type	Mode	Load (N)					P_{cr}
		0	25	50	75	95	
FGF-1	1st	139.2	134	127	239.3		
	2nd	371.49	361.3	352.3	349.35	$P_{cr}=73$	73
	3rd	698.48	687.2	695.8	645		
FGF-2	1st	159.94	153.04	141.6	125.19	229.13	
	2nd	431.8	399.37	390.94	384.37	320.85	$P_{cr}=92$
	3rd	866.21	843.21	866.51	840.3	769.92	
FGF-3	1st	150.91	144.94	124.1	218.64		
	2nd	392.85	375.98	371.1	312.50	$P_{cr}=75$	75
	3rd	734.46	720.26	726.4	638.43		

The damping ratio of FGFs corresponding to the first three modes is deduced from DEWESoft and is further evaluated using the circle fit method based on Equation 3. The experimentally evaluated damping factor corresponding to the first three modes at different loads is listed in Table 6.3. Results showed that the FGFs damping factor increases with increasing axial compressive load until the pre-buckled region and gets reversed in the post-buckling regime. This increase in the damping ratio in the pre-buckling region is due to an increase in filler-matrix interactions. Post buckling, the sudden stiffness rise leads to the decreasing damping ratio trend. The damping ratio of FGF-1 and FGFs at the first three modes is presented in Figure 6.8.

Table 6.3. Influence of uniaxial compressive load on damping factor of FGFs.

FGF Type	Mode	Load (N)					P_{cr}
		0	25	50	75	95	
FGF-1	1st	0.032381	0.03744	0.049615	0.04286		
	2nd	0.031567	0.037738	0.039481	0.035412	$P_{cr}=73$	73
	3rd	0.034483	0.036241	0.043961	0.037543		
FGF-2	1st	0.016199	0.027272	0.03265	0.040175	0.03088	
	2nd	0.015681	0.024111	0.026941	0.022677	0.020914	$P_{cr}=92$
	3rd	0.010403	0.015099	0.037531	0.030287	0.026287	
FGF-3	1st	0.027085	0.01266	0.033486	0.01967		
	2nd	0.027851	0.026303	0.043147	0.028941	$P_{cr}=75$	75
	3rd	0.031918	0.029312	0.031046	0.031724		

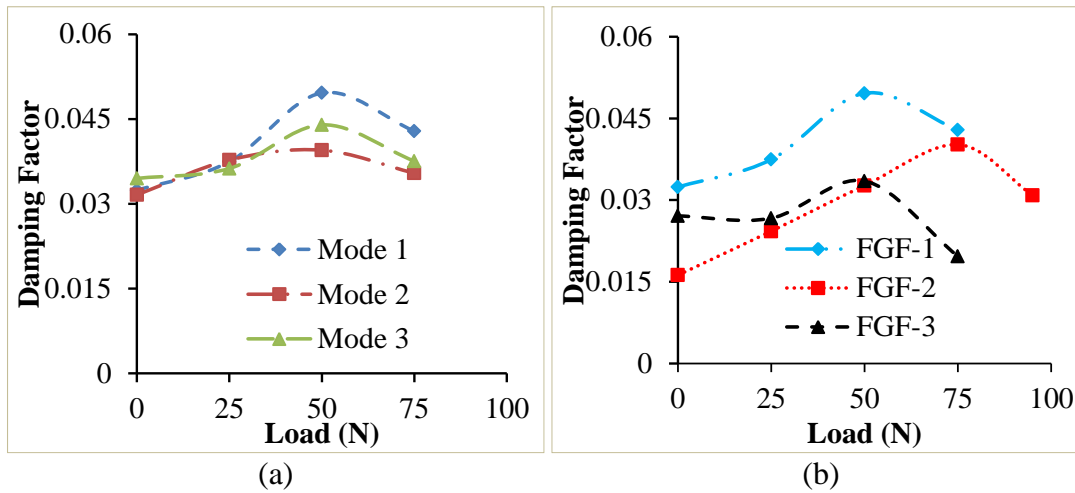


Figure 6.8. Representative plot for damping factor among different (a) Modes for FGF-1 and (b) FGFs.

The free vibration behavior of FGFs is also investigated using numerical analysis to predict natural frequencies corresponding to the first three modes under no-load conditions. Comparison among numerical and experimental results reveals that the natural frequencies obtained using numerical analysis exhibited a similar trend. Among FGFs, FGF-2 showed the high frequency values (Table 6.4). A slight deviation is observed among experimental and numerically evaluated frequencies due to the residual micro-porosities during 3D printing. Comparative studies of plain HDPE and FGF reveal the superior performance of the latter. The enhancement of natural frequencies in FGFs helps delay or control the occurrence of resonance phenomena effectively.

Table 6.4. Comparison of natural frequency under no load condition.

FGF Type	Mode	Natural Frequency (Hz)		Error (%)
		Experimental	Numerical	
FGF-1	1st	139.2	142.07	2.06
	2nd	371.49	396.11	6.62
	3rd	698.48	750.2	7.40
FGF-2	1st	159.94	160.43	0.36
	2nd	431.8	469.12	8.80
	3rd	866.21	880.36	1.60
FGF-3	1st	150.91	152.56	1.33
	2nd	392.85	436.17	11.02
	3rd	734.46	800.20	8.95

6.1.3 Estimation of critical buckling load using VCT

VCT is also looked into for evaluating the P_{cr} of concurrently printed FGFs, as no data is available in the prevailing literature. In VCT, load and frequency data are used to evaluate P_{cr} . The experimentally deduced natural frequency, subjected to compressive load lower than P_{cr} is computed for different loads. Then according to the second-order polynomial function, i.e., Equation 6.1, the curve is plotted for frequency squared values and load data and is extrapolated to corresponding load data at zero frequency to calculate P_{cr} . Figure 6.9a indicate P_{cr} of FGFs calculated using VCT display a similar trend across numerical, DTM, and MBC methods. Comparison of P_{cr} values evaluated using different methods are presented in Figure 6.9b. Such a comparison helps in estimating the upper and lower boundaries between which P_{cr} can vary.

$$\left(\frac{f}{f_n}\right)^2 = 1 - \frac{P}{P_{cr}} \quad (6.1)$$

Where f represents Frequency (Hz), f_n is natural frequency (Hz), p is mechanical load and p_{cr} is buckling load.

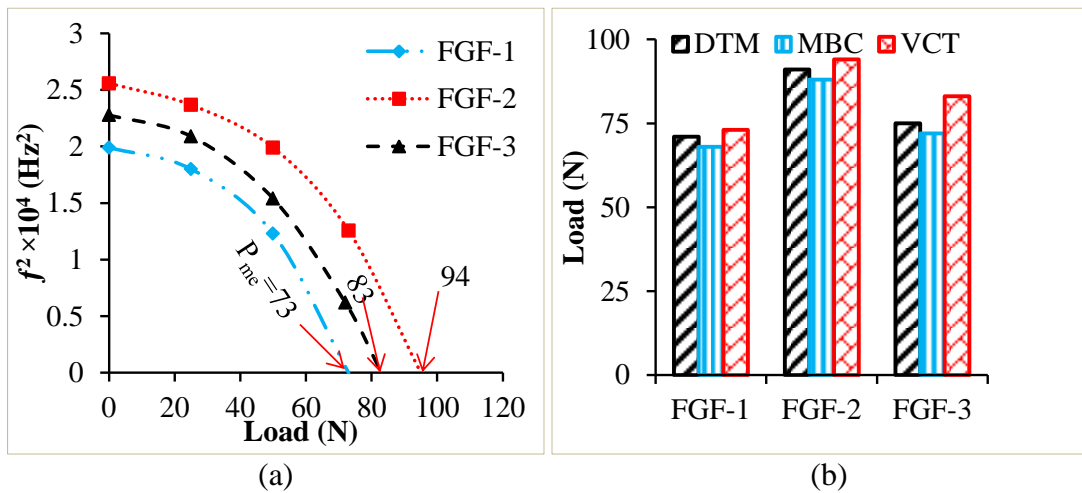


Figure 6.9. (a) Representative plot for evaluating P_{cr} using VCT and (b) comparison of DTM, MBC and VCT.

6.1.4 Property Chart

Density plays a crucial role in weight-sensitive applications; hence FGFs density and buckling strength are compared with the data extracted from the relevant literature. FGFs density is compared with 3D printed plain composites and thermosetting-based foams developed using the hand layup method (Bharath HS et al. 2020, Waddar Sunil et al. 2018, Waddar Sunil et al. 2019). Comparative results show that FGFs exhibited

better weight reduction potential than thermosetting-based foams and better mechanical buckling load than 3D printed plain foams with comparable density, as seen in Figure 6.10. This shows that replacing plain core with concurrently printed complex shaped integrated (leakproof/ joint less) FGFs can enhance the product quality for weight-sensitive applications like deep-sea oil drilling and marine structure applications.

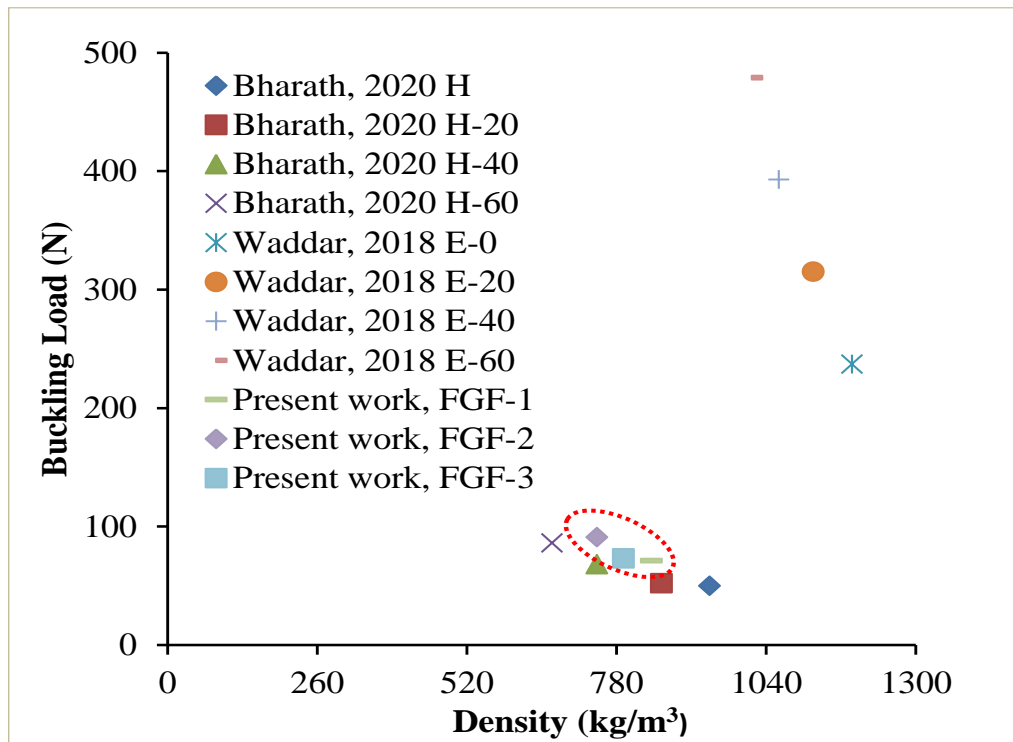


Figure 6.10. Buckling Load of different closed cell foams.

6.2 Buckling and free vibration of functionally graded sandwich foam

Functionally graded sandwich structures are 3D printed using optimized printing parameters. Figure 6.11 represents layers of the 3D printed FGSF-2 sample. This image clearly shows that layers are properly fused with one another. To assure this, using SEM analysis, representative interface images of top skin/H60 and bottom skin/H20 are captured, shown in Figure 6.12.

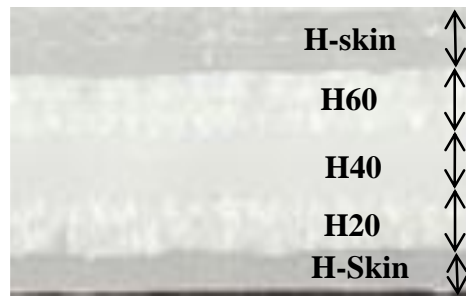


Figure 6.11. 3D printed FGFSF-2.

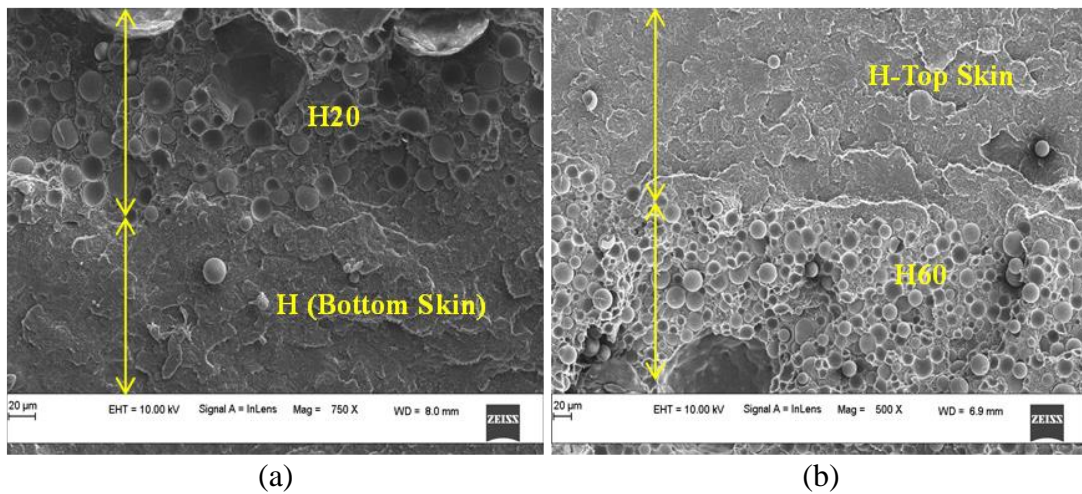


Figure 6.12. SEM images of (a) As casted layers (b) Filler sustainability of H60 (c) H-H20 interface and (d) H60-H interface of freeze fractured 3DP samples.

6.2.1 Critical buckling load of FGFSF

3D printed FGFSFs with fixed-fixed boundary conditions are subjected to uniaxial compressive load at a rate of 0.2 mm/min. This load is applied until the sample exhibits the buckling phenomenon. The test is terminated when the load-deflection response in DAQ stabilizes by exhibiting a continuous increase in the deflection without any significant load increase. Global buckling phenomenon is observed in all the FGFSFs with a null deflection at the fixed supports and maximum deflection at the center. Pre- and post-buckling states of representative FGFSF-3 are presented in Figure 6.13.

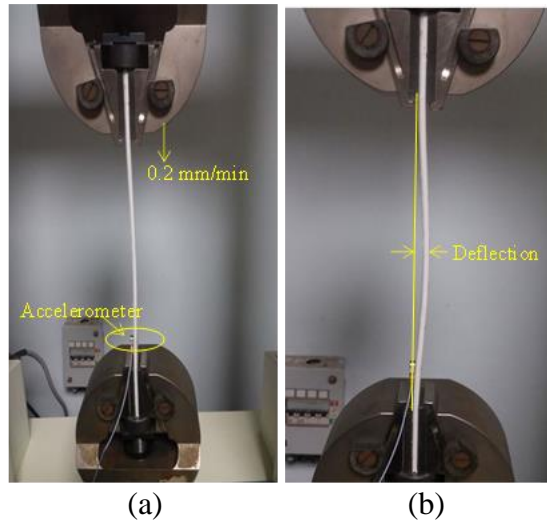


Figure 6.13. Representative image of (a) Pre and (b) post buckling state of FGSF-2.

Due to the progressive change of the material stiffness along the thickness direction, the sharp property transition at the 3D printed skin-core interface is eliminated. The variation of Bardella-Genna modulus along the thickness direction of FGSFs is shown in Figure 6.14a-Figure 6.14c. Moreover, as these sandwiches are 3D printed, the fused deposition of one layer over the other happens efficiently and seamlessly. Concurrent 3DP helps control the shear stresses between the layers when deflection under load creeps in and is evident from Figure 6.13, wherein the absence of delamination between the skin and core even at the buckled state (Figure 6.13b) can be clearly defined and observed. Experimentally acquired load-deflection plots of all FGSFs are presented in Figure 6.14d. It is observed that, among all FGSFs, for the same deflection magnitude, FGSF-2 exhibited a higher load requirement. This clearly shows that the FGSF-2 is stiffer than FGSF-1 and FGSF-3.

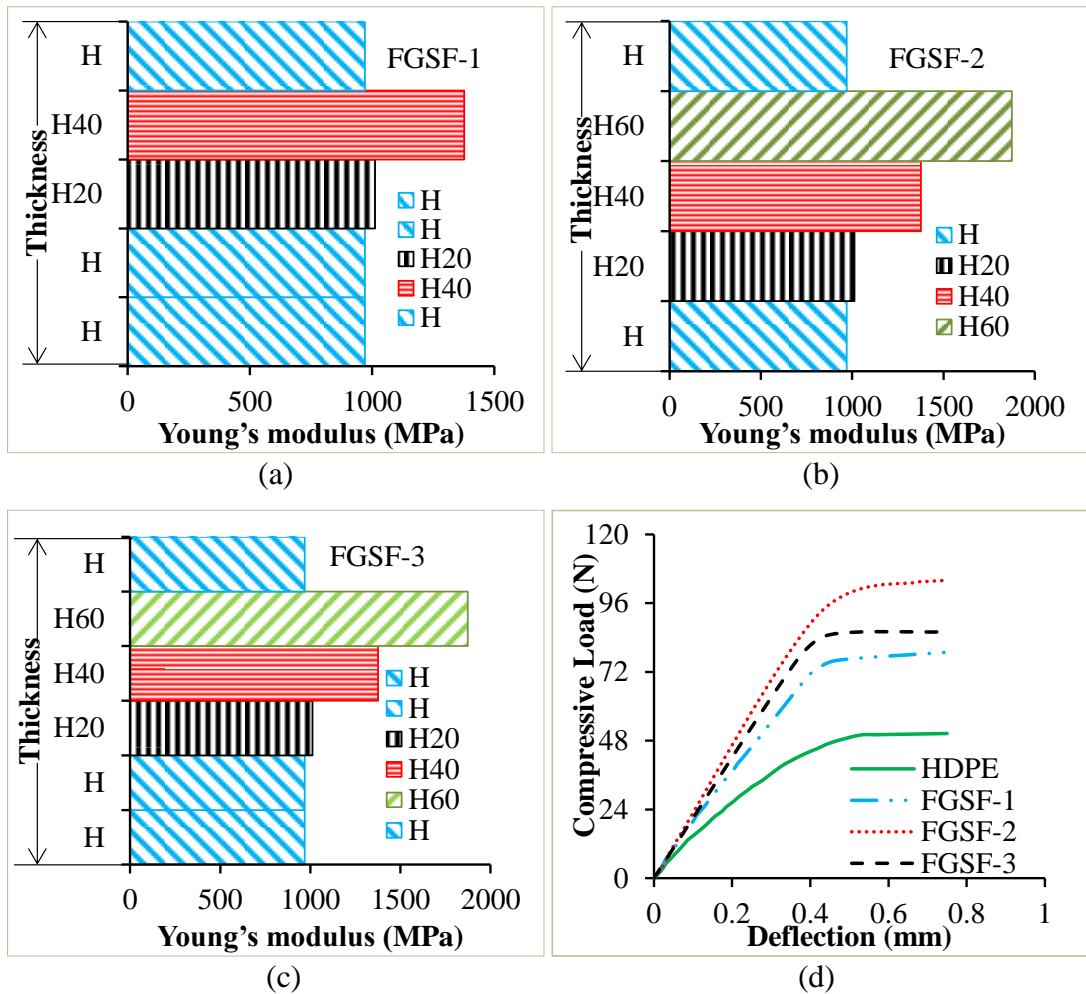


Figure 6.14. Representative (a-c) BGM variation, (d) load and deflection graphs of H and FGSFs.

P_{cr} of FGSFs is evaluated using DTM and MBC routes (Figure 6.15a and Figure 6.15b). Experimental evaluated P_{cr} values are listed in Table 6.5. From the results, it is observed that FGSF-2 exhibited better P_{cr} than FGSF-1 and FGSF-3. A combined phenomenon of gradual property variation and higher GMB content make FGSF-2 exhibit better stiffness than FGSF-1. Whereas comparatively more asymmetric stiffness variation is observed in FGSF-3 (Figure 6.14c) than in FGSF-2. The P_{cr} of FGSF-2 evaluated using DTM and MBC methods are 1.32, 1.19, and 1.34, 1.21 times FGSF-1 and FGSF-3, respectively. The addition of HDPE skin on the core made the sandwich exhibit better P_{cr} than their respective FG cores (FGF-1: H-H20-H40 = 71 ± 2.76 , FGF-2: H20-H40-H60 = 91 ± 1.53 , FGF-3: H-H20-H40-H60 = 75 ± 2.27). This is due to the reduced stress drop rate in FGSFs owing to concurrently printed

sandwiches. Figure 6.15c shows the superior load-deflection performance of representative FGSF compared to the respective FG core.

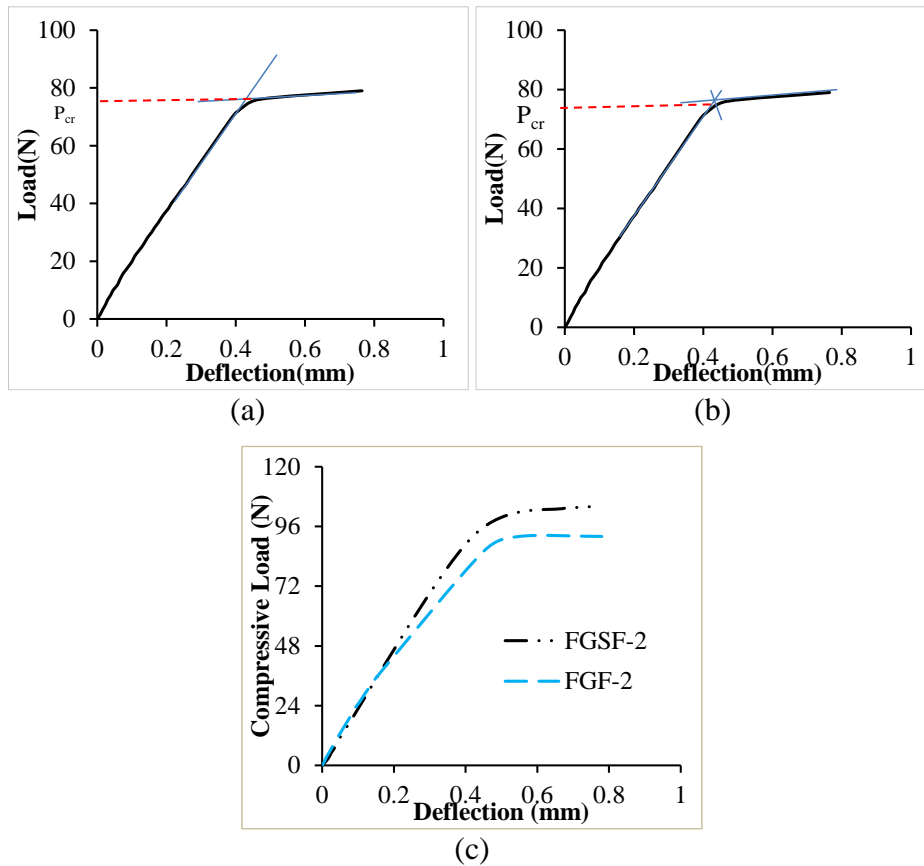


Figure 6.15. Evaluation of P_{cr} of FGSF-1 using (a) DTM and (b) MBC (c) Comparison of P_{cr} between FGSF and FGF.

Table 6.5. Experimental critical buckling load of FGSFs.

FGSF Type	Experimental P_{cr} (N)	
	DTM	MBC
FGSF-1	75	72
FGSF-2	99.5	97
FGSF-3	83	80

Compared to pure HDPE, the buckling strength of FGSF-1, FGSF-2, and FGSF-3 calculated using DTM and MBC methods are 1.5, 1.99, 1.66, and 1.53, 2.06, 1.7 times of HDPE, respectively (Bharath HS et al. 2020). Experimental P_{cr} values of FGSF-1, FGSF-2 and FGSF-3 predicted using DTM and MBC methods are 1.05, 1.09, 1.106 and 1.05, 1.10, 1.11 times of FGF-1, FGF-2 and FGF-3 respectively. Numerically

evaluated load-deflection graphs are plotted by varying the GIF value. Plots obtained for FGSF-1, FGSF-2, and FGSF-3 corresponding to the GIF values of 0.0005, 0.0001, and 0.0002 are presented in Figure 6.16.

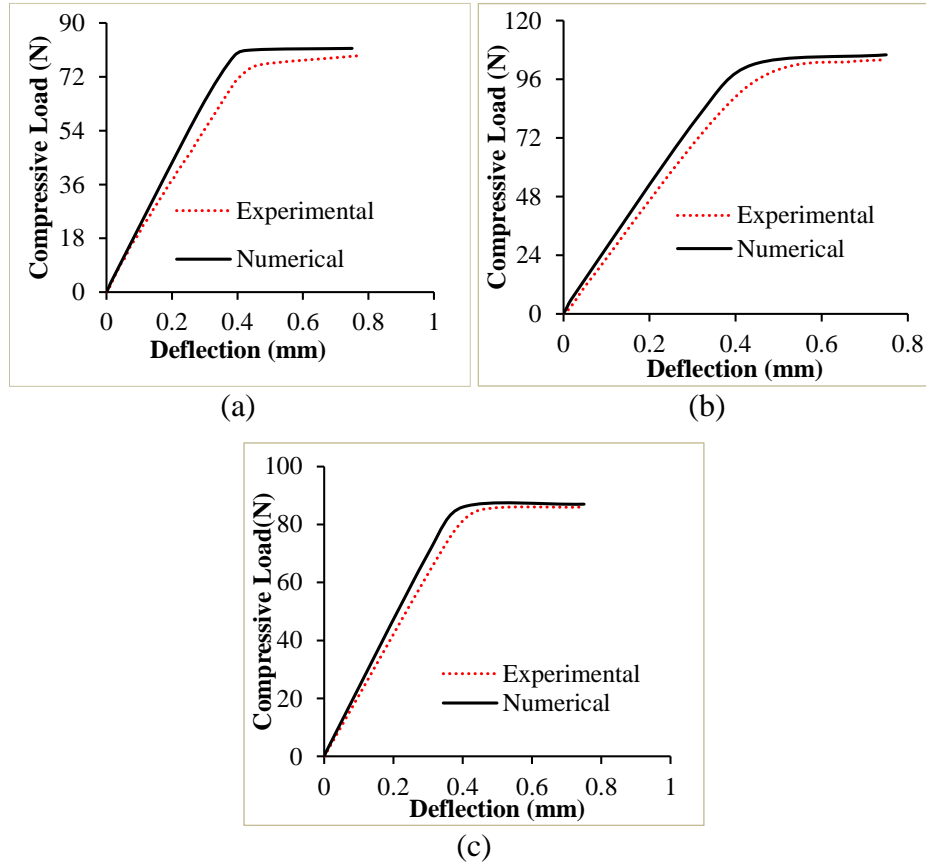


Figure 6.16. Comparison of Load-deflection graphs of (a) FGSF-1 (b) FGSF-2 and (c) FGSF-3.

From comparative studies Table 6.6, it is observed that there is a minor deviation between numerical and experimental results. This deviation is due to quasi-static material assumption, the exact unknown value of GIF, and voids induced in the FGSFs while printing. P_{cr} value calculated using the DTM is higher than the MBC method. These P_{cr} values corresponding to DTM and MBC methods are considered the respective upper and lower boundaries of FGSFs. The potential of FGSFs to exhibit higher P_{cr} values compared to H-H60 and their respective FGFs (FGF-1, FGF-2, FGF-3) has shown its significance in replacing the cores with FGSFs for weight-sensitive applications.

Table 6.6. Experimental and theoretical critical buckling load of FGSSFs.

FGSF Type	Experimental P_{cr} (N)		Numerical P_{cr} (N)		% Deviation of experimental with respect to numerical	
	DTM	MBC	DTM	MBC	DTM	MBC
FGSF-1	75	72	80	77	6.25	6.49
FGSF-2	99.5	97	103	100	3.39	3.00
FGSF-3	83	80	87	85	4.59	5.88

6.2.2 Free vibration behavior of FGSSF

Resonance is one of the significant problems that significantly affect the failure of a component, which primarily depends on the natural frequency. The natural frequencies of the 3D printed FGSSFs are estimated using an experimental and FE-based numerical approach. The free vibration behavior of FGSSFs is investigated under fixed-fixed conditions by exciting with a roving impact hammer. The generated frequency response functions (FRF) of FGSSFs are measured using an accelerometer. Frequency values corresponding to the first three modes are measured and tabulated in Table 6.7. FRF of representative FGSSF-3 is shown in Figure 6.17.

Table 6.7. Natural Frequencies of FGSSFs.

FGSF Type	Mode	Load (N)					P_{cr}
		0	30	60	90	120	
FGSF-1	1st	150.30	122.03	101.24	236.83		
	2nd	380.19	329.59	293.912	280	$P_{cr}=75$	75
	3rd	770.99	750	722.15	710.64		
FGSF-2	1st	165.12	142.40	137.21	133.74	214.81	
	2nd	450.60	392.32	373.29	353.71	329.6	$P_{cr}=99.5$
	3rd	810.34	770	750.23	742	683.6	
FGSF-3	1st	155.17	140.94	135.50	242.87		
	2nd	395.67	368.7	360.34	313.92	$P_{cr}=83$	83
	3rd	726.88	710.38	704.93	680.96		

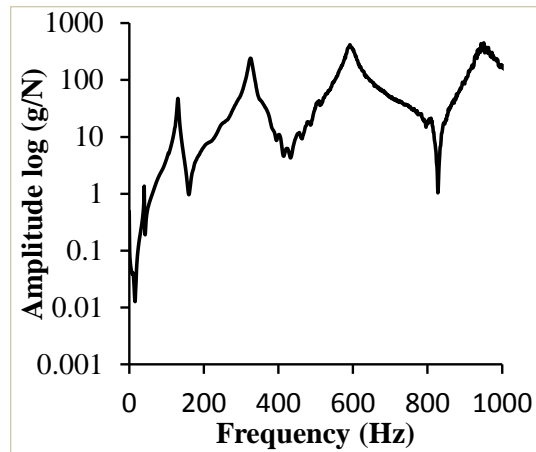


Figure 6.17 Representative FRF curve of FGSF-3.

All FGSFs, at mode-1 exhibited a reduction frequency with an increasing compressive load in the pre-buckling region. A sudden frequency rise is observed in the post-buckling zone, which might be due to an increase in the stiffness of FGSFs in their buckled state. As the P_{cr} is evaluated corresponding to the first mode, a similar trend of natural frequency is absent for mode-2 and mode-3. Among all FGSFs, FGSF-2 exhibited high natural frequency due to its higher stiffness. Table 6.8 lists all the frequency values of FGSFs corresponding to the first three modes evaluated using experimental and numerical routes. The deviation of experimental frequencies with respect to corresponding numerically evaluated frequencies is mentioned in Table 6.8.

Table 6.8. Experimental and numerical comparison of FGSFs under no load condition.

FGSF Type	Mode	Natural Frequency (Hz)		Error (%)
		Experimental	Numerical	
FGSF-1	1st	150.30	152.83	1.66
	2nd	380.19	428.55	11.28
	3rd	770.99	785.63	1.86
FGSF-2	1st	165.12	168.01	1.72
	2nd	450.45	464.62	3.04
	3rd	810.34	850.46	4.71
FGSF-3	1st	155.17	157.88	1.71
	2nd	395.67	444.13	10.91
	3rd	726.88	800.23	9.16

The deviations between the experimental and numerical approaches may be due to the residual micro-porosities, in-situ voids, and quasi-static material assumptions.

Experimental damping factor values of FGSFs calculated using Equation 3 are directly taken from DEWESOFT. The damping factor values of all FGSFs corresponding to the first three modes are presented in Table 6.9. It is observed that the damping factor increases in the pre-buckling zone, with load increase, and the trend gets reversed in the post-buckling zone Figure 6.18a. Experimentally obtained load and damping factor graphs for a different mode of FGSF-1 and among FGSFs corresponding to the first mode are exhibited in Figure 6.18a and Figure 6.18b.

Table 6.9. Damping Factor corresponding to first three modes of FGSFs.

FGSF Type	Mode	Load (N)					P_{cr}
		0	30	60	90	120	
FGSF-1	1st	0.029648	0.033606	0.03427	0.025801		$P_{cr}= 75$
	2nd	0.021928	0.02405	0.027074	0.018838		
	3rd	0.01622	0.017482	0.025215	0.014295		
FGSF-2	1st	0.021718	0.023918	0.030221	0.031339	0.01921	$P_{cr}= 99.5$
	2nd	0.012248	0.021678	0.024252	0.029312	0.02159	
	3rd	0.009051	0.013449	0.026616	0.024246	0.01796	
FGSF-3	1st	0.025902	0.031458	0.032952	0.024814		$P_{cr}= 83$
	2nd	0.015806	0.01899	0.025551	0.020581		
	3rd	0.018878	0.015986	0.021842	0.018941		

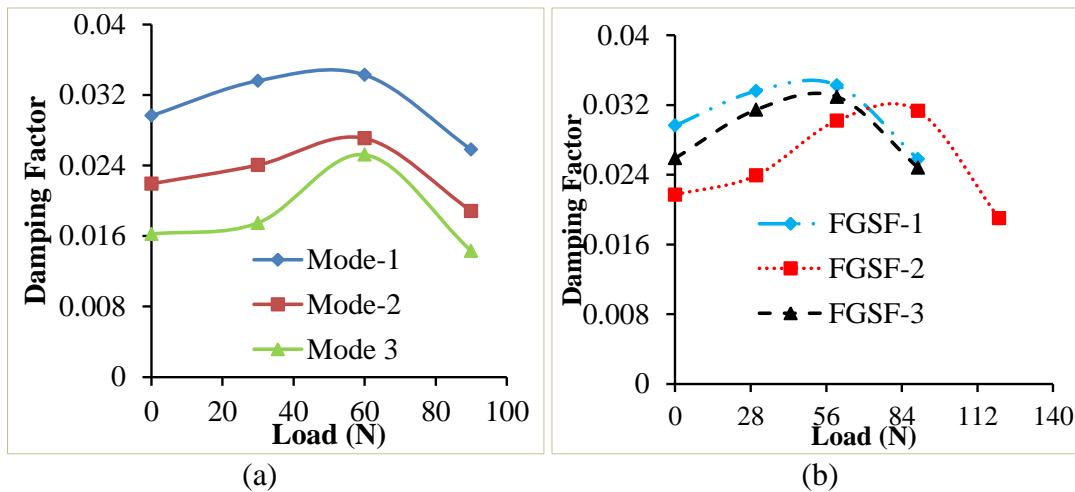


Figure 6.18. Representative plot of load-damping factor among (a) different modes of FGSF-1 and (b) FGSFs.

6.2.3 Property chart

The density and P_{cr} values are compared with extracted data from the literature. 3DP FGSFs densities are compared with plain core and sandwich composites developed using 3D printing (Bharath HS et al. 2021) and thermosetting based sandwich foam

beams developed using the hand layup method (Waddar Sunil et al. 2019) in Figure 6.19. This property chart helps observe the property variation concerning manufacturing methods and different core materials. It is observed that FGSFs have better weight reduction potential compared to thermosetting-based sandwich beams and better P_{cr} values compared to plain core-based 3D printed sandwiches. Figure 6.19 presents the property map that helps industrial practitioners, material scientists, and designers choose a proper material system and associated manufacturing route.

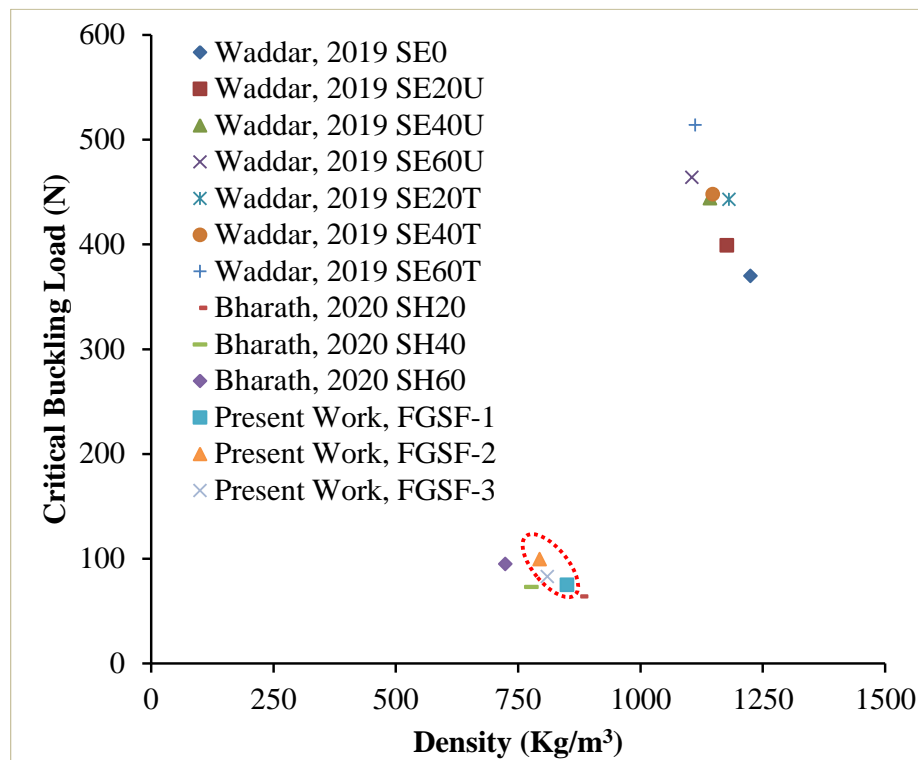


Figure 6.19. Comparison of Critical buckling load and densities among different foam based sandwich beams.

Conclusion

3D printed FGF and FGSFs are investigated for mechanical buckling and free vibration behavior using experimental and numerical techniques. The findings are summarized as follows.

- All FGF and FGSFs of considerable length (310 mm) are concurrently 3D printed without defects and warpage issues using apt printing parameters.
- SEM reveals proper bonding between the different compositional layers with intact GMBs.

- Compared to pure H buckling strength of FGF-1, FGF-2 and FGF-3 calculated using DTM and MBC methods are increased by 39, 78.4, 47 %, and 44.68, 87.23, 53.19%, respectively.
- Among plain core and FGFs, FGF-2 exhibited a higher buckling load and natural frequency. Among FGFs, FGF-2 exhibited the highest buckling strength.
- At mode-1 natural frequency decreases with an increasing compressive load, and trend reversal creeps in the post-buckling regime. The damping factor showed a reverse trend with respect to the compressive load.
- Among all FGSFs, FGSF-2 exhibited better P_{cr} and natural frequency.
- The natural frequency of FGSFs decreases in the pre-buckling zone and increases in the post-buckling zone.
- Compared to plain core sandwiches, FG core sandwiches gave better results for P_{cr} and natural frequency.

The results of the experimental analysis are found to be in very good agreement with numerical results. The concurrent 3D printing of FG cored sandwiches and their superior performance opens up newer materials design avenues for realizing complex-shaped integrated FGSF sandwiches. The proposed printing strategy of FGSFs successfully eliminated delamination effects at the skin-core interface. Further, these FGSFs exhibited enhanced dynamic response and good weight reduction potential. The FGSFs developed are capable of replacing the plain cored sandwich composites for buoyancy-aided lightweight applications.

7. THERMAL BUCKLING

In the present work to study the (1) Influence of the hollow GMB reinforcement on temperature (heat) distribution, (2) Effect of thermal load position on the lateral deflection of 3DP plain, graded, and their respective sandwich composite beams, and (3) Significance of material gradation rather than opting plain beams, HDPE/GMB based plain, graded, and their respective sandwich syntactic foams are 3D printed. SEM images at the interface of various compositions are shown in Figure 7.1.

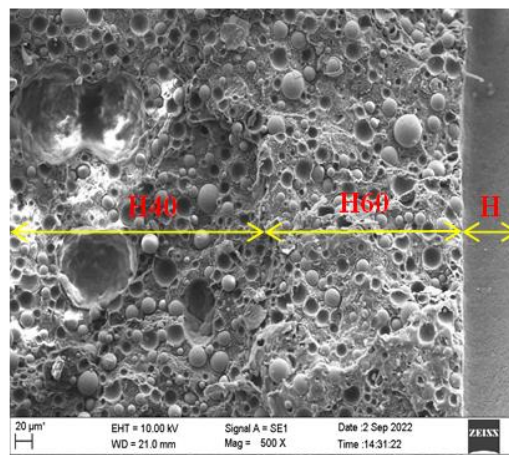


Figure 7.1. Interface of H40-H60-H.

7.1 Experimental analysis of thermal buckling

In this experiment, the beam under clamped-clamped boundary conditions is subjected to thermal load using IR heater. Here the displacement at both ends was restricted, so thermal stresses were developed in the beam and started deflecting. The maximum deflection in the fundamental mode is mostly observed in the middle of the beam, so LVDT is fixed at the centre of one side of the beam surface, as shown in Figure 2.16. As the beam thickness is relatively less (4 mm), thermal sensors are placed on front and back surfaces, as shown in Figure 7.2a (temperature variation along the thickness direction). The result data of DAQ indicates a 40-45°C variation. This is due to the lower thermal conductivity of hollow GMB particles (Figure 7.2b and Figure 7.2c). The hollow space inside the filler particles offers more resistance to heat flow than matrix material, resulting in a high thermal gradient between the surfaces exposed to a heater and another beam surface. The scanning electron microscopic image of hollow GMB reinforced HDPE composite is shown in Figure 7.2b. When the sample is subjected to different thermal loading conditions, three

types of buckling phenomenon are observed primary is normal buckling, secondary is snap-through buckling, and tertiary is gradual softening with minor vibration. When a sample is heated from one of its faces, non-uniform temperature distribution will occur, resulting in non-uniform stiffness along the thickness direction. Along with this, the thermal moment may also be developed, which creates a bending phenomenon with the increase in temperature. The eccentric moment will also cause the move the neutral axis from the centroid of the sample due to non-uniform temperature distribution (Liu L et al. 2006). So column behaves like an imperfect beam and may not buckle like the classical Euler buckling phenomenon.

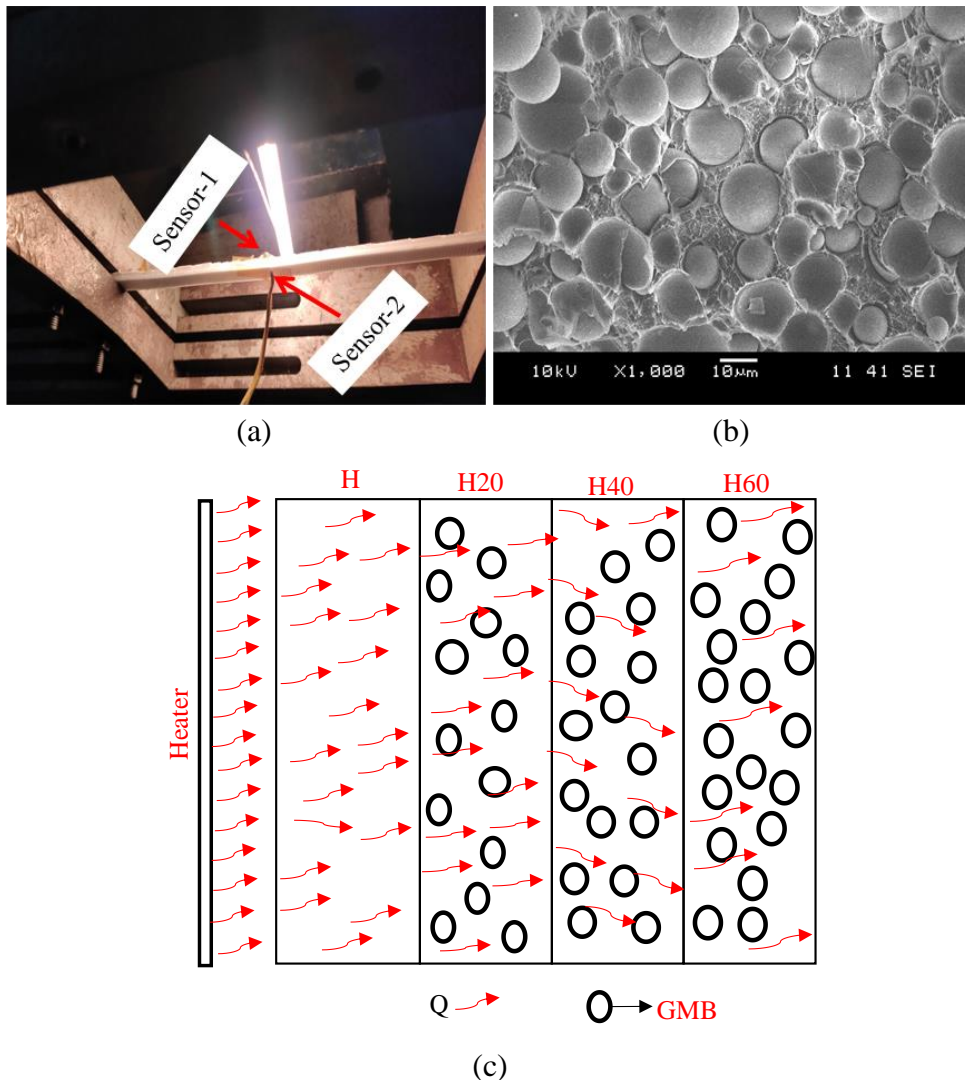


Figure 7.2. Representative picture of (a) sensor arrangement to measure temperature across cross-section (b) SEM of syntactic foam, and (c) Heat flow with respect to GMB percentage.

7.1.1. Case1: One end heating

In case 1, the sample is subjected to thermal load at one end, and the temperature distribution versus deflection along the length of the sample is studied. The temperature profile along the length direction for case-1 is shown in Figure 7.3. The results show that the sample exhibited a dimensional buckling phenomenon, and the critical thermal buckling temperature (T_{cr}) values of all 3D printed samples for case-1 are mentioned in Table 7.1. Temperature versus deflection graphs is presented in Figure 7.4. Among the plain samples, i.e., H, H20, H40, and H60, the neat H sample exhibited less buckling temperature of 46.95°C due to less heat resistance and comparatively higher CTE. The CTE values of H, H20, H40, and H60 are $135 \pm 3.29 \times (10^{-6} \text{ per } ^{\circ}\text{C})$, $106 \pm 3.85 \times (10^{-6} \text{ per } ^{\circ}\text{C})$, $88 \pm 2.65 \times (10^{-6} \text{ per } ^{\circ}\text{C})$, and $75 \pm 1.15 \times (10^{-6} \text{ per } ^{\circ}\text{C})$ which are considered from our previous work on foams (Bharath HS et al. 2020). The H20 sample initially exhibited resistance to the thermal load, but at 66.70°C , it showed sudden deflection. Due to the higher volume percentage of the GMB in H40 and H60, they did not conduct the heat along the length, resulting in less deformation at the center of the sample. The higher storage modulus of H40 and H60 might also be one of the reasons for exhibiting the lower deflection (Bharath HS et al. 2020). Few works on foams stated that the storage modulus increases with an increase in hollow filler percentage (Mrityunjay. 2020).

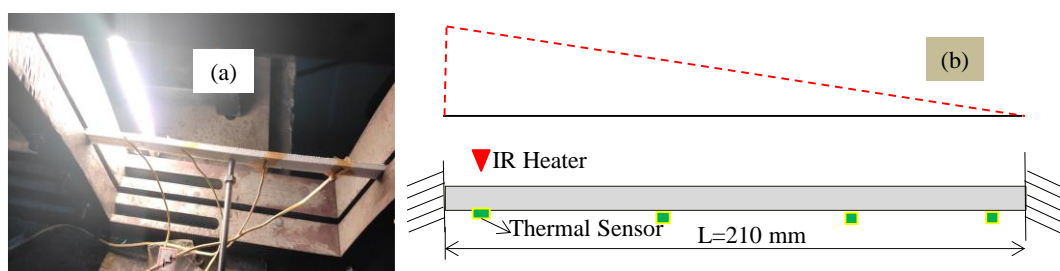


Figure 7.3. Represents images of case-1 (a) Heating position and (b) temperature distribution.

Table 7.1. Case-1 buckling temperature of 3D Printed Samples.

Sample Type	Case-1 (End-Heating)
	T_{cr}
H	46.95
H20	67.22
H40	79.8
H60	(local-softening)
SH20	59.65
SH40	66
SH60	72.4
FGF-1	47.5
FGF-2	55.54
FGF-3	(local-softening)
FGSF-1	(local-softening)
FGSF-2	(local-softening)
FGSF-3	(local-softening)

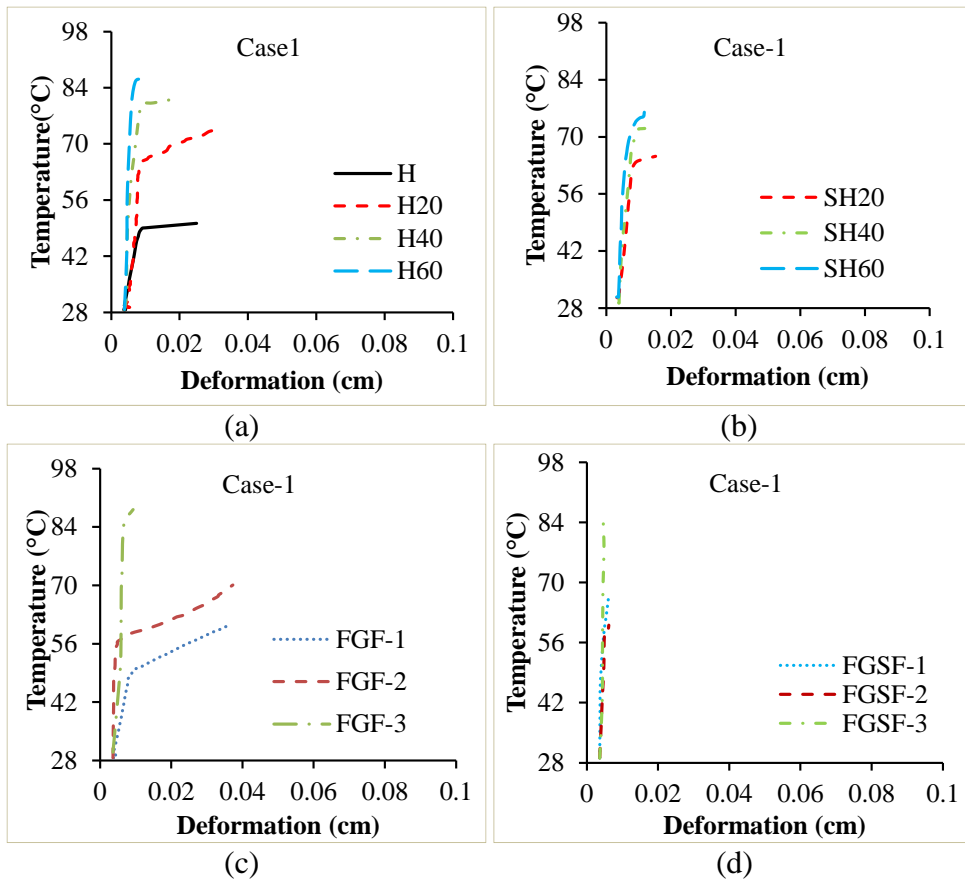


Figure 7.4. Temperature versus deformation graphs of case-1 for (a) Plain (b) Plain-Sandwich (c) FGF's and (d) FGSF's.

The continuous temperature increases cause the thermoplastics to soften, resulting in a loss of stiffness along the thickness direction (Figure 7.5). To increase the stability of the sample under thermal loading conditions, sandwich samples of all respective cores were also 3D printed and tested for thermal buckling. The sandwiches of these respective plain beams exhibited a similar trend. FGF's IR heater is placed towards the foam layer with a higher filler percentage, i.e., FGF-1 at the H40 phase and FGF-2 and FGF-3 at the H60 phase. As the coefficient of thermal expansion and conductivity are the major parameters to be considered to analyze thermal effect, the foam layers with lower CTE and conductivity are placed toward the heater side resulting in heat flow resistance while layer's backside resists deflection. Among the FGFs developed by varying material properties along the thickness direction, FGF-1 and FGF-2 exhibited a dimensional buckling phenomenon, whereas FGF-3 did not exhibit proper deformation. This might be due to the phenomenon of elongation in compound beams where one layer obstructs the motion of the other. The layer facing the IR heater possesses higher temperatures than other faces. So the layers at lower temperatures with different CTE and thermal conductivity will inhibit the motion of the high-temperature layers. This phenomenon might result in diminishing the deflection. The same phenomenon is observed in FGFSF, inhibiting the deflection and exhibiting localized melting, and the deflection amount is lesser than in FGF Figure 7.4d. This signifies that the stability of the beam increased upon sandwiching.

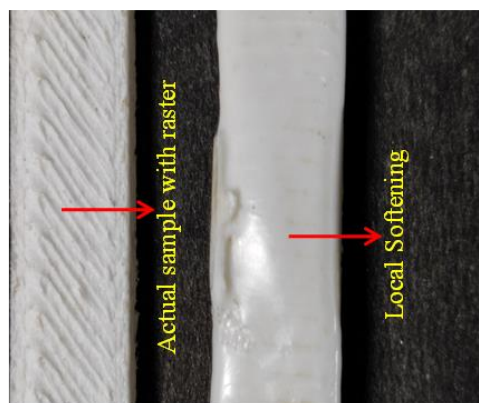


Figure 7.5. Local softening.

7.1.2 Case2: Centre heating

In this case, the IR heater and LVDT are placed opposite each other at the center of the beam. Once the experiment started, the IR heater started heating the sample slowly, and the heat was transferred from the center to both clamped ends. The temperature profile along the length direction for case-2 is shown in Figure 7.6. In this case, as the sample is directly heated at the center, which is the most suspected position, where maximum deflection is supposed to occur as per mode-1, compared to other cases, the deflection of the beam is higher. The temperature versus deflection graphs are shown in Figure 7.7, and the buckling temperatures of the respective samples of case-2 are mentioned in Table 7.2. In this case, plain samples exhibited snap-through buckling. i.e., when the sample is heated, initially, due to induced thermal stress, the sample starts deforming in one direction. After some time, due to the phenomenon of viscoelastic force regain sample started reaching its original non-deformed position, and further heating started deforming in the opposite direction. The temperature versus deflection graph is shown in Figure 7.7(a), and the buckling temperature is calculated using the double tangent method in Figure 7.7(a).

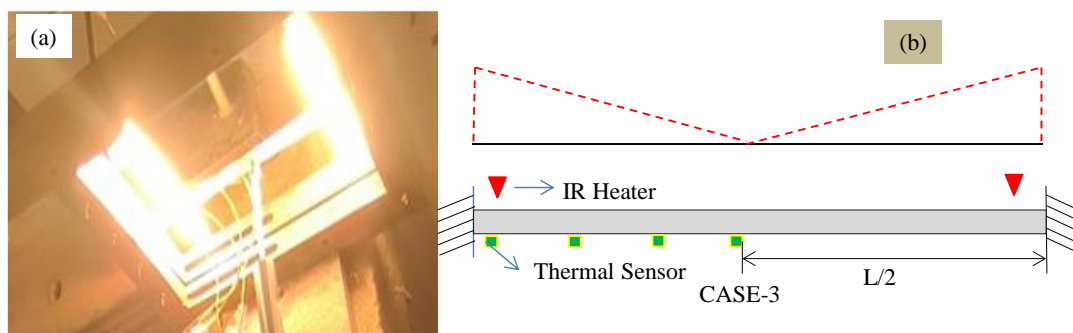


Figure 7.6. Representative images of case-2 (a) Heating position and (b) temperature distribution.

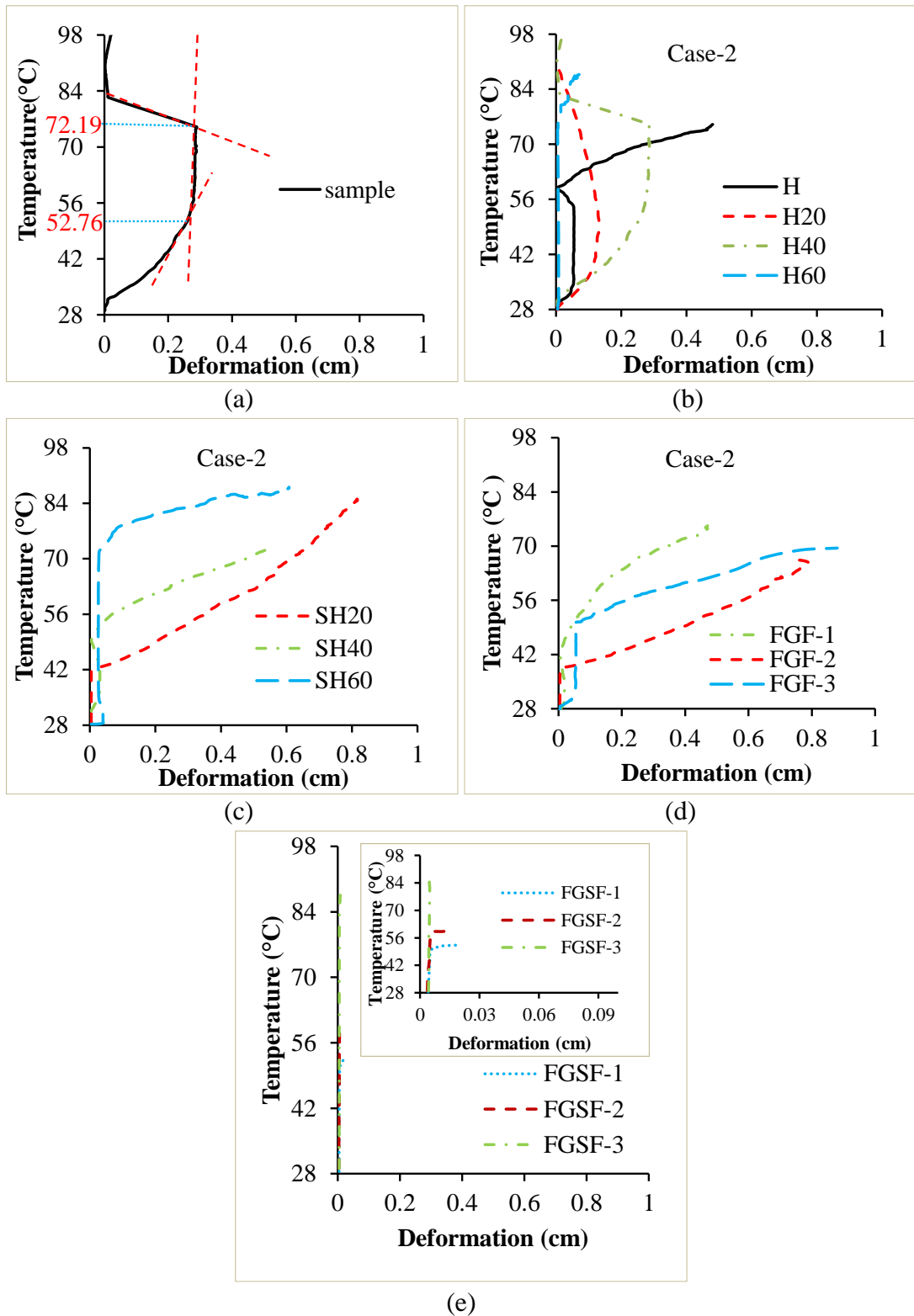


Figure 7.7. Temperature versus deformation graphs of case-2 for (a) Snap through buckling (b) Plain (c) Plain-Sandwich (d) FGF's and (e) FGSF's.

This snap-through buckling phenomenon is observed due to the release and restoration of the viscoelastic forces. Few researchers, like (Waddar Sunil et al. 2018), observed this snap-through buckling phenomenon in cenosphere reinforced epoxy-based composite made by hand lay-up method. (Kanakannavar Sateeshkumar and Jeyaraj. 2021)observed the snap-through buckling phenomenon in PLA composite (Gilorkar Amol et al. 2020). They observed similar behavior in sisal and glass are woven reinforced epoxy composite beams made by hand lay-up method. Moreover, when the sample is heated from one of its faces, non-uniform temperature distribution will occur, resulting in non-uniform stiffness along the thickness direction. Also, a thermal moment may develop, creating a bending phenomenon with increased temperature. An eccentric moment will also cause due to the shift of the neutral axis from the centroid of the sample due to the non-uniform distribution of temperature. So column bends like an imperfect beam and may not buckle like the classical Euler buckling phenomenon. The exhibition of the buckling behavior like an imperfect beam is controlled by sandwiching it with HDPE skin Figure 7.8(a). In FGF and FGSF, due to the variation of CTE value along the thickness direction, the tensile and compressive forces restrict each and minimize this snap-through buckling shown in Figure 7.8b. Among FGFs, FGF-3 exhibited a buckling temperature of 51.7°C, and in FGSFs, FGSF-3 exhibited local softening rather than the buckling phenomenon. Compared to case-1, case-2 exhibited higher deflection due to the placement of the heater and LVDT at the critical sample position. Though case-2 exhibited comparatively higher deformation, there is no delamination between the layers of the graded samples shown in Figure 7.8c and Figure 7.8d. This indicates that the 3D printing of graded samples has been done with proper fusion among the layers of different compositions.

Table 7.2. Buckling temperatures of case-2.

Sample Type	Case-2 (Centre-Heating)	
	T_{cr-1}	T_{cr-2}
H	34.7	52.64
H20	39.09	48.47
H40	52.76	72.19
H60	(local-softening)	----
SH20	41.76	----
SH40	48.68	----
SH60	69.67	----
FGF-1	39.93	----
FGF-2	37.34	----
FGF-3	50.94	----
FGSF-1	49.8	----
FGSF-2	56.47	----
FGSF-3	(local-softening)	----

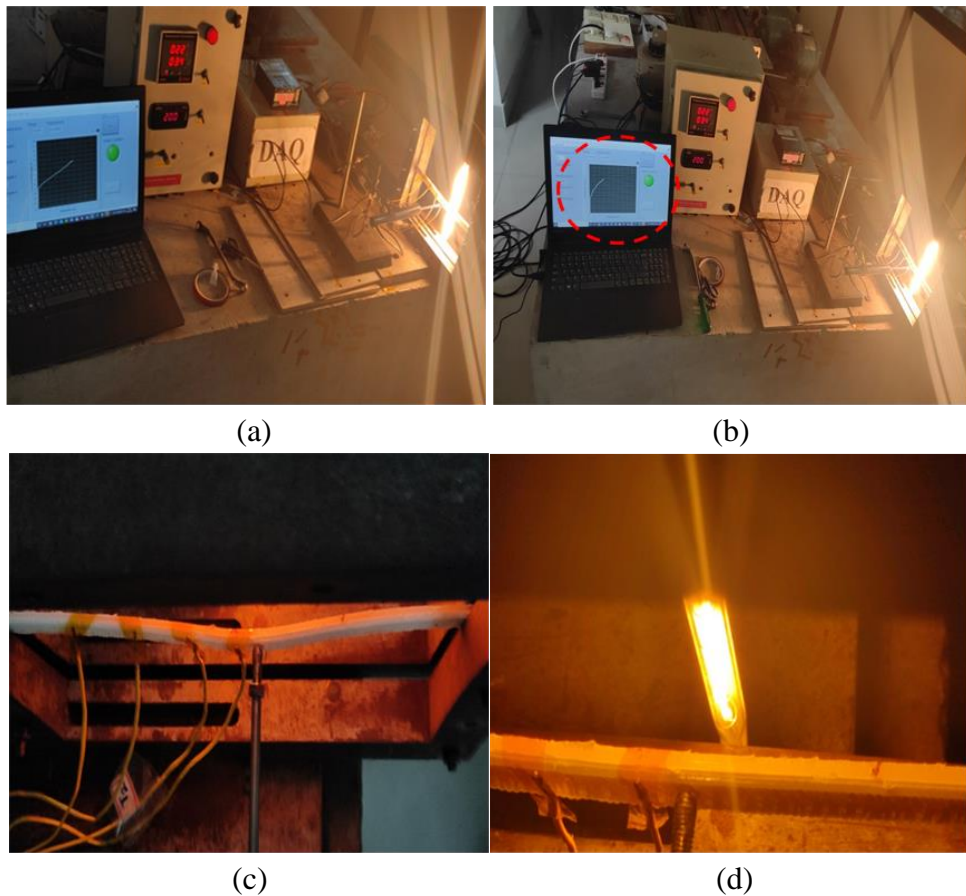


Figure 7.8. Buckling of (a)SH20 (b) FGF-1 (c) mode-1 buckling shape of FGF-1 and (d) sample with no delamination.

7.1.3 Case:3 Both end heating

In the current case, the thermal load is given at both ends using two IR heaters, and LVDT is placed at the center of the sample to measure the deflection. The temperature profile along the length direction for case-3 is shown in Figure 7.9. The sample did not exhibit deflection when the sample was initially fixed in frame and started heating due to viscoelastic forces and its storage modulus. These viscoelastic forces release upon increasing the temperature, and the sample deflects. The behavior of the HDPE sample from the fixing position to the buckling position (mode-1) is shown in Figure 7.10. All most all samples of plain, plain-sandwich, and functionally graded foams exhibited normal buckling phenomena without much-restoring forces or local melting, as shown in Figure 7.11.

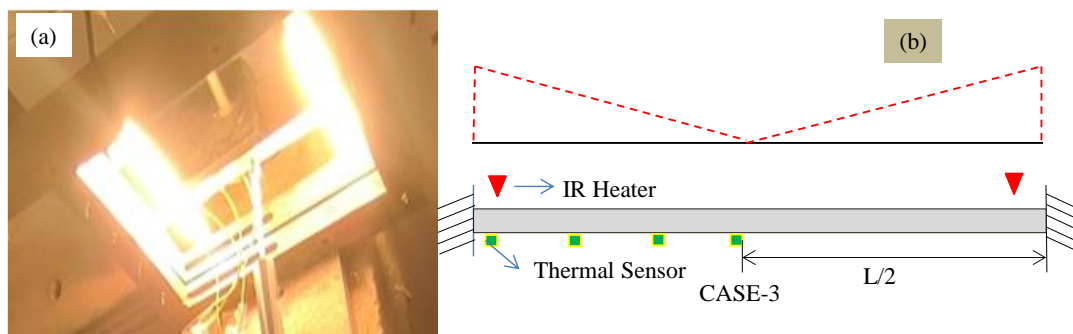


Figure 7.9. (a) Heating condition and (b) Temperature distribution.



Figure 7.10. 3DP HDPE sample (a) Before testing (b) while testing and (c) post buckling.



Figure 7.11. Dimensional buckling of H40.

The temperature versus deflection graphs of all samples is shown in Figure 7.12. The critical buckling temperatures of all the samples are mentioned in Table 7.3. From the results of buckling temperature, it is observed that there is a significant difference in buckling temperatures among different configurations of plain and FGF. In contrast, this difference is not much observed in sandwiches. These samples exhibited comparatively less deflection in the present case compared to case 2. When we experimented with observing the buckling behavior of FGSFs, These samples showed minor deflection compared to others, and the temperature versus deflection appeared to be a little wavy. This might be due to the combined effect of primary restoring viscoelastic forces and secondary non-uniform tensile and compressive forces caused due to temperature gradient along the thickness and material property gradation. The deflection of sandwich beams is comparatively less than the plain core. The sandwiches outperformed their respective core in terms of stability which shows its significance in replacing plain beams with functionally graded sandwich beams.

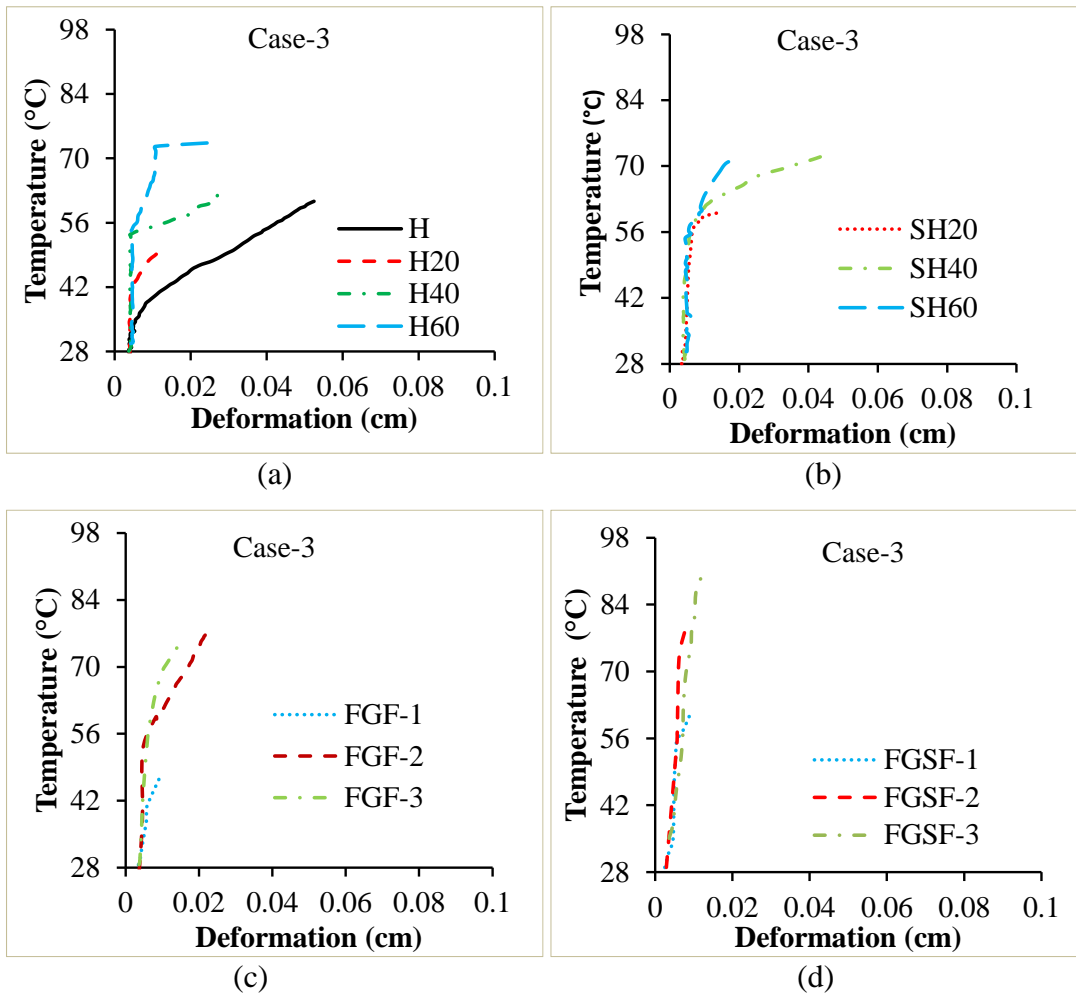


Figure 7.12. Temperature versus deformation graphs of case-3 for (a) Plain (b) Plain-Sandwich (c) FGF's and (d) FGFSF's.

Table 7.3. Buckling temperature of case-3.

Sample Type	Case-3 (Both-End-Heating)
	T_{cr}
H	36.86
H20	41.98
H40	52.47
H60	70.22
SH20	55.58
SH40	57.95
SH60	59.08
FGF-1	40.76
FGF-2	55.29
FGF-3	(local-Softening)
FGSF-1	(Local-softening)
FGSF-2	(local-softening)
FGSF-3	(local-softening)

Conclusion

- 3D printed samples subjected to different thermal loading conditions exhibited three types of buckling phenomenon: the primary is normal buckling, the secondary is snap-through buckling, and the tertiary is gradually softening with minor vibration.
- H60 exhibited better resistance to deflection among all plain samples.
- 3D printed sandwiches offered better resistance to deflection compared to their respective cores.
- FGSFs outperformed all 3D printed samples by enhancing the stability of the beams.
- All 3D printed samples exhibited higher deformation in case-2 (center heating) and minimum deflection in case-1 (one-end heating).

The functionally graded sandwich beams exhibited superior response compared to plain beams. Further, replacing the plain HDPE sample with syntactic foam helps in increasing the thermal resistance for insulation applications.

8. SUMMARY AND CONCLUSIVE REMARKS

Summary

Hollow GMB/HDPE based syntactic foam filaments are developed for commercial FFF 3D printers in the present work. These filaments are mostly used for lightweight applications. The extruded filament is subjected to SEM analysis to check the roundness of the cross-section and filler sustainability. Further, these filaments are used as the feed stock material to the 3D printer for developing plain, functionally graded cores and their respective sandwiches. Extensive microscopic analysis was performed on the 3D-printed samples to visualize the interface bonding, filler sustainability, and filler/matrix interphase. Results showed that the interface between the similar and dissimilar layers was properly fused, and there was no observable filler failure and agglomeration. This 3D printing of functionally graded syntactic core and their sandwiches is introduced through this work. The behavior of these 3D printed beams under various loads (mechanical, thermal) and loading conditions (axial, transverse) was studied. Extensive micrographic analysis was performed on tested samples to study the failure mechanism of these beams with respect to loading conditions. The results obtained from this work are compared with previous works available in literature. Property charts are plotted to make the industrial practitioners work easier in selecting the correct manufacturing method and material for the envisaged application.

Conclusion

The major conclusion of the present work are summarized below

Blend characterization

- Flowability of the developed composite through the orifice is measured using the melt flow index (MFI).
- MFI of the composite decreases with an increase in the filler percentage.

3D Printing parameters

- The effect of various 3D printing parameters on the part quality is presented.
- Possible defects in 3D printing components and solutions to overcome these problems are mentioned in the current work.
- 3D printing parameters are optimized using pilot studies.

- Nozzle temperature while processing HDPE filament was maintained as 225°C, H20 - 225°C, H40, and H60 - 245°C.
- Extrusion Multiplier: H-0.9, H20, and H40 - 1, H60 - 1.2.
- Bed and chamber temperatures of 120 and 75°C, respectively.
- Speed of printing: 35 mm/s.

Density

- Density 3D printed samples decreased with an increase in filler percentage.
- Void percentage, weight saving potential increases with an increase in filler percentage.
- Core exhibited less density when compared with their respective sandwiches. This is due to the selection of neat HDPE material as skin.

Compression behavior

- Graded foams exhibited better energy absorption when compared with plain foams.
- Modulus of the composite increased with an increase in filler percentage.
- Graded sandwich samples outperformed their respective core in modulus and strength perspective but with little compromise in weight reduction potential.
- Foams exhibited better specific properties compared to H. The specific modulus of H60 is 1.7 times that of pure HDPE. FGF-2 exhibited better specific strength than all 3D printed samples, which is 1.2 times of pure HDPE.
- Comparison among all FGF and FGSFs' showed that FGSF's exhibited higher modulus and strength when compared with their respective cores.
- All graded foams exhibited a sacrificial failure mechanism.

Flexural response

- FGSFs exhibited better strength compared to FGFs. Among all samples, FGF-2 exhibited the highest modulus.
- Modulus of FGF-2 enhanced by 33.83% compared to pure HDPE.
- All at once, 3D printed FGSFs exhibited better strength compared to non-graded foams.

- FGFs exhibited higher specific modulus than their corresponding sandwiches
- FGSFs exhibited higher specific strength than their corresponding cores
- Due to material property gradation, the asymmetric stress distribution is observed along the thickness direction.
- Only type-2 of FGF and FGSFs underwent fracture among all the printed samples.
- No delamination is observed, even at higher deformations.

Vibration response

- Compared to pure H buckling strength of FGF-1, FGF-2 and FGF-3 calculated using DTM and MBC method are increased by 39, 78.4, 47 % and 44.68, 87.23, 53.19%, respectively.
- FGF-2 exhibited a higher buckling strength and natural frequency among plain core and FGFs
- At mode-1 natural frequency decreases with an increasing compressive load, and trend reversal creeps in the post-buckling regime. The damping factor showed a reverse trend with respect to the compressive load.
- Among all FGSFs, FGSF-2 shows better P_{cr} and natural frequency values.
- The natural frequency of FGSFs decreases in the pre-buckling zone and increases in the post-buckling zone.
- FG core sandwiches gave better results for P_{cr} and natural frequency than a plain core sandwich.
- No delamination is observed, even load increased beyond the P_{cr} .

Thermal Buckling

- Thermal stability of the syntactic foam beam increased with an increase in filler percentage.
- H60 exhibited higher critical buckling temperature (T_{cr}) among all 3D printed plain core samples.
- Developing the sample by varying the material property of all thickness directions enhanced the stability of the beam.

- Functionally graded sandwich samples (FGSFs) outperformed all 3D printed samples in terms of stability and higher buckling temperatures.
- All 3D printed samples exhibited higher deformation when the position was selected at the center of the beams.
- All 3D printed samples exhibited lower deflection in one end heating condition (Case-1).
- None of the samples exhibited delamination behavior in any heating conditions, even at higher buckling temperatures.

The current work successfully demonstrated the 3D printing of the functionally graded core and their respective sandwiches using FFF based 3D printing technology. Response of these graded samples under various mechanical and thermal loads was studied. Results showed that the beams' stability, strength and energy absorption capability could be enhanced by opting the functionally graded sandwich beams rather than opting for plain beams.

SCOPE OF FUTURE WORK

The present work successfully demonstrated syntactic foam development and its filament extrusion. Further possible defects in FFF process and appropriate 3D printing parameters for processing the developed foams are presented. 3D printing strategy for developing the functionally graded sandwich foams and the behavior of these graded foams under different loads and loading conditions are explored. This work can be further explored by studying the behavior of graded beams developed by varying the material property symmetrically along the thickness direction with respect to the neutral axis. Trails can be conducted to improve the filler matrix interface bonding by surface-treating the hollow GMB particles.

REFERENCES

A. K. Noor, W. S. Burton and Bert., C. W. (1996). "Computational Models for Sandwich Panels and Shells." *Applied Mechanics Reviews*, Vol. 49, No3, pp. 155-200.

Ahmed, M. O., Masood Syed Hasan and Lal., B. J. (2016). "Optimization of fused deposition modeling process parameters for dimensional accuracy using I-optimality criterion." *Measurement*, 81, 174-196.

Amirpour Maedeh, Bickerton Simon, Calius Emilio, Das Raj and Brian., M. (2019). "Numerical and experimental study on deformation of 3D-printed polymeric functionally graded plates: 3D-Digital Image Correlation approach." *Composite structures*, 211, 481-489.

Anandrao Khalane Sanjay, Gupta RK, Ramachandran P and Venkateswara., R. G. (2012). "Free vibration analysis of functionally graded beams." *Defence Science Journal*, 62(3), 139-146.

Annigeri Ulhas K and B., V. K. G. (2018). "Effect of Reinforcement on Density, Hardness and Wear Behavior of Aluminum Metal Matrix Composites: A Review." *Materials Today: Proceedings*, 5(5, Part 2), 11233-11237.

Anthony Xavier M, Nishanth D, Navin Kumar N and P., J. (2020). "Synthesis and Testing of FGM made of ABS Plastic Material." *Materials Today: Proceedings*, 22, 1838-1844.

Arivazhagan Adhiyamaan, Saleem Ammar, Masood SH, Nikzad Mostafa and KA., J. (2014). "Study of dynamic mechanical properties of fused deposition modelling processed ultem material." *American Journal of Engineering and Applied Sciences*, 7(3), 307-315.

Arzamasov., B. (1989). "Material Science. Moscow: Mir Publishers."

ASTMF2792-10. "Standard Terminology for Additive Manufacturing Technologies, ASTM International, PA, USA."

Aydogdu Metin and Vedat., T. (2007). "Free vibration analysis of functionally graded beams with simply supported edges." *Materials & Design*, 28(5), 1651-1656.

B John and Nair. (2014). "13 - Syntactic foams. ." In H. Dodiuk & S. H. Goodman (Eds.), *Handbook of thermoset plastics (Thied Edition)*. Boston: William Andrew Publishing., (pp. 511-554).

Beesetty Pavan, Patil Balu and Mrityunjay., D. (2020). "Mechanical behavior of additively manufactured nanoclay/HDPE nanocomposites." *Composite structures*, 247, 112442.

Bharath H. S, Bonthu Dileep, Gururaja Suhasini, Prabhakar Pavana and Mrityunjay., D. (2021). "Flexural response of 3D printed sandwich composite." *Composite structures*, 263, 113732.

Bharath HS, Bonthu Dileep, Gururaja Suhasini, Prabhakar Pavana and Mrityunjay., D. (2021). "Flexural response of 3D printed sandwich composite." *Composite structures*, 263, 113732.

Bharath HS, Bonthu Dileep, Prabhakar Pavana and Mrityunjay., D. (2020). "Three-dimensional printed lightweight composite foams." *ACS Omega*, 5(35), 22536.

Bharath HS, Sawardekar Akshay, Waddar Sunil, Jeyaraj P and Mrityunjay., D. (2020). "Mechanical behavior of 3D printed syntactic foam composites." *Composite structures*, 254, 112832.

Bharath HS, Waddar Sunil, Bekinal Siddappal, Jeyaraj P and Mrityunjay., D. (2021). "Effect of axial compression on dynamic response of concurrently printed sandwich." *Composite structures*, 259, 113223.

Bharath Kumar BR, Zeltmann Steven Eric, Doddamani Mrityunjay, Gupta Nikhil, Gurupadu S and RRN., S. (2016). "Effect of cenosphere surface treatment and blending method on the tensile properties of thermoplastic matrix syntactic foams." *Journal of applied polymer science*, 133(35).

Bhavar Valmik, Kattire Prakash, Thakare Sandeep and RKP., S. (2017). *A review on functionally gradient materials (FGMs) and their applications*. Paper presented at the IOP Conference Series: Materials Science and Engineering.

Birman Victor and A., K. G. (2018). "Review of current trends in research and applications of sandwich structures." *Composites Part B: Engineering*, 142, 221-240.

Birman Victor and George., K. (2018). "Review of current trends in research and applications of sandwich structures." *Composites Part B: Engineering*.

Boschetto Alberto and Luana., B. (2016). "Design for manufacturing of surfaces to improve accuracy in Fused Deposition Modeling." *Robotics and Computer-Integrated Manufacturing*, 37, 103-114.

Breunig PETER, Damodaran VINAY, Shahapurkar KIRAN, Waddar SUNIL, Doddamani MRITYUNJAY, Jeyaraj P and P., P. (2020). "Dynamic impact behavior of syntactic foam core sandwich composites." *Journal of Composite Materials*, 54(4), 535-547.

Bunn P and JT., M. (1993). "Manufacture and compression properties of syntactic foams." *Composites*, 24(7), 565-571.

Byberg Kate Iren, Gebisa Aboma Wagari and G., L. H. (2018). "Mechanical properties of ULTEM 9085 material processed by fused deposition modeling." *Polymer Testing*, 72, 335-347.

Caeti Ryan, Gupta Nikhil and Maurizio., P. (2009). "Processing and compressive response of functionally graded composites." *Materials Letters*, 63(22), 1964-1967.

Calahorra A, Gara O and S., K. (1987). "Thin film parylene coating of three-phase syntactic foams." *Journal of Cellular Plastics*, 23(4), 383-398.

Caminero MA, Chacón JM, García-Moreno I and JM., R. (2018). "Interlaminar bonding performance of 3D printed continuous fibre reinforced thermoplastic composites using fused deposition modelling." *Polymer Testing*, 68, 415-423.

Chakraborty A, Gopalakrishnan S and JN., R. (2003). "A new beam finite element for the analysis of functionally graded materials." *International journal of mechanical sciences*, 45(3), 519-539.

Chen H. C, Chen T. Y and H., H. C. (2006). "Effects of Wood Particle Size and Mixing Ratios of HDPE on the Properties of the Composites." *Holz als Roh- und Werkstoff*, 64(3), 172-177.

Chen Han and Fiona., Z. Y. (2016). "Process parameters optimization for improving surface quality and manufacturing accuracy of binder jetting additive manufacturing process." *Rapid Prototyping Journal*, 22(3), 527-538.

Chris., D. (2011). 26 - Functional Fillers for Plastics. In M. Kutz (Ed.), *Applied Plastics Engineering Handbook* (pp. 455-468). Oxford: William Andrew Publishing.

Das Pallab and Pankaj., T. (2019). "Thermal degradation study of waste polyethylene terephthalate (PET) under inert and oxidative environments." *Thermochimica Acta*, 679, 178340.

Datsyuk V, Trotsenko S, Trakakis G, Boden A, Vyzas-Asimakopoulos K, Parthenios J, Galiotis C, Reich S and K., P. (2020). "Thermal properties enhancement of epoxy resins by incorporating polybenzimidazole nanofibers filled with graphene and carbon nanotubes as reinforcing material." *Polymer Testing*, 82, 106317.

David., K. (2017). Three-dimensional printing of plastics *Applied plastics engineering handbook* (pp. 617-634): Elsevier.

Doddamani MR and SM., K. (2011). "Dynamic response of fly ash reinforced functionally graded rubber composite sandwiches-a Taguchi approach." *International Journal of Engineering, Science and Technology*, 3(1).

Doddamani MR and SM., K. (2012). "Response of fly ash-reinforced functionally graded rubber composites subjected to mechanical loading." *Mechanics of Composite Materials*, 48(1), 89-100.

Doddamani Mrityunjay, Shunmugasamy Vasanth Chakravarthy, Gupta Nikhil and HB., V. (2015). "Compressive and flexural properties of functionally graded fly ash cenosphere–epoxy resin syntactic foams." *Polymer Composites*, 36(4), 685-693.

Domingo-Espin Miquel, Puigoriol-Forcada Josep M, Garcia-Granada Andres-Amador, Llumà Jordi, Borros, S. and Guillermo., R. (2015). "Mechanical property characterization and simulation of fused deposition modeling Polycarbonate parts." *Materials & Design*, 83, 670-677.

Domingo-Espin Miquel, Puigoriol-Forcada Josep M, Garcia-Granada Andres-Amador, Llumà Jordi, Borros Salvador and Guillermo., R. (2015). "Mechanical property characterization and simulation of fused deposition modeling Polycarbonate parts." *Materials & Design*, 83, 670-677.

Dontsov Yury V, Panin Sergey V, Buslovich Dmitry G and Filippo., B. (2020). "Taguchi optimization of parameters for feedstock fabrication and FDM

manufacturing of wear-resistant UHMWPE-based composites." *Materials*, 13(12), 2718.

Ebrahimi Farzad and Ali., J. (2016). "A Higher-Order Thermomechanical Vibration Analysis of Temperature-Dependent FGM Beams with Porosities." *Journal of Engineering*, 2016, 9561504.

Elamin Mohammed Eltayeb Salih, Li Bing and T., T. K. (2018). "Impact damage of composite sandwich structures in arctic condition." *Composite structures*, 192, 422-433.

Escócio Viviane Alves, Pacheco Elen Beatriz Acordi Vasques, Silva Ana Lucia Nazareth da, Cavalcante André de Paula and Yuan., V. L. L. (2015). "Rheological behavior of renewable polyethylene (HDPE) composites and sponge gourd (*Luffa cylindrica*) residue." *International Journal of Polymer Science*, 2015.

Espalin David, Arcaute Karina, Rodriguez David, Medina Francisco, Posner Matthew and Ryan., W. (2010). "Fused deposition modeling of patient-specific polymethylmethacrylate implants." *Rapid Prototyping Journal*.

Gangil Brijesh, Kukshal Vikas, Sharma Ankush, Patnaik Amar and Sandeep., K. (2019). *Development of hybrid fiber reinforced functionally graded polymer composites for mechanical and wear analysis*. Paper presented at the AIP conference proceedings.

Gao Fan and Yuanzhi., Z. (2020). "Method for preparing micro-nano-particle-reinforced PDMS-based FGM using 3D printing single nozzle." *Materials Letters*, 280, 128548.

Geng Peng, Zhao Ji, Wu Wenzheng, Ye Wenli, Wang Yulei, Wang Shuobang and Shuo., Z. (2019). "Effects of extrusion speed and printing speed on the 3D printing

stability of extruded PEEK filament." *Journal of Manufacturing Processes*, 37, 266-273.

Gilorkar Amol, Murugan Rajesh and Jeyaraj., P. (2020). "Thermal buckling of sisal and glass hybrid woven composites: Experimental investigation." *Composites Part C: Open Access*, 2, 100012.

Gordeev Evgeniy G, Galushko Alexey S and P., A. V. (2018). "Improvement of quality of 3D printed objects by elimination of microscopic structural defects in fused deposition modeling." *PloS one*, 13(6), e0198370.

Griffiths Chrisian A, Howarth Jack, De Almeida-Rowbotham Gabriela and Andrew., R. (2016). "A design of experiments approach to optimise tensile and notched bending properties of fused deposition modelling parts." *Proceedings of the institution of mechanical engineers, Part B: Journal of Engineering Manufacture*, 230(8), 1502-1512.

Gupta Nikhil, Maharsia Rahul and Dwayne., J. H. (2005). "Enhancement of energy absorption characteristics of hollow glass particle filled composites by rubber addition." *Materials Science and Engineering: A*, 395(1-2), 233-240.

Gupta Nikhil, Pinisetty Dinesh and Chakravarthy., S. V. (2013). *Reinforced polymer matrix syntactic foams: effect of nano and micro-scale reinforcement*: Springer Science & Business Media.

Gupta Nikhil and Ruslan., N. (2006). "Tensile properties of glass microballoon-epoxy resin syntactic foams." *Journal of applied polymer science*, 102(2), 1254-1261.

H S Bharath, Bonthu Dileep, Prabhakar Pavana and Mrityunjay., D. (2020). "Three-Dimensional Printed Lightweight Composite Foams." *ACS Omega*, 5(35), 22536-22550.

Haldar AK, Managuli Vishwanath, Munshi R, Agarwal RS and ZW., G. (2021). "Compressive behaviour of 3D printed sandwich structures based on corrugated core design." *Materials today communications*, 26, 101725.

Hemath Mohit, Mavinkere Rangappa Sanjay, Kushvaha Vinod, Dhakal Hom Nath and Suchart., S. (2020). "A comprehensive review on mechanical, electromagnetic radiation shielding, and thermal conductivity of fibers/inorganic fillers reinforced hybrid polymer composites." *Polymer Composites*, 41(10), 3940-3965.

Hobeika S, Men Y and G., S. (2000). "Temperature and strain rate independence of critical strains in polyethylene and poly (ethylene-co-vinyl acetate)." *Macromolecules*, 33(5), 1827-1833.

HS Bharath, Bonthu Dileep, Prabhakar Pavana and Mrityunjay., D. (2020). "Three-Dimensional Printed Lightweight Composite Foams." *ACS Omega*, 5(35), 22536-22550.

Hsissou Rachid, Seghiri Rajaa, Benzekri Zakaria, Hilali Miloudi, Rafik Mohamed and Ahmed., E. (2021). "Polymer composite materials: A comprehensive review." *Composite structures*, 262, 113640.

Hwang Seyeon, Reyes Edgar I, Moon Kyoung-sik, Rumpf Raymond C and Soo., K. N. (2015). "Thermo-mechanical characterization of metal/polymer composite filaments and printing parameter study for fused deposition modeling in the 3D printing process." *Journal of Electronic Materials*, 44(3), 771-777.

ISO22007-2:2015. (2015). "Plastics — Determination of thermal conductivity and thermal diffusivity — Part 2: Transient plane heat source (hot disc) method."

Ivanov Evgeni, Kotsilkova Rumiana, Xia Hesheng, Chen Yinghong, Donato Ricardo K, Donato Katarzyna, Godoy Anna Paula, Di Maio Rosa, Silvestre Clara, Cimmino Sossio and Verislav., A. (2019). "PLA/Graphene/MWCNT Composites with

Improved Electrical and Thermal Properties Suitable for FDM 3D Printing Applications." *Applied Sciences*, 9(6), 1209.

Jayavardhan M. L and Mrityunjay., D. (2018). "Quasi-static compressive response of compression molded glass microballoon/HDPE syntactic foam." *Composites Part B: Engineering*, 149, 165-177.

Jayavardhan ML, Kumar BR Bharath, Doddamani Mrityunjay, Singh Ashish K, Zeltmann Steven E and Nikhil., G. (2017). "Development of glass microballoon/HDPE syntactic foams by compression molding." *Composites Part B: Engineering*, 130, 119-131.

Jayavardhan ML and Mrityunjay., D. (2018). "Quasi-static compressive response of compression molded glass microballoon/HDPE syntactic foam." *Composites Part B: Engineering*, 149, 165-177.

Jeyachandran Praveen, Bontha Srikanth, Bodhak Subhadip, Balla Vamsi Krishna, Kundu Biswanath and Mrityunjay., D. (2020). "Mechanical behaviour of additively manufactured bioactive glass/high density polyethylene composites." *Journal of the Mechanical Behavior of Biomedical Materials*, 108, 103830.

Jeyachandran Praveen, Bontha Srikanth, Bodhak Subhadip, Krishna., B. V. and Mrityunjay., D. (2021). "Material extrusion additive manufacturing of bioactive glass/high density polyethylene composites." *Composites Science and Technology*, 213, 108966.

Jiang Li-li, Xu Guo-dong, Cheng Su, Lu Xia-mei and Tao., Z. (2014). "Predicting the thermal conductivity and temperature distribution in 3D braided composites." *Composite structures*, 108, 578-583.

Kanakannavar Sateeshkumar and Jeyaraj., P. (2021). "Thermal buckling of braided flax woven polylactic acid composites." *Journal of Reinforced Plastics and Composites*, 40(7-8), 261-272.

Kim Ho Sung and Azhar., K. M. (2001). "Fracture and impact behaviours of hollow micro-sphere/epoxy resin composites." *Composites Part A: Applied Science and Manufacturing*, 32(9), 1311-1317.

Kooistra Gregory W, Queheillalt Douglas T and NG., W. H. (2008). "Shear behavior of aluminum lattice truss sandwich panel structures." *Materials Science and Engineering: A*, 472(1-2), 242-250.

Kumar BR Bharath, Doddamani Mrityunjay, Zeltmann Steven E, Gupta Nikhil, Ramesh MR and Seeram., R. (2016). "Processing of cenosphere/HDPE syntactic foams using an industrial scale polymer injection molding machine." *Materials & Design*, 92, 414-423.

Kumar K Senthil, Siva I, Jeyaraj P, Jappes JT Winowlin, Amico SC and N., R. (2014). "Synergy of fiber length and content on free vibration and damping behavior of natural fiber reinforced polyester composite beams." *Materials & Design (1980-2015)*, 56, 379-386.

Kumar Sumodh, Ramesh MR, Doddamani Mrityunjay, Rangappa Sanjay Mavinkere and Suchart., S. (2022). "Mechanical characterization of 3D printed MWCNTs/HDPE nanocomposites." *Polymer Testing*, 114, 107703.

Labans E, Abramovich H and C., B. (2019). "An experimental vibration-buckling investigation on classical and variable angle tow composite shells under axial compression." *Journal of Sound and vibration*, 449, 315-329.

Laishram Rokesh, Bisheshwar H, Shivakumar ND, Amrutur Bharadwaj and TY., R. "A Study on the Effects of Fiber Orientation on Woven Glass Fiber Composite Structures."

Lee SM and Peter., P. (1992). "Braiding." *Handbook of Composite Reinforcements*, 24-40.

Lingaiah K and BG., S. (1991). "Strength and stiffness of sandwich beams in bending." *Experimental Mechanics*, 31(1), 1-7.

Liu H, Wu Q, Han G, Yao F, Kojima Y and S., S. (2008). "Compatibilizing and toughening bamboo flour-filled HDPE composites: Mechanical properties and morphologies." *Composites Part A: Applied Science and Manufacturing*, 39(12), 1891-1900.

Liu L, Kardomateas George A, Birman Victor, Holmes JW and J., S. G. (2006). "Thermal buckling of a heat-exposed, axially restrained composite column." *Composites Part A: Applied Science and Manufacturing*, 37(7), 972-980.

Liu Zhihui and Junchuan., N. (2018). "Vibrational energy flow model for functionally graded beams." *Composite structures*, 186, 17-28.

M., S. (2007). "Thermal buckling analysis of rectangular composite plates with temperature-dependent properties based on a layerwise theory." *Thin-Walled Structures*, 45(4), 439-452.

Masood SH and WQ., S. (2004). "Development of new metal/polymer materials for rapid tooling using fused deposition modelling." *Materials & Design*, 25(7), 587-594.

Mines RAW, Tsopanos S, Shen Y, Hasan R and ST., M. (2013). "Drop weight impact behaviour of sandwich panels with metallic micro lattice cores." *International Journal of Impact Engineering*, 60, 120-132.

MK., K. (1982). "A three-dimensional rectangular crack subjected to shear loading." *International Journal of Solids and Structures*, 18(12), 1075-1082.

Montgomery S. Macrae, Hilborn Haley, Hamel Craig M, Kuang Xiao, Long Kevin N and Jerry., Q. H. (2021). "The 3D printing and modeling of functionally graded Kelvin foams for controlling crushing performance." *Extreme Mechanics Letters*, 46, 101323.

Mrityunjay., D. (2020). "Dynamic mechanical analysis of 3D printed eco-friendly lightweight composite." *Composites Communications*, 19, 177-181.

Narahara Hiroyuki, Shirahama Yota and Hiroshi., K. (2016). "Improvement and evaluation of the interlaminar bonding strength of FDM parts by atmospheric-pressure plasma." *Procedia Cirp*, 42, 754-759.

Neves AMA, Ferreira AJM, Carrera E, Cinefra M, Jorge RMN and CMM., S. (2012). "Buckling analysis of sandwich plates with functionally graded skins using a new quasi- 3D hyperbolic sine shear deformation theory and collocation with radial basis functions." *ZAMM- Journal of Applied Mathematics and Mechanics/Zeitschrift für Angewandte Mathematik und Mechanik*, 92(9), 749-766.

Nikhil., G. (2007). "A functionally graded syntactic foam material for high energy absorption under compression." *Materials Letters*, 61(4-5), 979-982.

Nikhil., G. and Eyassu., W. (2004). "Microballoon wall thickness effects on properties of syntactic foams." *Journal of Cellular Plastics*, 40(6), 461-480.

Nikzad Mostafa, Masood S Hasan and Igor., S. (2011). "Thermo-mechanical properties of a highly filled polymeric composites for fused deposition modeling." *Materials & Design*, 32(6), 3448-3456.

Omar Mohammed Yaseer, Xiang Chongchen, Gupta Nikhil, Strbik III Oliver M and Kyu., C. (2015). "Syntactic foam core metal matrix sandwich composite: Compressive properties and strain rate effects." *Materials Science and Engineering: A*, 643, 156-168.

Omar Mohd Firdaus, Akil Hazizan Md and Arifin., A. Z. (2012). "Effect of molecular structures on dynamic compression properties of polyethylene." *Materials Science and Engineering: A*, 538, 125-134.

Pan Lun, Shen Guo-Qiang, Zhang Jing-Wen, Wei Xiao-Chu, Wang Li, Zou Ji-Jun and Xiangwen., Z. (2015). "TiO₂-ZnO composite sphere decorated with ZnO clusters for effective charge isolation in photocatalysis." *Industrial & Engineering Chemistry Research*, 54(29), 7226-7232.

Park S, Russell BP, Deshpande VS and NA., F. (2012). "Dynamic compressive response of composite square honeycombs." *Composites Part A: Applied Science and Manufacturing*, 43(3), 527-536.

Patil Balu, Kumar BR Bharath, Bontha Srikanth, Balla Vamsi Krishna, Powar Satvasheel, Kumar V Hemanth, Suresha SN and Mrityunjay., D. (2019). "Eco-friendly lightweight filament synthesis and mechanical characterization of additively manufactured closed cell foams." *Composites Science and Technology*, 183, 107816.

Pilkey Walter D, Pilkey Deborah F and Zhuming., B. (2020). *Peterson's stress concentration factors*: John Wiley & Sons.

Porter Daniel A, Hoang Trung VT and A., B. T. (2017). "Effects of in-situ poling and process parameters on fused filament fabrication printed PVDF sheet mechanical and electrical properties." *Additive Manufacturing*, 13, 81-92.

Qin Qing-hua, Zhang Jian-xun, Wang Zheng-jin, Li Hui-min and GUO., D. (2014). "Indentation of sandwich beams with metal foam core." *Transactions of Nonferrous Metals Society of China*, 24(8), 2440-2446.

R., V. J. (2018). *The behavior of sandwich structures of isotropic and composite materials*: Routledge.

Rajesh M and Jeyaraj., P. (2017). "Experimental investigation on buckling and free vibration behavior of woven natural fiber fabric composite under axial compression." *Composite structures*, 163, 302-311.

Reza., E. M. (2018). Buckling and Post-buckling of Beams. In M. R. Eslami (Ed.), *Buckling and Postbuckling of Beams, Plates, and Shells* (pp. 7-110). Cham: Springer International Publishing.

Rezayat Hassan, Zhou W, Siriruk Akawut, Penumadu D and SS., B. (2015). "Structure–mechanical property relationship in fused deposition modelling." *Materials Science and Technology*, 31(8), 895-903.

Rinaldi Marianna, Ghidini Tommaso, Cecchini Federico, Brandao Ana and Francesca., N. (2018). "Additive layer manufacturing of poly (ether ether ketone) via FDM." *Composites Part B: Engineering*, 145, 162-172.

Sadanand, K., Satish Kumar S, S, S. K., Sinha Umesh Kumar, Shah Brijeshkumar, Satish Kumar K, Steve Mithran AJ and K., M. P. (2021). *Vibration Reduction in Indigenous Wankel Rotary Combustion Engine with Structured Layer Damping*. Paper presented at the Proceedings of the 6th National Symposium on Rotor Dynamics.

ShekharB. (2012). " Roadmap to 13 Million Tons." *Plastindia in-house journal*, 37, 6-11.

Singer J. A, Arbocz J. A, Weller T. A and R., C. J. A. (2003). ""Buckling Experiments: Experimental Methods in Buckling of Thin-Walled Structures. Shells, Built-up Structures, Composites and Additional Topics, Volume 2." *Applied Mechanics Reviews*, 56(1), B5."

Singh Manoj Kumar and Sunny., Z. (2021). "Wettability, absorption and degradation behavior of microwave-assisted compression molded kenaf/HDPE composite tank under various environments." *Polymer Degradation and Stability*, 185, 109500.

Singh Rupinder, Bedi Piyush, Fraternali Fernando and IPS., A. (2016). "Effect of single particle size, double particle size and triple particle size Al₂O₃ in Nylon-6 matrix on mechanical properties of feed stock filament for FDM." *Composites Part B: Engineering*, 106, 20-27.

Spoerk Martin, Arbeiter Florian, Cajner Hrvoje, Sapkota Janak and Clemens., H. (2017). "Parametric optimization of intra- and inter- layer strengths in parts produced by extrusion- based additive manufacturing of poly (lactic acid)." *Journal of applied polymer science*, 134(41), 45401.

Tang XC, Jian WR, Huang JY, Zhao F, Li C, Xiao XH, Yao XH and SN., L. (2018). "Spall damage of a Ta particle-reinforced metallic glass matrix composite under high strain rate loading." *Materials Science and Engineering: A*, 711, 284-292.

Tao Yubo, Wang Honglei, Li Zelong, Li Peng and Q., S. S. (2017). "Development and Application of Wood Flour-Filled Polylactic Acid Composite Filament for 3D Printing." *Materials*, 10(4), 339.

Tarhini AA and AR., T.-B. (2019). "Graphene-based polymer composite films with enhanced mechanical properties and ultra-high in-plane thermal conductivity." *Composites Science and Technology*, 184, 107797.

Tay Yi Wei Daniel, Lim Jian Hui, Li Mingyang and Jen., T. M. (2022). "Creating functionally graded concrete materials with varying 3D printing parameters." *Virtual and Physical Prototyping*, 17(3), 662-681.

Tian Chun Guang, Yuan Ye, Bi Zheng Jun, Cai Li Xia and Juan., H. X. (2013). *Analysis software of power quality and power regulation for wind farm based on dewetron*. Paper presented at the Applied Mechanics and Materials.

Toudehdehghan Abdolreza, Lim JW, Foo Kim Eng, Ma'Arof MIN and J., M. (2017). *A brief review of functionally graded materials*. Paper presented at the MATEC Web Conferences.

Triantafillou Thanasis Christos and J., G. L. (1987). "Minimum weight design of foam core sandwich panels for a given strength." *Materials Science and Engineering*, 95, 55-62.

Tsouknidas A, Pantazopoulos M, Katsoulis I, Fasnakis D, Maropoulos S and N., M. (2016). "Impact absorption capacity of 3D-printed components fabricated by fused deposition modelling." *Materials & Design*, 102, 41-44.

Tucker Katherine, Tucker David, Eastham James, Gibson Elizabeth, Varma Sumir and Tugrul., D. (2014). "Network based technology roadmapping for future markets: case of 3D printing." *Technology and Investment*, 2014.

Tuttle M, Singhatanadgid P and G., H. (1999). "Buckling of composite panels subjected to biaxial loading." *Experimental Mechanics*, 39(3), 191-201.

Vaggar Gurushanth B and SC., K. (2020). "Thermal property characterization for enhancement of thermal conductivity of hybrid polymer composites." *Materials Today: Proceedings*, 20, 208-212.

Vijayavenkataraman Sanjairaj, Fuh Jerry YH and Feng., L. W. (2017). "3D printing and 3D bioprinting in pediatrics." *Bioengineering*, 4(3), 63.

Vu Minh Canh, Jeong Tae- Hyeong, Kim Jun- Beom, Choi Won Kook, Kim Dae Hoon and Sung- Ryong., K. (2021). "3D printing of copper particles and poly (methyl methacrylate) beads containing poly (lactic acid) composites for enhancing thermomechanical properties." *Journal of applied polymer science*, 138(5), 49776.

Waddar Sunil, Jeyaraj P, Doddamani Mrityunjay and Nikhil., G. (2018). "Buckling and free vibration behavior of cenosphere/epoxy syntactic foams under axial compressive loading."

Waddar Sunil, Jeyaraj P and Mrityunjay., D. (2018). "Influence of axial compressive loads on buckling and free vibration response of surface-modified fly ash cenosphere/epoxy syntactic foams." *Journal of Composite Materials*, 52(19), 2621-2630.

Waddar Sunil, Pitchaimani Jeyaraj, Doddamani Mrityunjay and Ever., B. (2019). "Buckling and vibration behaviour of syntactic foam core sandwich beam with natural fiber composite facings under axial compressive loads." *Composites Part B: Engineering*, 175, 107133.

Waddar Sunil, Pitchaimani Jeyaraj and Mrityunjay., D. (2018). "Snap-through buckling of fly ash cenosphere/epoxy syntactic foams under thermal environment." *Thin-Walled Structures*, 131, 417-427.

Waddar Sunil, Pitchaimani Jeyaraj and Mrityunjay., D. (2020). "Effect of thermal loading on syntactic foam sandwich composite." *Polymer Composites*, 41(5), 1774-1784.

Wadley Haydn NG, Fleck Norman A and G., E. A. (2003). "Fabrication and structural performance of periodic cellular metal sandwich structures." *Composites Science and Technology*, 63(16), 2331-2343.

Wang Rong, Shang Jianzhong, Li Xin, Luo Zirong and Wei., W. (2018). "Vibration and damping characteristics of 3D printed Kagome lattice with viscoelastic material filling." *Scientific reports*, 8(1), 1-13.

Wouterson Erwin M, Boey Freddy YC, Hu Xiao and Shing-Chung., W. (2005). "Specific properties and fracture toughness of syntactic foam: Effect of foam microstructures." *Composites Science and Technology*, 65(11-12), 1840-1850.

Wu Helong, Kitipornchai Sritawat and Jie., Y. (2015). "Free vibration and buckling analysis of sandwich beams with functionally graded carbon nanotube-reinforced composite face sheets." *International Journal of Structural Stability and Dynamics*, 15(07), 1540011.

Wu Peng, Wang Jun and Xiangyu., W. (2016). "A critical review of the use of 3-D printing in the construction industry." *Automation in Construction*, 68, 21-31.

X-F., L. (2008). "A unified approach for analyzing static and dynamic behaviors of functionally graded Timoshenko and Euler–Bernoulli beams." *Journal of Sound and vibration*, 318(4-5), 1210-1229.

Yuan Chongxin, Bergsma Otto, Koussios Sotiris, Zu Lei and Adriaan., B. (2012). "Optimization of sandwich composites fuselages under flight loads." *Applied Composite Materials*, 19(1), 47-64.

Zhang Jianxun, Qin Qinghua, Weilong, A., Li Huimin and TJ., W. (2014). "The failure behavior of geometrically asymmetric metal foam core sandwich beams under three-point bending." *Journal of Applied Mechanics*, 81(7).

Zhang Jianxun, Qin Qinghua, Xiang Chunping and TJ., W. (2016). "Dynamic response of slender multilayer sandwich beams with metal foam cores subjected to low-velocity impact." *Composite structures*, 153, 614-623.

Zhong Zheng and Tao., Y. (2007). "Analytical solution of a cantilever functionally graded beam." *Composites Science and Technology*, 67(3), 481-488.

LIST OF PUBLICATIONS

INTERNATIONAL JOURNALS

1. Dileep Bonthu, Prakash Rohit, Bharath H.S, Jeyaraj.P. and Mrityunjay Doddamani. (2021). "Dynamic behavior of concurrently printed functionally graded closed cell foams." *Composite Structures*, 275, 114449. (Impact factor 6.60, SCI).
2. Dileep Bonthu and Mrityunjay Doddamani. (2021). "Compressive response of 3D printed graded foams." *Composites Part C*: 6, 100181 (Scopus).
3. Dileep Bonthu, H.S. Bharath, S. Gururaja, P. Prabhakar, and Mrityunjay Doddamani, (2020) "3D printing of syntactic foam cored sandwich composite". *Composites Part C*: 3: p. 100068. (Scopus).
4. Dileep Bonthu, Bharath H S, Siddappa I. Bekinal, P Jeyaraj, and Mrityunjay Doddamani, "Dynamic response of 3D printed functionally graded sandwich foams". *Rapid Prototyping* (Under Review). (Impact factor 4.2, SCI).
5. Dileep Bonthu, Vinyas Mahesh and Mrityunjay Doddamani, "3D printed functionally graded foams response under transverse load". *Materials Today Communication* (Under Review). (Impact factor 3.66, SCI).
6. Dileep Bonthu, Jeyaraj.P. and Mrityunjay Doddamani, "Thermal buckling behaviour of 3D printed foams: Plain, Graded and Sandwich variants". *Next Materials* (Under Review).

BIO-DATA

1. Name : Bonthu Dileep
2. Father's Name : B V Satyanarayana
3. Date of Birth : 15th August 1995
4. Nationality : Indian
5. Marital Status : Unmarried
6. Address : Department of Mechanical Engineering
National Institute of Technology Karnataka
Surathkal, PO Srinivasnagar 575 025
Karnataka, India.
7. Mobile Number : +91 9490750215
8. E-mail id. : *dileepbonthusai@gmail.com*
9. Educational Qualification :

Qualification	University/Board	Year of Passing
Ph.D. (Mechanical Engineering)	National Institute of Technology Karnataka	Pursuing
M.Tech. (Mechanical Engineering)	National Institute of Technology Karnataka	2020
B.Tech. (Mechanical Engineering)	Jawaharlal Nehru Technological University, Kakinada	2016